

Universiteit
Leiden
The Netherlands

Deciphering the complex paramagnetic NMR spectra of small laccase

Dasgupta, R.

Citation

Dasgupta, R. (2021, June 15). *Deciphering the complex paramagnetic NMR spectra of small laccase*. Retrieved from https://hdl.handle.net/1887/3188356

Version:	Publisher's Version
License:	Licence agreement concerning inclusion of doctoral thesis in the Institutional Repository of the University of Leiden
Downloaded from:	https://hdl.handle.net/1887/3188356

Note: To cite this publication please use the final published version (if applicable).

Cover Page



Universiteit Leiden



The handle https://hdl.handle.net/1887/3188356 holds various files of this Leiden University dissertation.

Author: Dasgputa, R.
Title: Deciphering the complex paramagnetic NMR spectra of small laccase
Issue Date: 2021-06-15

Rubin Dasgupta
Deciphering the complex paramagnetic NMR spectra of small laccase
Ph.D. thesis, Leiden University, Leiden, The Netherlands

ISBN/EAN: 978-94-92597-75-5
Printed by PRINTSUPPORT4U || www.printsupport4u.nl
Cover design by Rubin Dasgupta

This research was financed by Leiden University and Netherlands' Magnetic Resonance Research School (NWO-BOO 022.005.029). The use of the uNMR-NL ultrahigh-field nuclear magnetic resonance facility was sponsored by the national roadmap for the large-scale NMR facility in the Netherlands (NWO grant number: 184-032-207).

Deciphering the complex paramagnetic NMR spectra of small laccase

Proefschrift

ter verkrijging van
de graad van doctor aan de Universiteit Leiden,
op gezag van rector magnificus prof.dr.ir. H. Bijl,
volgens besluit van het college voor promoties
te verdedigen op dinsdag 15 juni 2021
klokke 13:45 uur

door

Rubin Dasgupta

geboren te Kolkata, India
in 1992

Promotiecommissie

Promotors:	Prof. dr. M. Ubbink Prof. dr. H. J. M. de Groot
Promotiecommissie:	Prof. dr. H. S. Overkleeft (voorzitter) Prof. dr. M. Koper (secretaris)
Overige commissieleden:	Prof. dr. G. W. Canters (Leiden University, The Netherlands) Prof. dr. C. Luchinat (University of Florence, Italy) Dr. K. Petzold (Karolinska Institute, Sweden) Dr. P. Schanda (Institut de Biologie Structural, Grenoble, France)

For everything good in the world

सर्वे भवन्तु सुखिनः

Table of Contents

List of abbreviations..... 1

1. Introduction..... 2

1.1 General Introduction..... 3

1.2 The multicopper oxidase: Laccase..... 7

1.3 Paramagnetic nuclear magnetic resonance..... 13

1.4 Aim and Scope..... 21

1.5 References..... 22

2. Chemical exchange at the tri-nuclear copper center of small laccase from *Streptomyces coelicolor*..... 28

2.1 Introduction..... 29

2.2 Results and Discussion..... 30

2.3 Conclusion..... 37

2.4 Supporting Information..... 38

2.5 References..... 50

3. Towards resolving the complex paramagnetic NMR spectrum of small laccase: Assignment of resonances to residue specific nuclei.... 54

3.1 Introduction..... 55

3.2 Results and Discussion..... 57

3.3 Conclusion..... 65

3.4 Supporting Information..... 66

3.5 References..... 73

4. The resting oxidized state of small laccase analyzed with paramagnetic NMR spectroscopy..... 76

4.1 Introduction..... 77

4.2 Results and Discussion..... 79
4.3 Conclusion..... 88
4.4 Supporting Information..... 89
4.5 References..... 97
5. Electronic structure of the tri-nuclear copper center in the resting oxidized state for small laccase..... 100
5.1 Introduction..... 101
5.2 Results and Discussion..... 101
5.3 Conclusion..... 102
5.4 Supporting Information..... 105
5.5 References..... 106
6. Dipolar dephasing for structure determination in a strongly paramagnetic environment..... 108
6.1 Introduction..... 109
6.2 Results and Discussion..... 111
6.3 Conclusion..... 116
6.4 Supporting Information..... 117
6.5 References..... 124
7. General Discussion and Prospects..... 128
Summary..... 138
Samenvatting..... 140
Curriculum vitae..... 142
List of Publications..... 143

List of abbreviations

BMRB	Biological magnetic resonance bank
BS	Broken symmetry
DFT	Density functional theory
EBC	Enzymatic biofuel cell
EPR	Electron paramagnetic resonance
EXSY	Exchange spectroscopy
FCS	Fermi contact shift
FR	Fully reduced
FWHM	Full width at half of the maximum
HMQC	Heteronuclear multiple quantum coherence
HS	High spin
INEPT	Insensitive nuclei enhancement by polarization transfer
MAS	Magic angle spinning
MCD	Magnetic circular dichroism
MHz	Megahertz
NI	Native intermediate
NMR	Nuclear magnetic resonance
NOESY	Nuclear Overhauser effect spectroscopy
PCS	Pseudo-contact shift
PI	Peroxide intermediate
REDOR	Rotational echo double resonance
RF	Radiofrequency
RO	Resting oxidized
SHAP	Short high-power adiabatic pulse
SLAC	Small laccase
ssNMR	Solid-state NMR
T1	Type-1 copper site
T2	Type-2 copper site
T3	Type-3 copper site
TEDOR	Transferred-echo double resonance
TNC	Tri-nuclear copper center
WEFT	Water eliminated Fourier transform
wt	Wild type

Chapter 1

Introduction

The Road goes ever on and on,
Down from the door where it began.
Now far ahead the Road has gone,
And I must follow, if I can,

Pursuing it with eager feet,
Until it joins some larger way
Where many paths and errands meet.
And whither then? I cannot say.

– John Ronald Reuel Tolkien

1.1 General introduction

Enzymatic biofuel cells (EBCs) promise a sustainable and energy efficient future. It is a type of fuel cell that uses enzymes to catalyse redox reactions rather than precious non-renewable metals (platinum, palladium, ruthenium, etc.). A typical EBC oxidizes substrates at the anodic half, while reducing oxygen to water at the cathodic half. The anode can be functionalized with different enzymes depending on the application, for example using glucose dehydrogenase to oxidize glucose and act as biosensors for insulin delivery.(1) The cathode is usually functionalized with a multicopper oxidase (MCO), such as laccase, for the oxygen reduction reaction, due to their high efficiency and low required overpotential.(2, 3) The efficiency of a fuel cell is reflected by the power density of the system that represents the electron production rate.(2, 4) The traditional fuel cells can afford power densities in the order of a few kilowatts while the EBCs can generate power densities in the range of microwatts to milliwatts.(4) This limits the application of the EBCs to small devices, for example pacemakers (5), biosensors (6), wristwatches (7, 8), light-emitting diodes (9–11), music play back devices (12) and generating electricity from sunlight (13). Although there has been major advances in the application of EBCs, their commercial application remains elusive.(2, 14) It was estimated that an enzyme with a 100 nm^2 cross section and an activity of 500 electrons per second can generate a current density of 80 $\mu A \cdot cm^{-2}$.(15) For practical applications a biofuel cell will require a current density of 10 $mA \cdot cm^{-2}$ that will necessitate loading of thousands of monolayers of enzyme on the electrodes.(4, 15) This poses a considerable engineering problem in addition to the challenges of improving the electron transfer from the enzyme to the electrodes and the life time of the enzyme.

One of the major contributors in defining the efficiency of a fuel cell is the oxygen reduction reaction at the cathodic half.(16) This reaction is a 4-electron reduction of molecular oxygen to water that has a reduction potential of 1.23 V. The major challenges in the oxygen reduction reaction that hinder the wide spread application of the fuel cells are the slow kinetics and the high required overpotential, which limits the thermodynamic efficiency to ~40-60%.(17) The origin of the overpotential is the strong dioxygen bond with a bond energy of 498 kJ/mol.(18) In a traditional fuel cell platinum or its alloy is used as the cathode catalyst, providing an overpotential of ~ 300 mV. However, its high cost renders industrial applications impractical.(17) In contrast, the EBCs uses laccase to perform the oxygen reduction reaction, with a very low overpotential of ~ 20 mV, and a turn-over rate of 2.1 O_2 per laccase per second.(19) Although functionalizing laccase on the electrode seems promising, its limitations outweighs its effectiveness. The commonly encountered limitations are the enzyme instability, inhibition by high salt concentrations (≥ 100

mM), low pH range of activity, large scale production of the enzyme and difficulty in achieving high packing densities due to the large size of laccase.(2, 17, 20) One way to overcome such limitations is to design an artificial "bio-inspired" catalyst.(20, 21) Extensive research is being carried out to synthesize efficient artificial catalysts for the oxygen reduction reaction based on the active site of laccase and in recent years several candidates were reported (Table 1.1, for a detailed list of copper based catalysts for oxygen reduction reaction (ORR), refer to Thorseth *et al.*(17)).(20) It is evident that most of the artificial catalysts are either mononuclear or binuclear copper complexes and the most efficient catalyst was reported to be Cu-Hdatrz (Table 1.1). However, the power density generated falls below the platinum based catalyst.(17) Ligand modification such as using pyridine, pyrrole, imidazole and triazole in association with bridging moieties between the copper centres were shown to improve the overall performance of the catalyst but the enzyme laccase remains the most efficient in terms of overpotential and turnover frequency per active site.(17, 20, 22) Improvement of the turnover frequency per site was reported for polymeric copper based catalysts, such as Cu(3, 3'-diaminobenzidine) (21), and self-assembled monolayer based systems (20), due to their high stability but minimal improvement was observed in terms of overpotential.(21)

There are multiple factors affecting the efficiency of such "bio-inspired" catalysts. First, the geometry of the primary coordination sphere that can stabilize different binding modes of dioxygen results in different reaction mechanisms, i.e. $4e^-/4H^+$ conversion of dioxygen to water or $2e^-/2H^+$ conversion of dioxygen to hydrogen peroxide.(22–24) The coordination of the active site in laccase (described in section 1.2) was shown to be in an "entatic state" with a distorted tetrahedral geometry, thereby attaining a conformation that compromises between the favoured geometries for Cu(I) and Cu(II) ions.(25–28) Such a state reduces the reorganization energy of the reaction and enables the protein to transfer electrons efficiently.(26, 27) In laccase, the type 1 copper site (described in section 1.2) was studied extensively, showing that the reorganization energy was ~ 0.5 eV upon reduction of the copper ion by extracting an electron from substrate. In contrast, the reorganization energy of the substrate was in the range of 1.2 to 2.0 eV. This suggests that the geometry of the T1 site in the protein does not change much and is in an entatic state, while the geometry of the substrate does change.(25, 29) Creating an entatic state of the metal coordination in artificial catalysts poses a challenge for synthesis. A few successful attempts have been reported for a heme based oxygen activation system, and recently for copper based photoactive complexes, aiming for efficient electron transfer.(27, 30)

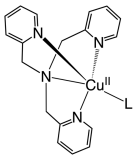
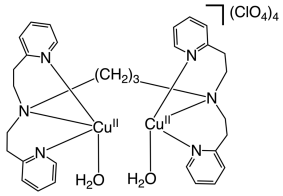
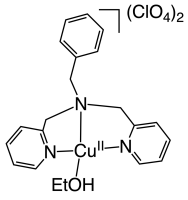
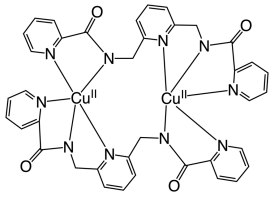
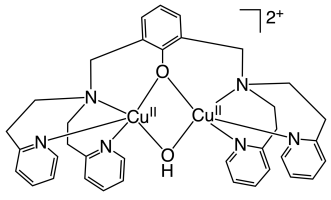
Second, it was shown that in the laccase second coordination sphere residues like aspartic acid or glutamic acid are important in regulating the proton chemical potential and stabilizing the intermediate states.(31–33) This idea was implemented in an iron-porphyrin based system with a carboxyphenyl group in the second

coordination sphere where the carboxylic groups are oriented toward the redox centre, acting as a proton relay.(34) However, the overpotential was observed to be ~ 400 mV, 20 times higher than that of laccase.

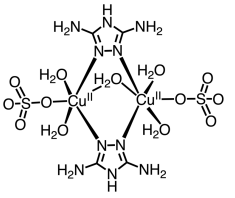
This leads to the final factor that can affect the efficiency of these catalysts, the motions at the redox active site. Oxygen reduction catalysed by laccase is a complicated reaction comprising a series of steps, including several electron transfer steps, oxygen binding, bond breaking, proton transfers through the enzyme, protonation and water release (the detailed reaction mechanism in laccase is shown in section 1.2).(25, 29). The function of the enzyme is two-fold, lowering the activation barriers of each of the consecutive steps and ensuring that all steps occur in the desired order, avoiding side products. Enzymes speed up reactions by stabilizing transition states with favourable interactions in the active site. Lowering proton transfer barriers may require an enzyme conformation different from the one required to lower the barrier for oxygen-oxygen bond breaking. Thus, it seems almost inevitable that laccase uses different conformations during the catalytic cycle, implying motions must occur. Such a sophisticated approach of catalysis requires a system with many atoms and it may well be fundamentally impossible to mimic that with low molecular weight compounds (Table 1.1) in detail. Examples of such motions is ubiquitous in enzymes. For example in alcohol dehydrogenase the binding of substrate NAD^+ causes conformational changes in the active site that reduces the barrier for proton transfer.(35) Similarly, the substrate free adenylate kinase was found to undergo preferred motions in μs-ms time scale to attain substates along the reaction coordinate.(36)

Extensive studies on the dynamics at the TNC of laccase have not been reported but observations from crystal structures (PDB entries 2xu9 (37) and 3zx1 (38)) show that active site histidine imidazole rings can attain two conformations without breaking the coordination with the coppers. Investigating the dynamics of the TNC at the atomic level is non-trivial. A crystal structure shows a time-averaged conformation. Nuclear magnetic resonance (NMR) spectroscopy in solution suffers from the large size of the enzyme, and line broadening caused by the paramagnetic copper ions. The research described in this thesis is based on paramagnetic NMR spectroscopy to probe motions or conformational heterogeneity at the TNC of a laccase. A two-domain small laccase from *Streptomyces coelicolor* (SLAC) (39) is employed, because of its thermostability, ease of large-scale production, resistance to high salt concentrations (~ 1 M) and pH ≥ 7.0.(39–41) Although using SLAC directly on an electrode looks promising, the low turnover frequency and limited stability hinders upscaling for application.(42) This study can help in designing a functional framework for efficient "bio-inspired" oxygen reduction catalysts that can be applied for longer term usage. Maybe, a small low molecular weight protein or peptide mimic of the active site of laccase can be advantageous.

Table 1.1. *Examples of oxygen reduction catalysts based on the active site of laccase.*

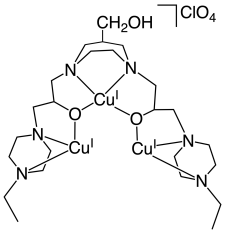
Catalyst	Structure	Ref.
$[Cu(tmpa)(L)]^{2+}$ tmpa = tris(2-pyridylmethyl) amine L = $(trifluoromethanesulfonate)_2$		(43)
$[Cu^{II}_2(N3)(H_2O)_2](ClO_4)_4$ N3 = (– $(CH_2)_3$-linked (bis[2-(2-pyridyl) ethyl] amine)$_2$)		(23)
$[Cu^{II}(BzPY1)(EtOH)](ClO_4)_2$ BzPY1 = N-Benzyl-N, N-bis(2-pyridinylmethyl) amine		(23)
Copper complex with polypyridine-polyamide ligand		(44)
$[Cu^{II}_2(LO)\text{-}(OH)]^{2+}$ [LO = bi-nucleating ligand with copper-bridging phenolate moiety]		(24)

$[Cu_2(Hdatrz)_2(\mu\text{-}OH_2)\ (H_2O)_4(SO_4)_2]$
Hdatrz = 3,5-diamino-1,2,4-triazole



(45)

Cu_3(7-N-Etppz (CH_2OH))
Etppz = 3,3′-(6-(hydroxymethyl) -1,4-diazepane-1,4-diyl) bis(1-(4-ethylpiperazin-1-yl) propan-2-ol)



(16)

1.2 The multicopper oxidase: Laccase

Laccase is a multi-copper oxidase (MCO) comprising two active sites, a type 1 (T1) site for oxidizing substrates and a tri-nuclear copper centre (TNC) for the oxygen reduction reaction (Figure 1.1). The type 1 site is also known as the blue copper site and consists of a copper ion coordinated to a cysteine sulphur, and two histidine ligands. An additional axial methionine can coordinate the copper in case of the low (100 to 400 mV) redox potential laccases (Figure 1.2a and c). The TNC is comprised of a type 3 (T3) and a type 2 (T2) copper site. A T3 site is characterized by a binuclear copper centre in which each copper ion is coordinated by three histidine ligands and the copper ions are bridged by a hydroxide. A T2 site is characterized by a copper centre coordinated by two histidine ligands and a water derived ligand (water or hydroxide ion). The T1 and T2 sites are electron paramagnetic resonance (EPR) active, while the T3 site is EPR silent due to the strong antiferromagnetic coupling between the electron spins on the cupric ions.(25)

Laccases can be divided into two classes, three-domain monomeric laccases and two-domain trimeric small laccases (Figure 1.1). Three-domain laccases are further divided into low redox potential (100 to 400 mV) and high redox potential (> 400 mV) laccases, based on the redox potential of the T1 site. Three-domain laccases are widely distributed among different domains of life, while the two-domain small laccases are found mostly in prokaryotes.(46) The T1 copper ions of the two-domain small laccases and the low redox potential three-domain laccases are coordinated by an additional axial methionine, which was shown to be the reason for their low redox potential.(47–49) For the three-domain laccases lacking this axial methionine ligand

and in combination with a hydrophobic environment of the T1 site, the high redox potential is high (Figure 1.2).(40, 48, 50) Both the two-domain small laccases and three-domain laccases were subjected to many directed evolution and site-directed mutation studies to raise the redox potential of the T1 site and to increase the high pH stability.(48, 50–52) In recent years, the T1 site of the two-domain small laccase was successfully modified to have a redox potential comparable to the high redox potential fungal laccases.(48, 50, 53) Table 1.2 shows the redox potential of different small laccases (for the detailed list of the redox potentials of different laccases refer to Mate *et al.* (49)). It is observed that replacing the methionine residues with more hydrophobic residues near the T1 site increases the redox potential drastically.(50) In addition to improving the T1 site redox potential, studies were performed to improve the activity of small laccase by site directed mutagenesis.(40, 54, 55) Table 1.3 summarizes the mutants that showed higher activity than the wild type. Two such mutants have been reported, H165A, located near the T3 site, and Y230A, near the T1 site (Figure 1.2). The increase in activity was attributed to enhanced accessibility of the copper ions and oxygen in the T3 site and improvement in substrate binding, respectively.(40, 55)

Table 1.2. *Redox potentials of the T1 sites of native small laccases and variants.*

Laccase	Source	Redox potential (T1 site)	Reference
SvSL	*S. viridochromogenes*	350 ± 7 mV	(56)
Ssl1	*S. sviceus*	375 ± 8 mV	(50)
SLAC	*S. coelicolor*	430 mV	(42)
Ssl1 M295L/M293G/M195A/V287N	*S. sviceus*	560 ± 6 mV	(53)

Table 1.3*. Small laccase mutants that showed higher substrate oxidation activity than wild type.*

Laccase	Source	Mutant	Activity (mutant/wild type) (nM min^{-1} μg^{-1})	Reference
SLAC	*S. coelicolor*	Y230A	1.20/0.98	(40)
SgfSL	*S. griseoflavus*	H165A	1.45/0.82	(55)

Also, the TNCs differ between the two-domain and three-domain laccases. In the former three TNCs are located at the interfaces of the three subunits, while in the

three-domain laccases, a single TNC is found at the interface of two domains (Figure 1.1). In the small laccases the coppers in the TNC are coordinated by His Nε2 atoms, whereas in three-domain laccases one of the T3 coppers has a Nδ1 as a coordinating atom. Residues in the second coordination sphere of the TNC are also different between small laccases and three-domain laccases. In the former, the second coordination sphere is mostly occupied by polar residues, except for I169 and A266. It has been hypothesized that due to this polarity near the TNC of the two-domain SLAC it has greater tolerance for high pH and high salt concentration.(54, 55) In three-domain laccases most second shell residues are hydrophobic, except for the glutamates and aspartates near the T3 and the T2 sites (Figure 1.2). In three-domain laccases the aspartic/glutamic acid in the second coordination sphere of the T3 site was shown to be a proton donor, while the aspartate near the T2 site is an acceptor, keeping the total charge of the TNC constant during the proton transfer process of the oxygen reduction reaction (Figure 1.2e and f).(31, 32, 57) Similar arrangements of polar residues at the entrances of the water channel can be observed in the crystal structures of small laccases. Here, protons can be donated by the glutamine or serine near the T3 site and accepted by the aspartate near the T2 site. However, there is no experimental or theoretical proof for such a process in small laccase. A common feature of the two-domain and three-domain laccases is the presence of a water channel that passes through the TNC (Figure 1.2d, e and f), providing the entry path for protons required for the formation of water. It was reported that the tyrosine near the T2 site is a unique feature of small laccase, as it allows free radical formation during the oxygen reduction reaction.(58–60) Recently, a study using side directed mutagenesis showed that His164 (Figure 1.2d; numbering from PDB 3cg8) acts a gatekeeper residue for dioxygen entry.(55) Mutating it to alanine increased the activity of the small laccase (Table 1.2).(55) Similar gatekeeper residue was not yet reported for the three-domain laccase. The structural, biochemical and sequence analysis of the two-domain small laccase and three-domain laccase suggests that they originated from a common ancestor and later differentiated to serve the same function in different conditions.(46)

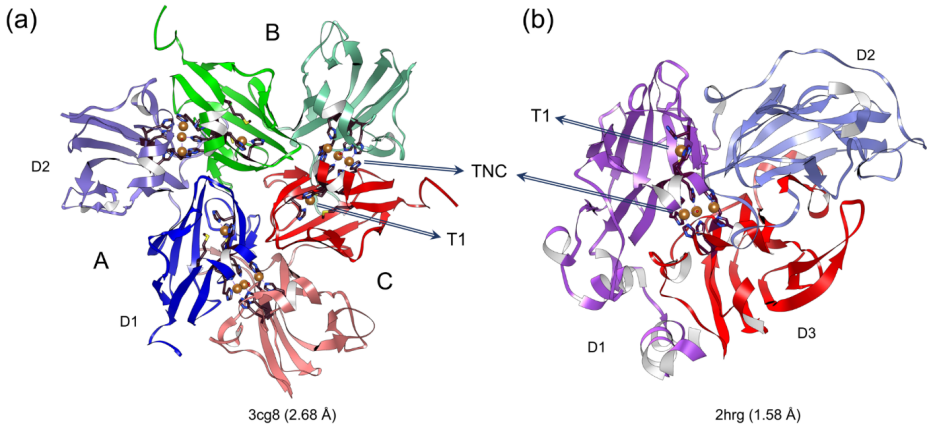


Figure 1.1. *(a) Crystal structure of two-domain laccase from S. coelicolor (PDB 3cg8).(61) The two-domain laccase forms a homotrimer in solution and the subunits are shown in red, blue and green, with the two domains in different shades. In subunit A the domains are marked D1 and D2. (b) Crystal structure of three-domain laccase from Trametes trogii (PDB 2hrg) showing the three domains D1 in magenta, D2 in light blue and D3 in red.(62) The TNCs are located at the interfaces of subunits (a) or domains (b), while the T1 site is buried in a domain.*

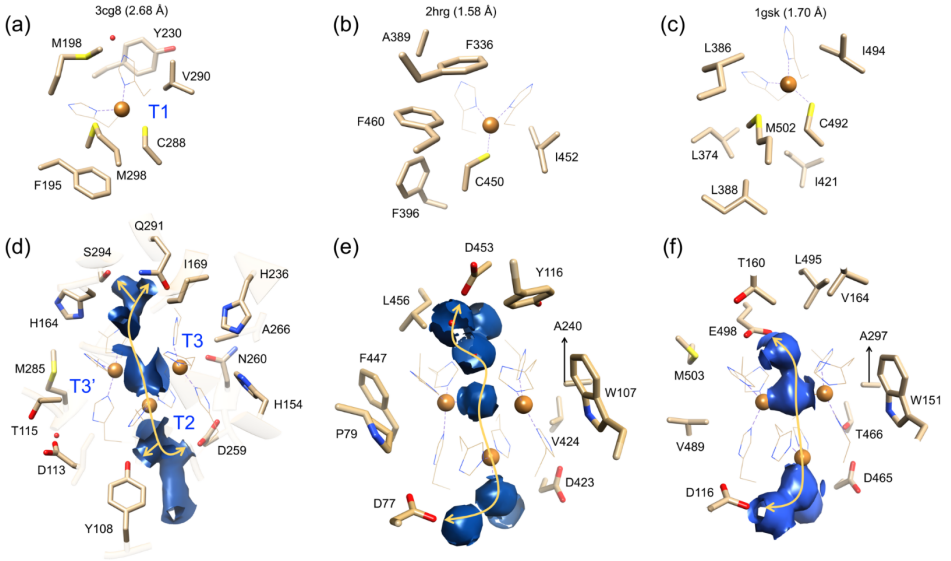


Figure 1.2*. (a-c) T1 sites of small laccase from S. coelicolor (a),(61) the high redox potential three-domain laccase from T. trogii (b),(62) and the low redox potential three-domain laccase from an endospore coat of Bacillus subtilis (c).(63) (d-f) The water channels shown as the electron density surface of the water molecules in the TNC in the crystal structures of the laccases in panels (a-c). The double-sided arrows show possible proton transfer paths. Coordinating histidine ligands are shown as wire and second coordination sphere residues are shown as sticks. Red spheres are the bound water molecules. The copper sites are marked in panels a and d.*

The oxygen reduction reaction is summarized in Figure 1.3 and 1.4b.(29, 32, 58, 60, 64, 65) The resting oxidized (RO) state is reduced to the fully reduced (FR) state by four electrons that are provided by oxidation of substrates at the T1 site (Figure 1.2, 1.3 and 1.4b). The FR state binds oxygen and reduces it to a peroxide intermediate (PI) state by two-electron transfer (Figure 1.4b). The subsequent conversion of the PI to the native intermediate (NI) state requires two more electrons. The third cuprous copper ion supplies one electron and the second can be obtained from either the tyrosine near the T2 site in small laccase or the T1 site (Figure 1.3 and 1.4b). In the small laccase from *S. coelicolor* (SLAC), the Y108 residue (Figure 1.2a) was reported to provide this electron to the T2 copper, when the T3 site copper ions are reduced (Figure 1.3).(58, 60) A similar observation was made for human ceruloplasmin, in which the tyrosine radical is formed during the conversion of RO state to the FR state.(58, 66) Without substrate the NI state is slowly converted to the RO state, while it is rapidly converted to the FR state with excess of substrates present.(65) The basic structure for the catalytic motif of the TNC in the RO state is shown in Figure 1.4a.(32, 65, 67) This structure is shared among all the laccases and is used for density functional theory (DFT) calculations. It is particularly suited for modelling entatic states since the overall charge and spin state of the catalytic motif can be defined without resolving spin and charge down to the level of individual magnetic ions and histidine side chains. This provides room for structural flexibility such as histidine ring motions at the active site. The modelling of the catalytic motif can also be aided by defining the redox couples during the oxygen reduction reaction (Figure 1.4b) where the charge and spin multiplicities are stated. For small laccases and human ceruloplasmin the tyrosine near the T2 site is also involved in the catalytic mechanism as mentioned above (Figure 1.3). The present model of the oxygen reduction reaction at the TNC however, does not consider the motions that can help in attaining a conformation that can reduce the energy barrier for electron and proton transfer.

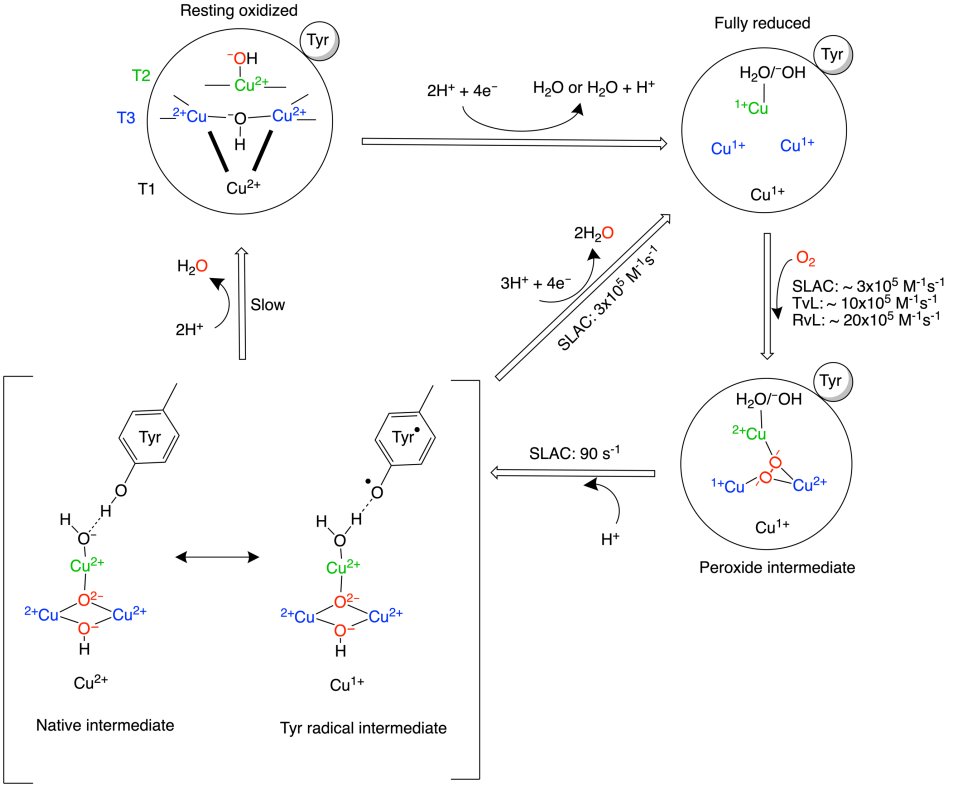
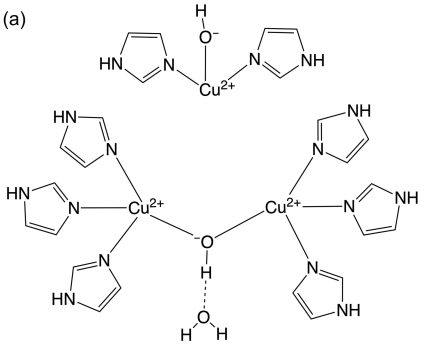


***Figure 1.3**: Reaction mechanism of the oxygen reduction reaction in SLAC. The coordination of the coppers in the TNC is shown in the resting oxidized state with the T3 coppers (blue) coordinated by three His Nε2 atoms each and the hydroxyl group, whereas the T2 copper (green) is coordinated by two His Nε2 atoms and a hydroxide/water.(32, 57, 65) The oxygen binding rates are shown for laccases from several organisms, SLAC from S. coelicolor, TvL from Trametes versicolor laccase and RvL for Rhus vernicifera laccase.(65) A tyrosine radical intermediate for SLAC is shown.(58) The formation of the tyrosine radical intermediate was reported only for small laccase and human ceruloplasmin.(66) The O atom is coloured red to show that it is from the oxygen molecule undergoing reduction. Only the stable intermediate states are denoted for the transition states in-between readers are referred to Solomon et al. (64, 65)*

(a)



(b) *Redox couples* $^{(Spin\ multiplicity\ 2S+1)}[Cu^{Charge\ of\ each\ atom}_{Number\ of\ atoms}]$

$$T_1^{ox} - {}^2[Cu_3^{II}(^-OH)(-OH)](\boldsymbol{RO}) \xrightarrow{k + 4e^- + 4k^{IET}} T_1^{red} - {}^1[Cu_3^{I}](\boldsymbol{FR}) + H_2O$$

$$T_1^{red} - {}^1[Cu_3^{I}](\boldsymbol{FR}) \xrightarrow{2k^{IET} + O_2} T_1^{red} - {}^1[Cu_1^{I}\,Cu_2^{II}(^-OO^-)(^-OH)](\boldsymbol{PI})$$

$$T_1^{red} - {}^1[Cu_1^{I}\,Cu_2^{II}(^-OO^-)(^-OH)](\boldsymbol{PI}) \xrightarrow{k^{IET}} T_1^{ox} - {}^2[Cu_2^{I}\,Cu_1^{II}(^-OO^-)(^-OH)](\boldsymbol{PI} + \boldsymbol{e}^-)$$

$$T_1^{ox} - {}^2[Cu_2^{I}\,Cu_1^{II}(^-OO^-)(^-OH)](\boldsymbol{PI} + \boldsymbol{e}^-) \xrightarrow{2k^{IET} + H^+} T_1^{ox} - {}^2[Cu_3^{II}(^-OH)\,(O^{2-})(^-OH)](\boldsymbol{NI})$$

$$T_1^{ox} - {}^2[Cu_3^{II}(^-OH)\,(O^{2-})(^-OH)](\boldsymbol{NI}) \xrightarrow{3H^+ + 4e^-} T_1^{red} - {}^1[Cu_3^{I}](\boldsymbol{FR}) + 2H_2O$$

$$T_1^{ox} - {}^2[Cu_3^{II}(^-OH)\,(O^{2-})(^-OH)](\boldsymbol{NI}) \xrightarrow{H^+} T_1^{ox} - {}^2[Cu_3^{II}(^-OH)(-OH)](\boldsymbol{RO}) + H_2O$$

Figure 1.4*: (a) The starting minimal model of the TNC in the RO state used by Solomon et al., to describe the reaction mechanism using DFT calculations.(32, 65, 67) The coordinating histidine ligands are replaced with the imidazolyl groups. The charges of the copper ions and the hydroxide ions are shown. (b) The redox couples describing the reaction mechanism of the oxygen reduction by the TNC. The spin multiplicities associated with each catalytic state, the charges of the copper ions and oxygen atoms are shown. In the reaction k represents the rate of substrate oxidation at the T1 copper site and k^{IET} represents the intramolecular electron transfer rate.*

1.3 Paramagnetic nuclear magnetic resonance spectroscopy

Studying the TNC with NMR spectroscopy is complicated by several factors. SLAC is a protein of more than 100 kDa in the native trimeric form, making the application of standard techniques for backbone assignment of resonances very challenging. However, the signals of nuclear spins around the coppers in oxidized form have properties that vary greatly from those of nuclear spins far away. The latter will have relatively short transverse and very long longitudinal relaxation times due to the

slow tumbling of the protein in solution, resulting in broad lines and long repetition times. For the nuclei interacting with the strong electron spins, which are on the cupric ions and delocalized over the ligands, the signals experience large chemical shift changes and strongly reduced relaxation times for both transverse and longitudinal relaxation. These features make it possible to selectively detect the signals of nuclear spins near the paramagnetic centres by rapid repetition of NMR scans, combined with long measurement times for sufficient signal-to-noise data and analysis of the spectral region outside the normal envelope of signals for non-paramagnetically shifted peaks. Paramagnetically tailored experiments are necessary to compensate for the short transverse relaxation times, which lead to rapid loss of coherence during the pulse sequence.(68) The observed chemical shift (δ_{obs}) is given by (68)

$$\delta_{\mathrm{obs}} = \delta_{\mathrm{dia}} + \delta_{\mathrm{FCS}} + \delta_{\mathrm{PCS}} \tag{1.1}$$

where δ_{dia} is the diamagnetic chemical shift, δ_{FCS} the Fermi contact shift (FCS) and δ_{PCS} the pseudo-contact shift (PCS).

Fermi contact shift

The FCS is due to the additional magnetic field generated at the nucleus due to the time-averaged electron spin density that is delocalized from the nearby paramagnetic metal. It is a through bond interaction and is generally observed for nuclei that are ≤ 5 bonds away from the metal centre.(68) For a single metal centre, the δ_{FCS} is given by

$$\delta_{\mathrm{FCS}} = \frac{A}{\hbar}\frac{g_{\mathrm{e}}\mu_{\mathrm{B}}S(S+1)}{3\gamma k_{\mathrm{B}}T} \tag{1.2}$$

where A is the isotropic hyperfine coupling constant, g_{e} is the free-spin electron g factor with the value of 2.0023, μ_{B} is the electron Bohr magneton, $\hbar$ is the reduced Planck constant, γ is the gyromagnetic ratio of the nucleus, k_{B} is the Boltzmann constant, T is the temperature in Kelvin and $S = 1/2$, which is in this case the electron spin of the Cu(II) ion. A is directly proportional to the spin density ρ on the nucleus and is given by (68)

$$A = \frac{2}{3}\hbar\gamma_I\mu_{\mathrm{B}}g_{\mathrm{e}}\mu_0\rho \tag{1.3}$$

The sign of the FCS is determined by the polarization of the electron spin. If the spin is parallel to the external magnetic field, the sign is positive and if it is anti-parallel to the external magnetic field, the sign is negative.

In the case of coupled multiple metal centers, as is the case for the TNC of laccase, the FCS is given by (68)

$$\delta_{\mathrm{FCS}} = A\frac{\mu_{\mathrm{B}}g_{\mathrm{e}}}{\hbar\gamma_I 3k_{\mathrm{B}}T}\frac{\sum_{C_i S_{\mathrm{T}}} C_i S_{\mathrm{T}}(S_{\mathrm{T}}+1)(2S_{\mathrm{T}}+1)\mathrm{e}^{-E_{(S_{\mathrm{T}})}/k_{\mathrm{B}}T}}{\sum_{S_{\mathrm{T}}}(2S_{\mathrm{T}}+1)\mathrm{e}^{-E_{(S_{\mathrm{T}})}/k_{\mathrm{B}}T}} \tag{1.4}$$

where S_T is the total electronic spin calculated by Kambe's approach.(69–71) C_i is the ratio of the spin expectation value for the metal ion in Fermi contact with the respective nucleus and the total spin expectation value of all the coupled metal ions.(39, 68) $E_{(S_T)}$ are the eigen values for all the states of S_T.

For a two-spin antiferromagnetically coupled system such as the T3 coppers in the RO state of the TNC equation 1.4 is expressed as (68)

$$\delta_{FCS} = \frac{A}{\hbar}\frac{g_e\mu_B}{\gamma k_B T}\left[\frac{e^{\left(\frac{2J}{k_B T}\right)}}{1+3e^{\left(\frac{2J}{k_B T}\right)}}\right] \tag{1.5}$$

where $2J$ is the energy different between the singlet ($S_T = 0$) ground state and the excited triplet state ($S_T = 1$).

For a three-spin coupled system like the NI state of the TNC, the derivation is more complicated. Following Kambe's approach (69–71), the total spin S_T of a three spin1/2 system can take values of 1/2, 1/2 and 3/2. The two coupled metal centers with spin 1/2 each, form a subunit that can have a spin 1 or 0 ($S_i + S_j$ ... $S_i - S_j$). These states can interact with the third copper ion with spin 1/2. For the two-spin state 0 coupled to the third spin 1/2 a ground state $\left|\frac{1}{2},0\right\rangle$ can be identified, and for the two-spin state 1 coupled to the third spin ½ a first excited doublet state $\left|\frac{1}{2},1\right\rangle$ and a second excited quartet state $\left|\frac{3}{2},1\right\rangle$ are possible due to the higher spin multiplicity for this arrangement.(64, 72).

The expression for C_i depends on the relative strengths of the electronic J couplings between the metal centers in the TNC and is summarized in Table 1.4.(73) The energy levels can be calculated from the Heisenberg Hamiltonian for n interacting spins, (71)

$$\hat{H} = -2\sum_{j>i=1}^{n} J_{ij} S_i \cdot S_j \tag{1.6}$$

where J_{ij} is the exchange coupling between S_i and S_j spins and n=3. There will be in total 8 microstates (M_{xyz}, where xyz are the spin state of each spin) for a three coupled system. Operating the Hamiltonian in equation 1.6 on each microstate $\langle M_{xyz}|\hat{H}|M_{xyz}\rangle$, we get and 8x8 matrix (M1) for the interaction. Solving for the eigenvalues, we get the expression for $E_{(S_T)}$ for each of the energy states (ground state, the first excited doublet state and the second excited doublet state). The expression for $E_{(S_T)}$ in different symmetric conditions of the J coupling (J_{13}, J_{12}, J_{23}) between the copper pairs is summarized in (Table 1.5).(64, 71, 74)

Table 1.4*. Expression for C_i in equation 1.4 for a three spin 1/2 coupled system as in the native intermediate state of the TNC (Figure 1.3). (a) $J_{13} = J_{12} = J_{23} = J$ or $J_{13} = J_{12} = J \neq J_{23}$ and (b) $J_{13} \neq J_{12} \neq J_{23}$*

States	(a)			(b)		
	C_1	C_2	C_3	C_1	C_2	C_3
$\left\|\frac{3}{2},1\right\rangle$	1/3	1/3	1/3	1/3	1/3	1/3
$\left\|\frac{1}{2},1\right\rangle$	2/3	2/3	−1/3	$\frac{2\alpha\sqrt{(1-\alpha^2)}}{\sqrt{3}} + \frac{2-2\alpha^2}{3}$	$-\frac{2\alpha\sqrt{(1-\alpha^2)}}{\sqrt{3}} + \frac{2-2\alpha^2}{3}$	$-\frac{1}{3} + \frac{4\alpha^2}{3}$
$\left\|\frac{1}{2},0\right\rangle$	0	0	1	$-\frac{2\alpha\sqrt{(1-\alpha^2)}}{\sqrt{3}} + \frac{2\alpha^2}{3}$	$\frac{2\alpha\sqrt{(1-\alpha^2)}}{\sqrt{3}} + \frac{2\alpha^2}{3}$	$1 - \frac{4\alpha^2}{3}$

where, $\alpha^2 = \frac{1}{2}(1 - \frac{1}{\sqrt{1+x^2}})$ and $x = \sqrt{3}\frac{J_{12}-J_{13}}{2J_{23}-J_{12}-J_{13}}$, assuming that J_{23} is the strongest coupling.(73)

Table 1.5*: Eigenvalues for the states of S_T with (a) $J_{13} = J_{12} = J_{23} = J$, (b) $J_{13} = J_{12} = J \neq J_{23}$ (c) $J_{13} \neq J_{12} \neq J_{23}$.*

Total spin S_T	Eigenvalues $E_{(S_T)}$		
	(a)	(b)	(c)
3/2 $\|\frac{3}{2},1\rangle$	$-3\frac{J}{2}$	$-\frac{1}{2}(2J + J_{23})$	$-\frac{(J_{12}+J_{23}+J_{13})}{2}$
1/2 $\|\frac{1}{2},1\rangle$	$3\frac{J}{2}$	$2J - J_{23}/2$	$\frac{(J_{12}+J_{23}+J_{13})}{2} + X$
1/2 $\|\frac{1}{2},0\rangle$	$3\frac{J}{2}$	$\frac{3(J_{23})}{2}$	$\frac{(J_{12}+J_{23}+J_{13})}{2} - X$

$$X = \sqrt{{J_{12}}^2 + {J_{13}}^2 + {J_{23}}^2 - J_{12}J_{13} - J_{12}J_{23} - J_{13}J_{23}}$$

Matrix M1 calculated by operating Hamiltonian in equation 1.6 on each microstate (M_{xyz}) of a TNC with 3 coupled Cu^{2+} ions. ($\uparrow = 1/2$ *and* $\downarrow = -1/2$)

Microstates	$\uparrow\uparrow\uparrow$	$\uparrow\uparrow\downarrow$	$\uparrow\downarrow\uparrow$	$\downarrow\uparrow\uparrow$	$\uparrow\downarrow\downarrow$	$\downarrow\uparrow\downarrow$	$\downarrow\downarrow\uparrow$	$\downarrow\downarrow\downarrow$
$\uparrow\uparrow\uparrow$	$-\frac{1}{2}(J_{12}+J_{13}+J_{23})$	0	0	0	0	0	0	0
$\uparrow\uparrow\downarrow$	0	$\frac{1}{2}(-J_{12}+J_{13}+J_{23})$	$-J_{23}$	$-J_{13}$	0	0	0	0
$\uparrow\downarrow\uparrow$	0	$-J_{23}$	$\frac{1}{2}(J_{12}-J_{13}+J_{23})$	$-J_{12}$	0	0	0	0
$\downarrow\uparrow\uparrow$	0	$-J_{13}$	$-J_{12}$	$\frac{1}{2}(J_{12}+J_{13}-J_{23})$	0	0	0	0
$\uparrow\downarrow\downarrow$	0	0	0	0	$\frac{1}{2}(J_{12}+J_{13}-J_{23})$	$-J_{12}$	$-J_{13}$	0
$\downarrow\uparrow\downarrow$	0	0	0	0	$-J_{12}$	$\frac{1}{2}(J_{12}-J_{13}+J_{23})$	$-J_{23}$	0
$\downarrow\downarrow\uparrow$	0	0	0	0	$-J_{13}$	$-J_{23}$	$\frac{1}{2}(-J_{12}+J_{13}+J_{23})$	0
$\downarrow\downarrow\downarrow$	0	0	0	0	0	0	0	$-\frac{1}{2}(J_{12}+J_{13}+J_{23})$

The paramagnetic effect is temperature dependent, for two reasons. With increasing temperature, the populations of the low and high energy levels of an electron spin will become more similar, reducing the time-averaged effect on the nuclear spin, thereby decreasing the FCS (Curie behaviour). For coupled systems, increasing the temperature and thus k_BT, increases the population of the excited S = 1 energy level, so enhancing the paramagnetic effect on the nuclear spin and thus, increasing the shift with temperature (anti-Curie behaviour).(68) Therefore, Curie behaviour is usually observed for signals of nuclear spins near a single copper site, while anti-Curie behaviour is observed for signals of spins near a coupled metal centre with a coupling strength of > 200 cm^{-1}.(68)

Pseudo-contact shift

The PCS is the contribution from the dipolar interaction of the time-averaged unpaired electron spin with the surrounding nuclear spins. It is due to the anisotropy of the magnetic susceptibility tensor (χ) of the metal ion that is observed *e.g.* when the metal ion has spin S ≥ 1/2 with a significant zero field splitting.(75) The metal ion contribution to the PSC (in ppm) is given by (76, 77)

$$\delta_{PCS} = \frac{1}{4\pi}\frac{10^6}{2r^3}\{(1-3\cos^2\theta)(\chi_{zz}-\tilde{\chi}) + \sin^2\theta\cos 2\varphi(\chi_{yy}-\chi_{xx})\} \qquad (1.7)$$

where χ_{xx}, χ_{yy} and χ_{zz} are the principal axis components of the susceptibility tensor with isotropic $\tilde{\chi} = \frac{1}{3}(\chi_{yy}+\chi_{xx}+\chi_{zz})$, θ is the angle between the unit vector along the metal-ligand nuclei and the direction of the χ_{zz} of the susceptibility tensor, r is the distance from the metal ion nucleus to the ligand nucleus and φ is the angle between the projection of unit vector along the line joining the metal and ligand nuclei in the xy plane and the x axis. If the electronic excited state is not thermally accessible at temperatures used for EPR and NMR studies, *i.e.* the ground state is far below any excited state, then the χ-tensor is proportional to the g-tensor, which can be measured by EPR spectroscopy, according to (75, 76)

$$\chi_{ii} = \frac{\mu_0\mu_B^2\, S(S+1)}{3k_BT} g_{ii}^2, \qquad (1.8)$$

where μ_B is the Bohr magneton (9.2740 x 10^{-24} J T^{-1}), S is the electronic spin with S = 1/2 for a single Cu^{2+}, k_B is the Boltzmann constant (1.3807 x 10^{-23} J K^{-1}), μ_0 is the permeability of the vacuum (4π x 10^{-7} kg m s^{-2} A^{-2}) and T is the temperature in Kelvin. Substituting equation 1.8 in equation 1.7, the PCS is given by (76)

$$\delta_{PCS} = 10^6\frac{\mu_0\mu_B^2\, S(S+1)}{4\pi 9k_BTr^3}\left\{\left(g_{zz}^2 - \frac{1}{2}\left(g_{xx}^2+g_{yy}^2\right)\right)(1-3\cos^2\theta) + \left(\frac{3}{2}\left(g_{yy}^2-g_{xx}^2\right)\sin^2\theta\cos 2\varphi\right)\right\}. \qquad (1.9)$$

For SLAC-T1D, it was reported that there is a low lying excited state which is ~125 cm^{-1} (39) above the ground state and can be accessible at temperatures > 175 K. Since

the NMR experiments were done at temperatures between 278 – 303 K, this excited state has to be taken into account to estimate the contribution of the PCS. For such a system the χ-tensor from equation 1.8 is defined as:(71)

$$\chi_{ii} = \frac{\mu_0 \mu_B^2}{3k_B T} g_{ii}^2 \frac{\sum_{S_T} S_T(S_T+1)(2S_T+1)e^{-E_{(S_T)}/k_B T}}{\sum_{S_T}(2S_T+1)e^{-E_{(S_T)}/k_B T}}, \tag{1.10}$$

where $E_{(S_T)}$ is given by expressions in Table 1.5 for different symmetric conditions of a three-coupled spin system (Figure S2.10b) and S_T is same as defined before. Using equation 1.10, equation 1.9 can be rewritten as:

$$\begin{aligned}&\delta_{PCS}\\ &= 10^6 \frac{\mu_0 \mu_B^2}{4\pi 9 k_B T r^3}\left\{\left(g_{zz}^2 - \frac{1}{2}\left(g_{xx}^2 + g_{yy}^2\right)\right)(1-3\cos^2\theta)\right.\\ &\left.+\left(\frac{3}{2}\left(g_{yy}^2 - g_{xx}^2\right)\sin^2\theta\cos 2\varphi\right)\right\}\frac{\sum_{S_T} S_T(S_T+1)(2S_T+1)e^{-E_{(S_T)}/k_B T}}{\sum_{S_T}(2S_T+1)e^{-E_{(S_T)}/k_B T}}\end{aligned} \tag{1.11}$$

Using equation 1.11 one can estimate the PCS contribution to the observed chemical shift (equation 1.1). It can be used to refine the structure of the metalloproteins by providing distance restraints.(68)

Paramagnetic NMR of laccase

The Cu^{2+} ions at the TNC exhibit a strong magnetic coupling that alleviates the problem of the line broadening observed in isolated type 1 copper proteins.(68) The two antiferromagnetically coupled coppers (Figure 1.3) at the T3 site of the RO state behave as a diamagnetic system at low temperatures (< 100 K), however, at elevated temperatures (> 100 K), low lying excited states are populated that are paramagnetic (S = 1), resulting in paramagnetically shifted NMR resonances from the surrounding nuclei.(68, 78) The strong coupling between the coppers at the T3 site increases the electronic relaxation rate of the electron spins, reducing the paramagnetic broadening of nuclear resonances. The T2 site is not (strongly) coupled to the T3 coppers in the RO state, so the relaxation time of the electron spin is much longer, resulting in broadening beyond detection of resonances for nearby nuclear spins. In the NI state however, nuclei near to all the three coppers in the TNC are observed because the T3 and T2 sites are coupled via an oxygen atom (Figure 1.3), forming a frustrated spin system with a spin multiplicity of 2, which results in rapid electronic relaxation and relatively narrow lines for nuclear resonances. In this thesis a small laccase from *S. coelicolor* (SLAC) was used. To study the TNC, a mutant was employed in which the cysteine C288 coordinating the T1 copper ion (Figure 1.2a) was mutated to serine, depleting the T1 site of copper (SLAC-T1D). It was found that for this variant the NI state is dominant (Chapters 2 and 3), while for the wild type SLAC the RO state is most populated (Chapter 4).(73)

Paramagnetic ions decrease the spin lattice relaxation time (T_1) of the nearby nuclei to a few milliseconds compared to the more distant nuclear spins, which have T_1 times of hundreds of milliseconds. The water eliminated Fourier transform (WEFT) pulse sequence (Figure 1.5a) capitalizes on these differences of the T1 times to observe signals from nuclei close to the paramagnetic metal centre.(68, 79) Coupled with rapid pulsing with an inter-scan delay of a few ms, the WEFT pulse sequence can specifically detect the signals from nuclei experiencing the paramagnetic relaxation enhancement.(68) The temperature dependence of the ^{1}H chemical shift from the NI state of SLAC-T1D was shown to consist of resonances having three different behaviours, Curie, anti-Curie and no-Curie.(73) This strongly suggests the presence of more than one coupling between the copper ions because for a single coupling a single temperature dependency is expected for all the resonances.(80, 81) Since in the NI state all the three copper ions at the TNC are coupled, three different couplings can be present (Figure 1.3). The coupling strengths J were reported to be -150 cm^{-1}, -120 cm^{-1} and -80 cm^{-1}, (73) corresponding to the $E_{(S_T)}$ values (expression from Table 1.5 for the general case where $J_{13} \neq J_{12} \neq J_{23}$) of -235 cm^{-1}, -114 cm^{-1} and 175 cm^{-1} for the ground state, first excited doublet state and the second excited quartet state respectively. This results in a low-lying excited state at 121 cm^{-1}, which is in close agreement with the variable temperature MCD measurement that placed this state at 150 cm^{-1}.(73, 82) These observations suggest a triad configuration of the NI state with three copper ions coupled to each other with different strength.(73, 82) In contrast, for the wild type SLAC the temperature dependence of the ^{1}H chemical shift shows a single Cu-Cu coupling consistent with the RO state.(73)

The above observations confirm the magnetic character of the NI and the RO states. To characterize underlying motions at the TNC multidimensional NMR experiments are needed. The 2D exchange spectroscopy (EXSY)(83) (Figure 1.5b) was reported to reveal chemical exchange process in the paramagnetic systems.(68, 84, 85) Nuclear Overhauser enhancements (NOE) can also be present in the EXSY spectrum because exchange and cross relaxation can both occur during the mixing time, in which magnetization is longitudinal. Chemical exchange can be distinguished from NOE signals by the temperature dependence of the volume integral of cross peaks. The volume of the NOE cross peak will not change much with increasing temperature, while it does increase for the exchange cross peak because the exchange rate is temperature dependent.(68) In this work, the EXSY/NOESY (Figure 1.5b) pulse sequence was used to identify chemical exchange processes and NOE cross peaks between protons at the TNC of SLAC (Chapters 2 and 3). 2D ^{15}N–^{1}H heteronuclear experiments can also be performed to determine the type of heteroatom a paramagnetically shifted ^{1}H resonance is attached to.(68, 86) The evolution period in such experiments is optimized, based on the transverse relaxation time (T_2) of the paramagnetically shifted proton resonances.(68) In this study the paramagnetically

tailored 2D ^{15}N–^{1}H heteronuclear multiple quantum coherence (HMQC) (Figure 1.5c) was used to correlate ^{15}N and ^{1}H nuclei via ^{1}J coupling (Chapters 2 and 3).(87)

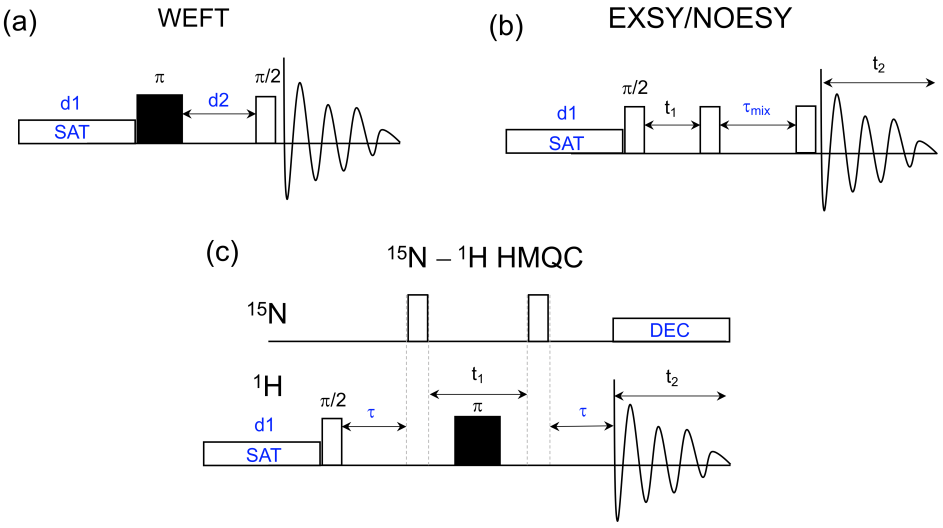


Figure 1.5. *NMR pulse sequences to study the TNC of small laccase from S. coelicolor. (a) 1D water eliminated Fourier transfer (WEFT), where d2 is the WEFT delay,(79) (b) 2D EXSY/NOESY where τ_{mix} is the mixing time (83) and (c) 2D ^{15}N-^{1}H HMQC, where τ is the magnetization transfer delay and DEC is the decoupling.(87) A continuous wave water saturation (SAT) is used during the interscan delay (d1). The incremental delay or the evolution time t_1 and the acquisition time t_2 are shown in panels b and c. Open and filled rectangles represents $\pi/2$ and π pulses, respectively.*

1.4 Aim and Scope

Motional information about the TNC of SLAC is absent, yet it is expected that switching between conformations of the enzyme will be important in catalysing the successive steps of the four-electron reduction of molecular oxygen. The aim of the thesis is to lay the groundwork for detailed studies of the catalysis by laccase and the role of motions using NMR spectroscopy. Signals of nuclear spins very close to the site of oxygen reduction can be used as spies to report on structure and dynamics, provided the signals can be assigned to specific nuclei. A large part of the work presented in this thesis is focussed at that goal. In **Chapter 2** the presence of chemical exchange in the copper ligands in the TNC of the SLAC-T1D is reported. **Chapter 3** shows the first sequence specific assignment of the resonances to the T2 site histidine ligands by comparing SLAC-T1D and a double mutant SLAC-T1D/Y108F. In addition, the NMR

spectral regions of NI and RO states in SLAC-T1D are characterized in detail. In **Chapter 4** the NMR spectrum of SLAC-wt, its comparison with SLAC-T1D and assignment of T3 site histidine ligands using a double mutant SLAC-T1D/Q291E are reported. The role of the second shell residue Gln291 in stabilizing the RO state is demonstrated. **Chapter 5** discusses the results of quantum mechanical calculations on the RO state of the TNC. These calculations can be a step towards resonance assignment. Solid-state NMR (ssNMR) was shown to provide picometer resolution of the copper site in superoxide dismutase.(88) In addition, measuring the dipolar coupling strength of the nuclei near the copper center can provide us with motional information. Optimization and parameterization of suitable pulse sequences for application of ssNMR to laccase is important. This is shown in **Chapter 6** on a model copper compound. **Chapter 7** presents the general discussion and outlook.

1.5 References

1. Jeon, W.-Y., J.-H. Lee, K. Dashnyam, Y.-B. Choi, T.-H. Kim, H.-H. Lee, H.-W. Kim, and H.-H. Kim. 2019. Performance of a glucose-reactive enzyme-based biofuel cell system for biomedical applications. *Scientific Reports*. 9:1–9.
2. Mano, N., and A. de Poulpiquet. 2017. O_2 Reduction in Enzymatic Biofuel Cells. *Chem. Rev.*
3. Wang, J., K. Wang, F.-B. Wang, and X.-H. Xia. 2014. Bioinspired copper catalyst effective for both reduction and evolution of oxygen. *Nat Commun*. 5:5285.
4. Bullen, R.A., T.C. Arnot, J.B. Lakeman, and F.C. Walsh. 2006. Biofuel cells and their development. *Biosensors and Bioelectronics*. 21:2015–2045.
5. Southcott, M., K. MacVittie, J. Halámek, L. Halámková, W.D. Jemison, R. Lobel, and E. Katz. 2013. A pacemaker powered by an implantable biofuel cell operating under conditions mimicking the human blood circulatory system – battery not included. *Phys. Chem. Chem. Phys.* 15:6278.
6. Slaughter, G., and T. Kulkarni. 2019. Detection of Human Plasma Glucose Using a Self-Powered Glucose Biosensor. *Energies*. 12:825.
7. Vincent, K.A., J.A. Cracknell, J.R. Clark, M. Ludwig, O. Lenz, B. Friedrich, and F.A. Armstrong. 2006. Electricity from low-level H2 in still air – an ultimate test for an oxygen tolerant hydrogenase. *Chem. Commun.* 5033.
8. Vincent, K.A., J.A. Cracknell, A. Parkin, and F.A. Armstrong. 2005. Hydrogen cycling by enzymes: electrocatalysis and implications for future energy technology. *Dalton Trans.* 3397.
9. Cinquin, P., C. Gondran, F. Giroud, S. Mazabrard, A. Pellissier, F. Boucher, J.-P. Alcaraz, K. Gorgy, F. Lenouvel, S. Mathé, P. Porcu, and S. Cosnier. 2010. A Glucose BioFuel Cell Implanted in Rats. *PLoS ONE*. 5:e10476.
10. Zebda, A., S. Cosnier, J.-P. Alcaraz, M. Holzinger, A. Le Goff, C. Gondran, F. Boucher, F. Giroud, K. Gorgy, H. Lamraoui, and P. Cinquin. 2013. Single Glucose Biofuel Cells Implanted in Rats Power Electronic Devices. *Scientific Reports*. 3:1–5.
11. Chen, X., L. Yin, J. Lv, A.J. Gross, M. Le, N.G. Gutierrez, Y. Li, I. Jeerapan, F. Giroud, A. Berezovska, R.K. O'Reilly, S. Xu, S. Cosnier, and J. Wang. 2019. Stretchable and Flexible Buckypaper-Based Lactate Biofuel Cell for Wearable Electronics. *Advanced Functional Materials*. 29:1905785.
12. Sony Develops. *Sony Global - Sony Global Headquarters*.
13. Flexer, V., and N. Mano. 2010. From Dynamic Measurements of Photosynthesis in a Living Plant to Sunlight Transformation into Electricity. *Anal. Chem.* 82:1444–1449.
14. Xiao, X., H. Xia, R. Wu, L. Bai, L. Yan, E. Magner, S. Cosnier, E. Lojou, Z. Zhu, and A. Liu. 2019. Tackling the Challenges of Enzymatic (Bio)Fuel Cells. *Chem. Rev.* 119:9509–9558.
15. Calabrese Barton, S., J. Gallaway, and P. Atanassov. 2004. Enzymatic Biofuel Cells for Implantable and Microscale Devices. *Chem. Rev.* 104:4867–4886.

16. Thiyagarajan, N., D. Janmanchi, Y.-F. Tsai, W.H. Wanna, R. Ramu, S.I. Chan, J.-M. Zen, and S.S.-F. Yu. 2018. A Carbon Electrode Functionalized by a Tricopper Cluster Complex: Overcoming Overpotential and Production of Hydrogen Peroxide in the Oxygen Reduction Reaction. *Angewandte Chemie International Edition*. 57:3612–3616.
17. Thorseth, M.A., C.E. Tornow, E.C.M. Tse, and A.A. Gewirth. 2013. Cu complexes that catalyze the oxygen reduction reaction. *Coordination Chemistry Reviews*. 257:130–139.
18. Gewirth, A.A., and M.S. Thorum. 2010. Electroreduction of Dioxygen for Fuel-Cell Applications: Materials and Challenges. *Inorg. Chem.* 49:3557–3566.
19. A Laccase-Wiring Redox Hydrogel for Efficient Catalysis of O2 Electroreduction | The Journal of Physical Chemistry B. .
20. Kato, M., and I. Yagi. 2020. Electrocatalytic Oxygen Reduction at Multinuclear Metal Active Sites Inspired by Metalloenzymes. *e-J. Surf. Sci. Nanotechnol.* 18:81–93.
21. He, F., L. Mi, Y. Shen, X. Chen, Y. Yang, H. Mei, S. Liu, T. Mori, and Y. Zhang. 2017. Driving electrochemical oxygen reduction and hydrazine oxidation reaction by enzyme-inspired polymeric Cu(3,3′-diaminobenzidine) catalyst. *J. Mater. Chem. A*. 5:17413–17420.
22. Thorseth, M.A., C.S. Letko, E.C.M. Tse, T.B. Rauchfuss, and A.A. Gewirth. 2013. Ligand Effects on the Overpotential for Dioxygen Reduction by Tris(2-pyridylmethyl)amine Derivatives. *Inorg. Chem.* 52:628–634.
23. Tahsini, L., H. Kotani, Y.-M. Lee, J. Cho, W. Nam, K.D. Karlin, and S. Fukuzumi. 2012. Electron-Transfer Reduction of Dinuclear Copper Peroxo and Bis-μ-oxo Complexes Leading to the Catalytic Four-Electron Reduction of Dioxygen to Water. *Chemistry – A European Journal*. 18:1084–1093.
24. Fukuzumi, S., L. Tahsini, Y.-M. Lee, K. Ohkubo, W. Nam, and K.D. Karlin. 2012. Factors That Control Catalytic Two- versus Four-Electron Reduction of Dioxygen by Copper Complexes. *J. Am. Chem. Soc.* 134:7025–7035.
25. Solomon, E.I., D.E. Heppner, E.M. Johnston, J.W. Ginsbach, J. Cirera, M. Qayyum, M.T. Kieber-Emmons, C.H. Kjaergaard, R.G. Hadt, and L. Tian. 2014. Copper Active Sites in Biology. *Chemical Reviews*. 114:3659–3853.
26. Vallee, B.L., and R.J. Williams. 1968. Metalloenzymes: the entatic nature of their active sites. *Proc Natl Acad Sci U S A*. 59:498–505.
27. Dicke, B., A. Hoffmann, J. Stanek, M.S. Rampp, B. Grimm-Lebsanft, F. Biebl, D. Rukser, B. Maerz, D. Göries, M. Naumova, M. Biednov, G. Neuber, A. Wetzel, S.M. Hofmann, P. Roedig, A. Meents, J. Bielecki, J. Andreasson, K.R. Beyerlein, H.N. Chapman, C. Bressler, W. Zinth, M. Rübhausen, and S. Herres-Pawlis. 2018. Transferring the entatic-state principle to copper photochemistry. *Nature Chemistry*.
28. Williams, R.J.P. 1995. Energised (entatic) States of Groups and of Secondary Structures in Proteins and Metalloproteins. *European Journal of Biochemistry*. 234:363–381.
29. Jones, S.M., and E.I. Solomon. 2015. Electron Transfer and Reaction Mechanism of Laccases. *Cell Mol Life Sci*. 72:869–883.
30. Comba, P. 2000. Coordination compounds in the entatic state. *Coordination Chemistry Reviews*. 200–202:217–245.
31. Quintanar, L., C. Stoj, T.-P. Wang, D.J. Kosman, and E.I. Solomon. 2005. Role of Aspartate 94 in the Decay of the Peroxide Intermediate in the Multicopper Oxidase Fet3p. *Biochemistry*. 44:6081–6091.
32. Yoon, J., and E.I. Solomon. 2007. Electronic Structure of the Peroxy Intermediate and Its Correlation to the Native Intermediate in the Multicopper Oxidases: Insights into the Reductive Cleavage of the O−O Bond. *J. Am. Chem. Soc.* 129:13127–13136.
33. Augustine, A.J., C. Kjaergaard, M. Qayyum, L. Ziegler, D.J. Kosman, K.O. Hodgson, B. Hedman, and E.I. Solomon. 2010. Systematic Perturbation of the Trinuclear Copper Cluster in the Multicopper Oxidases: The Role of Active Site Asymmetry in Its Reduction of O_2 to H_2O. *J. Am. Chem. Soc.* 132:6057–6067.
34. Carver, C.T., B.D. Matson, and J.M. Mayer. 2012. Electrocatalytic Oxygen Reduction by Iron Tetra-arylporphyrins Bearing Pendant Proton Relays. *J. Am. Chem. Soc.* 134:5444–5447.
35. Plapp, B.V. 2010. Conformational Changes and Catalysis by Alcohol Dehydrogenase. *Arch Biochem Biophys*. 493:3–12.

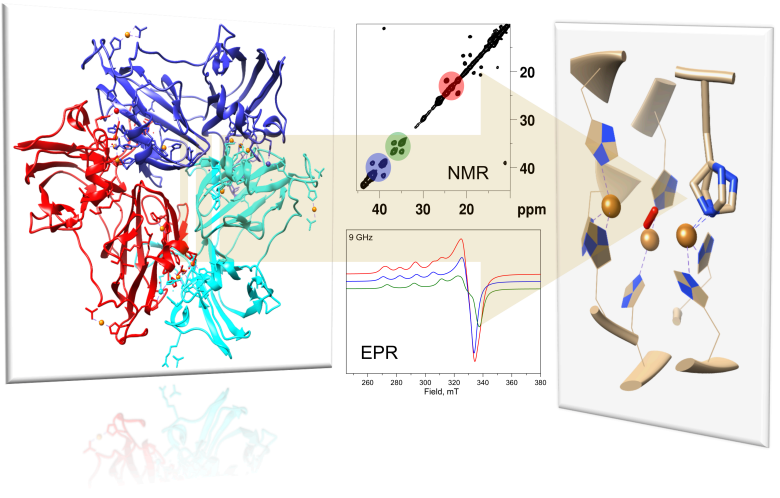
36. Henzler-Wildman, K.A., V. Thai, M. Lei, M. Ott, M. Wolf-Watz, T. Fenn, E. Pozharski, M.A. Wilson, G.A. Petsko, M. Karplus, C.G. Hübner, and D. Kern. 2007. Intrinsic motions along an enzymatic reaction trajectory. *Nature*. 450:838–844.
37. Serrano-Posada, H., S. Centeno-Leija, S.P. Rojas-Trejo, C. Rodríguez-Almazán, V. Stojanoff, and E. Rudiño-Piñera. 2015. X-ray-induced catalytic active-site reduction of a multicopper oxidase: structural insights into the proton-relay mechanism and O_2-reduction states. *Acta Cryst D*. 71:2396–2411.
38. Silva, C.S., P. Durão, A. Fillat, P.F. Lindley, L.O. Martins, and I. Bento. 2012. Crystal structure of the multicopper oxidase from the pathogenic bacterium *Campylobacter jejuni* CGUG11284: characterization of a metallo-oxidase. *Metallomics*. 4:37–47.
39. Machczynski, M.C., E. Vijgenboom, B. Samyn, and G.W. Canters. 2004. Characterization of SLAC: A small laccase from *Streptomyces coelicolor* with unprecedented activity. *Protein Science*. 13:2388–2397.
40. Sherif, M., D. Waung, B. Korbeci, V. Mavisakalyan, R. Flick, G. Brown, M. Abou-Zaid, A.F. Yakunin, and E.R. Master. 2013. Biochemical studies of the multicopper oxidase (small laccase) from Streptomyces coelicolor using bioactive phytochemicals and site-directed mutagenesis. *Microb Biotechnol*. 6:588–597.
41. Lörcher, S., P. Lopes, A. Kartashov, and E.E. Ferapontova. 2013. Direct Bio-electrocatalysis of O_2 Reduction by Streptomyces coelicolor Laccase Orientated at Promoter-Modified Graphite Electrodes. *ChemPhysChem*. 14:2112–2124.
42. Gallaway, J., I. Wheeldon, R. Rincon, P. Atanassov, S. Banta, and S.C. Barton. 2008. Oxygen-reducing enzyme cathodes produced from SLAC, a small laccase from Streptomyces coelicolor. *Biosensors and Bioelectronics*. 23:1229–1235.
43. Langerman, M., and D.G.H. Hetterscheid. 2019. Fast Oxygen Reduction Catalyzed by a Copper(II) Tris(2-pyridylmethyl)amine Complex through a Stepwise Mechanism. *Angewandte Chemie*. 131:13108–13112.
44. Liu, C., H. Lei, Z. Zhang, F. Chen, and R. Cao. 2017. Oxygen reduction catalyzed by a water-soluble binuclear copper(II) complex from a neutral aqueous solution. *Chem. Commun.* 53:3189–3192.
45. Kato, M., K. Kimijima, M. Shibata, H. Notsu, K. Ogino, K. Inokuma, N. Ohta, H. Uehara, Y. Uemura, N. Oyaizu, T. Ohba, S. Takakusagi, K. Asakura, and I. Yagi. 2015. Deprotonation of a dinuclear copper complex of 3,5-diamino-1,2,4-triazole for high oxygen reduction activity. *Physical Chemistry Chemical Physics*. 17:8638–8641.
46. Janusz, G., A. Pawlik, U. Świderska-Burek, J. Polak, J. Sulej, A. Jarosz-Wilkołazka, and A. Paszczyński. 2020. Laccase Properties, Physiological Functions, and Evolution. *International Journal of Molecular Sciences*. 21:966.
47. Sekretaryova, A., S.M. Jones, and E.I. Solomon. 2019. O_2 Reduction to Water by High Potential Multicopper Oxidases: Contributions of the T1 Copper Site Potential and the Local Environment of the Trinuclear Copper Cluster. *J. Am. Chem. Soc.* 141:11304–11314.
48. Toscano, M.D., L.D. Maria, S. Lobedanz, and L.H. Østergaard. 2013. Optimization of a Small Laccase by Active-Site Redesign. *ChemBioChem*. 14:1209–1211.
49. Mate, D.M., and M. Alcalde. 2015. Laccase engineering: From rational design to directed evolution. *Biotechnology Advances*. 33:25–40.
50. Gunne, M., A. Höppner, P.-L. Hagedoorn, and V.B. Urlacher. 2014. Structural and redox properties of the small laccase Ssl1 from *Streptomyces sviceus*. *The FEBS Journal*. 281:4307–4318.
51. Mate, D.M., D. Gonzalez-Perez, M. Falk, R. Kittl, M. Pita, A.L. De Lacey, R. Ludwig, S. Shleev, and M. Alcalde. 2013. Blood Tolerant Laccase by Directed Evolution. *Chemistry & Biology*. 20:223–231.
52. Scheiblbrandner, S., E. Breslmayr, F. Csarman, R. Paukner, J. Führer, P.L. Herzog, S.V. Shleev, E.M. Osipov, T.V. Tikhonova, V.O. Popov, D. Haltrich, R. Ludwig, and R. Kittl. 2017. Evolving stability and pH-dependent activity of the high redox potential *Botrytis aclada* laccase for enzymatic fuel cells. *Sci Rep*. 7:13688.
53. Olbrich, A.C., J.N. Schild, and V.B. Urlacher. 2019. Correlation between the T1 copper reduction potential and catalytic activity of a small laccase. *Journal of Inorganic Biochemistry*. 201:110843.

54. Gabdulkhakov, A.G., O.S. Kostareva, I.A. Kolyadenko, A.O. Mikhaylina, L.I. Trubitsina, and S.V. Tishchenko. 2018. Incorporation of Copper Ions into T2/T3 Centers of Two-Domain Laccases. *Molecular Biology*. 52:23–29.
55. Gabdulkhakov, A., I. Kolyadenko, O. Kostareva, A. Mikhaylina, P. Oliveira, P. Tamagnini, A. Lisov, and S. Tishchenko. 2019. Investigations of Accessibility of T2/T3 Copper Center of Two-Domain Laccase from Streptomyces griseoflavus Ac-993. *International Journal of Molecular Sciences*. 20:3184.
56. Trubitsina, L.I., S.V. Tishchenko, A.G. Gabdulkhakov, A.V. Lisov, M.V. Zakharova, and A.A. Leontievsky. 2015. Structural and functional characterization of two-domain laccase from *Streptomyces viridochromogenes*. *Biochimie*. 112:151–159.
57. Palmer, A.E., S.K. Lee, and E.I. Solomon. 2001. Decay of the Peroxide Intermediate in Laccase: Reductive Cleavage of the O−O Bond. *J. Am. Chem. Soc.* 123:6591–6599.
58. Gupta, A., I. Nederlof, S. Sottini, A.W.J.W. Tepper, E.J.J. Groenen, E.A.J. Thomassen, and G.W. Canters. 2012. Involvement of Tyr108 in the Enzyme Mechanism of the Small Laccase from Streptomyces coelicolor. *Journal of the American Chemical Society*. 134:18213–18216.
59. Kielb, P., H.B. Gray, and J.R. Winkler. 2020. Does Tyrosine Protect *S. Coelicolor* Laccase from Oxidative Degradation? DOI: 10.26434/chemrxiv.12671612.v1
60. Tepper, A.W.J.W., S. Milikisyants, S. Sottini, E. Vijgenboom, E.J.J. Groenen, and G.W. Canters. 2009. Identification of a Radical Intermediate in the Enzymatic Reduction of Oxygen by a Small Laccase. *J. Am. Chem. Soc.* 131:11680–11682.
61. Skálová, T., J. Dohnálek, L.H. Østergaard, P.R. Østergaard, P. Kolenko, J. Dušková, A. Štěpánková, and J. Hašek. 2009. The Structure of the Small Laccase from *Streptomyces coelicolor* Reveals a Link between Laccases and Nitrite Reductases. *Journal of Molecular Biology*. 385:1165–1178.
62. Matera, I., A. Gullotto, S. Tilli, M. Ferraroni, A. Scozzafava, and F. Briganti. 2008. Crystal structure of the blue multicopper oxidase from the white-rot fungus *Trametes trogii* complexed with p-toluate. *Inorganica Chimica Acta*. 361:4129–4137.
63. Enguita, F.J., L.O. Martins, A.O. Henriques, and M.A. Carrondo. 2003. Crystal Structure of a bacterial endospore coat component a laccase with enhanced thermostability properties. *J. Biol. Chem*. 278:19416–19425.
64. Augustine, A.J., L. Quintanar, C.S. Stoj, D.J. Kosman, and E.I. Solomon. 2007. Spectroscopic and Kinetic Studies of Perturbed Trinuclear Copper Clusters: The Role of Protons in Reductive Cleavage of the O−O Bond in the Multicopper Oxidase Fet3p. *J. Am. Chem. Soc.* 129:13118–13126.
65. Heppner, D.E., C.H. Kjaergaard, and E.I. Solomon. 2014. Mechanism of the Reduction of the Native Intermediate in the Multicopper Oxidases: Insights into Rapid Intramolecular Electron Transfer in Turnover. *J. Am. Chem. Soc.* 136:17788–17801.
66. Tian, S., S.M. Jones, and E.I. Solomon. 2020. Role of a Tyrosine Radical in Human Ceruloplasmin Catalysis. *ACS Cent. Sci.*
67. Quintanar, L., J. Yoon, C.P. Aznar, A.E. Palmer, K.K. Andersson, R.D. Britt, and E.I. Solomon. 2005. Spectroscopic and Electronic Structure Studies of the Trinuclear Cu Cluster Active Site of the Multicopper Oxidase Laccase: Nature of Its Coordination Unsaturation. *J. Am. Chem. Soc.* 127:13832–13845.
68. Bertini, I., C. Luchinat, G. Parigi, and E. Ravera. 2017. NMR of paramagnetic molecules: applications to metallobiomolecules and models. Second edition. Amsterdam: Elsevier.
69. Kambe, K. 1950. On the Paramagnetic Susceptibilities of Some Polynuclear Complex Salts. *J. Phys. Soc. Jpn.* 5:48–51.
70. Gruber, S.J., C.M. Harris, and E. Sinn. 1968. Metal Complexes as Ligands. VI. Antiferromagnetic Interactions in Trinuclear Complexes Containing Similar and Dissimilar Metals. *The Journal of Chemical Physics*. 49:2183–2191.
71. Sinn, E. 1970. Magnetic exchange in polynuclear metal complexes. *Coordination Chemistry Reviews*. 5:313–347.
72. Lee, S.-K., S.D. George, W.E. Antholine, B. Hedman, K.O. Hodgson, and E.I. Solomon. 2002. Nature of the Intermediate Formed in the Reduction of O_2 to H_2O at the Trinuclear Copper Cluster Active Site in Native Laccase. *J. Am. Chem. Soc.* 124:6180–6193.

73. Machczynski, M.C., and J.T. Babicz. 2016. Correlating the structures and activities of the resting oxidized and native intermediate states of a small laccase by paramagnetic NMR. *Journal of Inorganic Biochemistry*. 159:62–69.
74. Griffith, J.S. 1972. On the general theory of magnetic susceptibilities of polynuclear transition-metal compounds. In: Structure and Bonding. Berlin, Heidelberg: Springer Berlin Heidelberg. pp. 87–126.
75. M. Ubbink, J. A. R. Worrall, G. W. Canters, E. J. J. Groenen, and M. Huber. 2002. Paramagnetic Resonance of Biological Metal Centers. *Annual Review of Biophysics and Biomolecular Structure*. 31:393–422.
76. Kurland, R.J., and B.R. McGarvey. 1970. Isotropic NMR shifts in transition metal complexes: The calculation of the fermi contact and pseudocontact terms. *Journal of Magnetic Resonance (1969)*. 2:286–301.
77. McConnell, H.M., and R.E. Robertson. 1958. Isotropic Nuclear Resonance Shifts. *The Journal of Chemical Physics*. 29:1361–1365.
78. Bertini, I., C. Luchinat, and G. Parigi. 2002. Magnetic susceptibility in paramagnetic NMR. *Progress in Nuclear Magnetic Resonance Spectroscopy*. 40:249–273.
79. Patt, S.L., and B.D. Sykes. 1972. Water Eliminated Fourier Transform NMR Spectroscopy. *J. Chem. Phys.* 56:3182–3184.
80. Banci, L., I. Bertini, and C. Luchinat. 1990. The ^{1}H NMR parameters of magnetically coupled dimers—The Fe2S2 proteins as an example. In: Bioinorganic Chemistry. Berlin, Heidelberg: Springer. pp. 113–136.
81. Asokan, A., B. Varghese, and P.T. Manoharan. 1999. Synthesis, Structure, Magnetic Properties, and ^{1} H NMR Studies of a Moderately Antiferromagnetically Coupled Binuclear Copper(II) Complex. *Inorganic Chemistry*. 38:4393–4399.
82. Solomon, E.I., A.J. Augustine, and J. Yoon. 2008. O_2 Reduction to H_2O by the multicopper oxidases. *Dalton Trans.* 3921–3932.
83. Jeener, J., B.H. Meier, P. Bachmann, and R.R. Ernst. 1979. Investigation of exchange processes by two-dimensional NMR spectroscopy. *J. Chem. Phys.* 71:4546–4553.
84. Santos, H., D.L. Turner, A.V. Xavier, and J. le Gall. 1984. Two-dimensional NMR studies of electron transfer in cytochrome c3. *Journal of Magnetic Resonance (1969)*. 59:177–180.
85. Bertini, I., C. Luchinat, G. Parigi, and R. Pierattelli. 2005. NMR Spectroscopy of Paramagnetic Metalloproteins. *ChemBioChem*. 6:1536–1549.
86. Ciofi-Baffoni, S., A. Gallo, R. Muzzioli, and M. Piccioli. 2014. The IR-^{15}N-HSQC-AP experiment: a new tool for NMR spectroscopy of paramagnetic molecules. *Journal of Biomolecular NMR*. 58:123–128.
87. Bax, A., R.H. Griffey, and B.L. Hawkins. 1983. Correlation of proton and nitrogen-15 chemical shifts by multiple quantum NMR. *Journal of Magnetic Resonance (1969)*. 55:301–315.
88. Bertarello, A., L. Benda, K.J. Sanders, A.J. Pell, M.J. Knight, V. Pelmenschikov, L. Gonnelli, I.C. Felli, M. Kaupp, L. Emsley, R. Pierattelli, and G. Pintacuda. 2020. Picometer Resolution Structure of the Coordination Sphere in the Metal-Binding Site in a Metalloprotein by NMR. *J. Am. Chem. Soc.* 142:16757–16765.

Chapter 2

Chemical exchange at the tri-nuclear copper center of small laccase from *Streptomyces coelicolor*



This chapter is published as:
Dasgupta, R., K.B.S.S. Gupta, F. Nami, H.J.M. de Groot, G.W. Canters, E.J.J. Groenen, and M. Ubbink. 2020. Chemical exchange at the trinuclear copper center of small laccase from *Streptomyces coelicolor*. *Biophysical Journal*. 119:9–14. DOI: http://doi.org/10.1016/j.bpj.2020.05.022

EPR spectroscopy was performed and the data were analyzed by F. Nami, G. W. Canters and E. J. J. Groenen.

The tri-nuclear copper center (TNC) of laccase reduces oxygen to water with very little overpotential. The arrangement of the coppers and ligands in the TNC is known from many crystal structures, yet information about possible dynamics of the ligands is absent. Here, we report dynamics at the TNC of small laccase from *S. coelicolor* using paramagnetic NMR and EPR spectroscopy. Fermi contact-shifted resonances tentatively assigned to histidine Hδ1, display two-state chemical exchange with exchange rates in the order of 100 s^{-1}. In the EPR spectra, at least two forms are observed with different g_z values. It is proposed that the exchange processes reflect rotational motion of histidine imidazole rings that coordinate the coppers in the TNC.

2.1 Introduction

Laccases reduce dioxygen to two water molecules at the tri-nuclear copper center (TNC) by oxidizing a broad range of substrates at the type 1 (T1) site, with very little overpotential,(1) making them potentially interesting proteins for enzymatic biofuel cells. The TNC (Figure 2.1d and 1.4a) comprises a type 3 (T3) site with two coppers and a type 2 (T2) site with a single copper. The T1 site is linked to the TNC via a conserved HCH motif and the two are separated by ~ 13 Å (Figure 1.3). This conserved motif provides a fast route for electron transfer from the substrate via the T1 site to the TNC for O_2 reduction to water. Crystal structures of laccases (2–8) have helped in modelling the catalytic mechanism of O_2 reduction.(2, 4) The current model for the catalytic mechanism for O_2 reduction at the TNC is summarized in Chapter 1 (Figure 1.3). In brief, the resting oxidized (RO) state is converted to fully reduced (FR) state by receiving four electrons from substrate oxidized at the T1 site. The FR state can bind oxygen and is converted to peroxide intermediate (PI) state by transferring 2 electrons to the oxygen molecule hence forming a peroxide. The PI state is converted to native intermediate (NI) state, in which the oxygen bond has been cleaved and all the coppers in the TNC are coupled via an oxygen atom. This NI state can slowly be converted to RO state in the absence of the substrate or directly go into the FR state in the presence of the substrate.(2–4)

Although much is known about the mechanism through different models, mimicking the active site to design artificial catalyst is notoriously difficult. The model compounds reported so far do not have the catalytic efficiency of the enzyme.(9–12) Usually dynamics associated with the residues at the active site is ignored while designing artificial catalyst although it was reported that motions can be important to attain a conformation that lowers the energy barrier for electron and proton transfer processes.(13–16) Determining such motions in laccase might provide insight into designing a functional framework for an efficient artificial catalyst. Here, we report

the presence of conformational exchange at the TNC on the millisecond timescale, ascribed to motions of the copper coordinating imidazole rings of histidine residues.

2.2 Results and discussions

A mutant of small laccase from *S. coelicolor* (SLAC) was used, in which the T1 site is copper depleted by the C288S mutation (SLAC-T1D).(8) The theoretical MW of the holoenzyme in its monomeric form is 37.05 kDa. The purified protein was found to run at an apparent MW of 75 kDa and 37 kDa in SDS PAGE (Figure S2.1) but in solution it has a MW ~ 105 kDa, as determined by size exclusion chromatography linked with multi angle light scattering (SEC-MALS). Thus, it is concluded that the enzyme is in its trimer form, as observed in crystal structure.(17)

Identification of nitrogen attached protons

The 1D ^{1}H WEFT-NMR (18) experiment enhances signals of protons experiencing rapid paramagnetic relaxation. The resulting NI state spectrum of SLAC-T1D (Figure 2.1a) shows large Fermi contact shifts (FCS) (> 21 ppm) for many resonances. The spectrum is very similar to the one reported by Machczynski *et al.*, (2004 and 2016) (6, 19) confirming that TNC is fully formed. Fermi contact interactions fall off rapidly with the number of bonds between metal and nucleus,(20) indicating that the resonances with large shifts must derive from sidechains of the copper coordinating amino acid residues, which are histidine ligands.(21, 22) Since the anisotropy of the copper sites in proteins is reported to be low,(20) the contribution of pseudo-contact shifts (PCS) to the observed chemical shift is much smaller than that of the FCS, though not necessarily negligible in all cases (maximal PCS estimations are provided in Table S2.5 using equation 1.11).

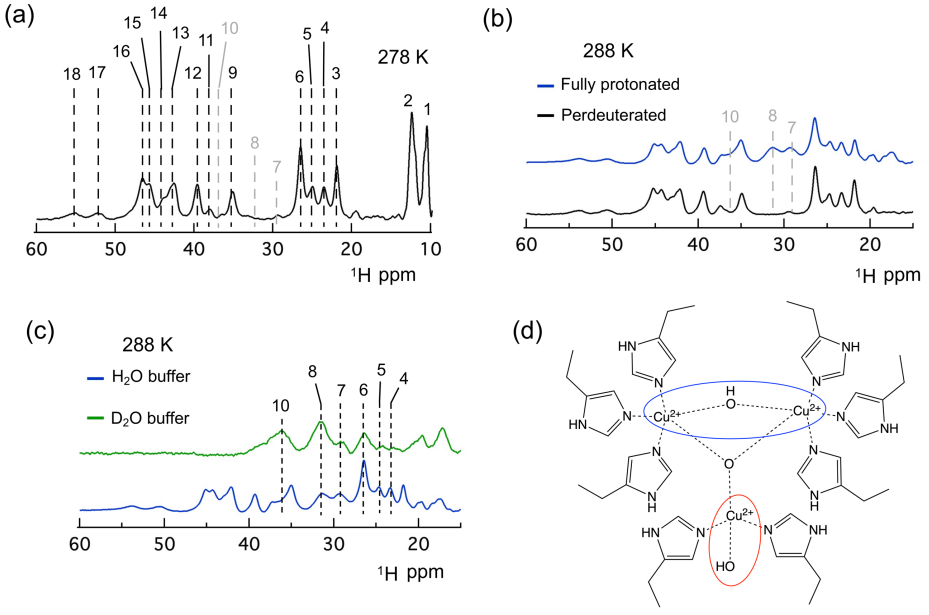


***Figure 2.1**. Analysis of the 1D ¹H spectra. (a) WEFT NMR spectra of perdeuterated protein with amide proton back-exchanged at 278 K depicting the part of the spectrum showing signals that are strongly shifted by Fermi contact effects. The resonance 7, 8 and 10 are indicated to shows their positions from panel b and c; (b) 1D WEFT spectra at 288 K comparing samples that were fully protonated (blue) or perdeuterated with back-exchange (black), both in H_2O buffer. Resonances 7, 8 and 10 are indicated which are derived from protons attached to carbons; (c) 1D WEFT spectra at 288 K comparing fully protonated samples in D_2O buffer (green) and H_2O buffer (blue), showing the extensive loss of resonances due to exchange of protons by deuterons and (d) Schematic representation of a tri-nuclear copper center of small laccase in the NI state. The T3 and T2 sites are marked by blue and red ovals. Hδ1 His ring protons are shown.*

Utilizing different deuteration schemes, resonances from protons attached to nitrogen/oxygen atoms can be distinguished from those attached to carbon, being exchangeable and non-exchangeable, respectively. For a per-deuterated sample that was allowed to back-exchange the exchangeable deuterons to protons, resonances 7 and 8 were lost from the spectrum, indicating that they derive from non-exchangeable, carbon-attached protons. The remaining resonances appear in the spectrum of this sample, indicating that they are from exchangeable protons, most likely attached to nitrogen atoms (Figure 2.1b). A normal, protonated sample in which exchangeable protons were replaced with deuterons by bringing the sample in D_2O yields a spectrum in which resonances 7, 8 and 10 are prominent, supporting the observation that the equivalent protons are attached to carbons (Figure 2.1c). For resonances 4, 5 and 6

(Figure 2.1a and c) the assignment is less clear, they may represent overlapping signals from exchangeable and non-exchangeable protons (Figure 2.1b, c).

Chemical exchange at the TNC

To probe the dynamics at the TNC, $^1H - ^1H$ exchange spectroscopy (EXSY) (23) was used with solvent pre-saturation during interscan delay (Figure 1.5b). We observe multiple cross peaks between the FCS resonances (> 22 ppm, Figure S2.2). NOE and exchange cross peaks were distinguished by comparing the temperature dependence of the cross-peak intensities, normalized by the diagonal peak intensities. For the temperature range used in the present work (278 – 303 K) NOE cross peak intensity will be independent with respect to temperature, while the EXSY cross peak intensity will show an increase with increasing temperature (Figure S2.2 and Figure 2.2a and b).(20) The cross peaks between resonances 3 & 5, 9 & 11, and 12 & 13 arise from chemical exchange, whereas the cross peak between resonance 12 and a resonance at 11 ppm is a NOE cross peak (Figure S2.2). Resonances between 27 and 30 ppm belong to protons attached to carbon atoms (Figure 2.1a, b and c). Cross-peaks were also observed between resonance pairs of 18-16 and 17-15 at very short mixing times of 1 ms and 2 ms and at 303 K (Figure S2.4). Cross peaks are also observed between the resonances in the spectra region from 11 to 22 ppm (Figure S2.5). However, due to the low S/N it could not be established whether these cross peaks are due to chemical exchange or NOE.

Table 2.1. *Kinetic parameters and equilibrium constants. The values [*] were obtained from the best fit (Figure S2.3) of the cross peak and diagonal intensities of the resonance pairs 3-5, 9-11 and 13-12 to equation S2.1. The rate constants k_A and k_B are the forward and reverse rates and k_{ex} is the total exchange rate ($k_A + k_B$). K_{eq} is the equilibrium constant obtained from the ratio of the diagonal peak integral volume at τ_{mix} = 0 ms and was constrained during fitting.*

Temp. (K)	3-5				9-11				13-12			
	(s^{-1})				(s^{-1})				(s^{-1})			
	k_A	k_B	k_{ex}	K_{eq}	k_A	k_B	k_{ex}	K_{eq}	k_A	k_B	k_{ex}	K_{eq}
293	34	45	79	0.76	48	61	109	0.78	15	29	44	0.52
298	33	62	95	0.53	29	91	120	0.32	29	34	63	0.85
303	46	81	127	0.56	48	127	175	0.37	22	44	66	0.50
308	68	115	183	0.59	81	160	241	0.50	36	48	84	0.75

[*] Error is estimated to be ~ ± 5% from duplicate measurements.

Thus, in the further analysis we focussed on the exchange peaks between resonances 3 – 5, 9 – 11 and 13 – 12. The chemical exchange is in the slow-exchange regime because a distinct resonance is observed for each state. The forward and backward chemical-exchange rates were determined for the three pairs of resonances using equations derived previously (equations S2.1 to S2.4, see also Figure S2.3).(24) Table 2.1 summarizes the exchange rates obtained from fittings of the ratio of the cross by diagonal peak intensities at different temperatures. The equilibrium constant is about 0.5 and does not change much in the applied temperature range, but the exchange rates increase about two-fold between 293 and 308 K for each resonance pair, allowing an estimation of the activation energy of the transition between the two states. The observed activation energies for the transitions of resonance 3 to 5, 9 to 11 and 13 to 12 are 43 ± 4 kJ/mol, 42 ± 7 kJ/mol and 30 ± 6 kJ/mol, respectively (Figure 2.2c).

Temperature dependence of proton chemical shift

Temperature dependence of the FCS resonances (Figure S2.10a) showed three types of behaviour, strong-Curie (decreasing hyperfine coupling with increasing temperature), for resonances 11, 13, 16, 15, 18 and 17, weak-anti-Curie (increasing hyperfine coupling with increasing temperature), for resonances 3, 6, 7 and 8, and no-Curie (temperature independent), for resonances 4, 5, 9 and 12, suggesting that there is more than one coupled copper pair, in line with previous reports.(19, 25) The quantitative analysis of the coupling scheme for the temperature dependence of the FCS resonances (Figure S2.10) is described in section 1.3 of Chapter 1. Using equation 1.4, the J coupling values were obtained from the temperature dependence of the FCS resonances, assuming a general triad ($J_{13} \neq J_{12} \neq J_{23}$ for NI form of SLAC-T1D, yielding $J_{12} = -120$ cm^{-1}, $J_{13} = -80$ cm^{-1} and $J_{23} = -150$ cm^{-1}, where J_{23} is the coupling between the T3 coppers (Figure S2.10b and c). The above values were obtained by procedure described in Machczynski *et al.*,(2016) (19) and it was observed that the values reported gave an excellent fit.

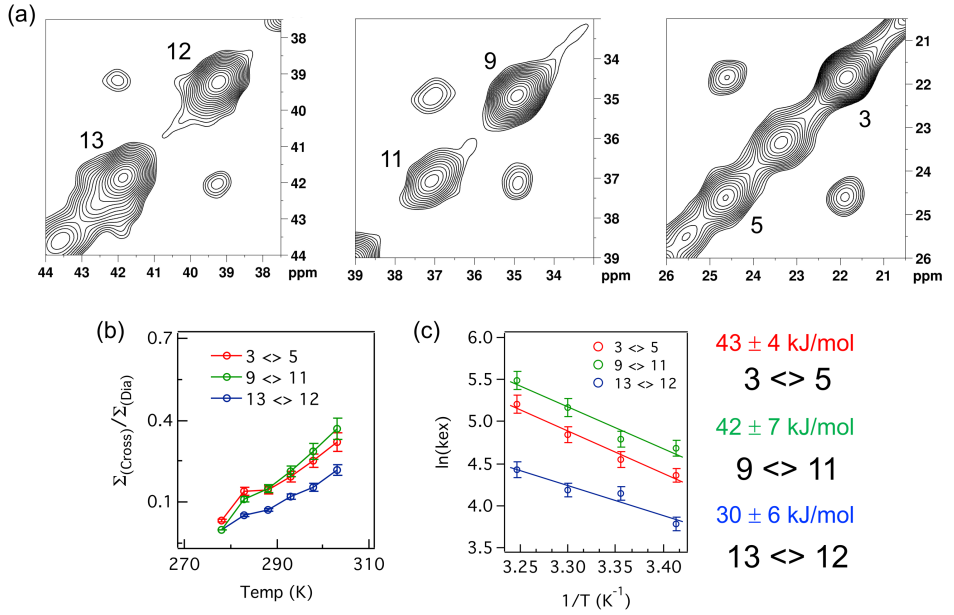


Figure 2.2. *Exchange effects. (a) 2D ^{1}H–^{1}H EXSY spectra of the region between > 22 ppm, showing resonances with exchange cross peaks. The spectrum was recorded at 288 K at 14.2 T (600 MHz). The numbering of resonances is equivalent to Figure 2.1a. (b) Temperature dependence of the sum of cross peak intensity, normalized with the sum of diagonal peak intensity of the resonances 3 – 5, 9 – 11 and 13 – 12 in red, green and blue, respectively. The error bars are calculated from the noise level. (c) Arrhenius plot and the respective activation energies for the exchange processes 3 ↔ 5, 9 ↔ 11 and 13 ↔ 12. The error is one standard deviation.*

Analysis of crystal structures

The FCS for the two states differ by ~ 3 ppm, a relatively small change for an absolute FCS in the order of 20-35 ppm, indicating a small change in the unpaired electron-spin density on the proton. In combination, these observations agree with an assignment of the resonances to the protons linked to the Nδ1 atoms of the imidazole rings of histidine ligands that coordinate the coppers in the T3 and T2 sites. Such protons are exchangeable with the solvent but the exchange is slow enough for the resonance to be observed because all but one Nδ1 atom in the TNC are hydrogen bonded (Table S2.3). These hydrogens will experience large FCS, being very close to the copper ions. A rearrangement of the imidazole ring, such as a small rotation, can leave the coordination intact, yet cause a slight change in spin density and thus in the FCS. An inspection of crystal structures of prokaryotic multicopper oxidases (3-domain monomeric laccases) yielded two examples (PDB: 3zx1 and 2xu9) (26, 27) in which imidazole ring motions at the T3 site were captured (Figure S2.6). In 3zx1 (resolution

1.95 Å) two conformations of the His-182 ring are observed with $\chi 2$ angles 154° and 86°, yet maintaining a coordination bond with the T3-Cu.(26) In structure 2xu9 (resolution 1.5 Å) the equivalent ligand, His-137, also displays two conformations, one of which has no coordination bond with T3-Cu.(27) In this case also the $\chi 1$ angle differs.

To estimate how much motion of the His rings could be accommodated at the TNC of SLAC, we modelled the change in distance between the T3-Cu and His Nε2 of the ligand His158, equivalent to His182.A in PDB 3zx1, as a function of the $\chi 2$ dihedral angle, using PDB 3cg8 (resolution 2.68 Å).(17) Allowing for a somewhat arbitrary maximal increase of 0.05 Å of the distance to maintain the coordination bond, avoiding clashes with surrounding atoms and maintaining the hydrogen bond of the Nδ1, the $\chi 2$ angle of His-158 can still assume values between 100° and 140° (Figure S2.6). Similar analysis was done for all the coordinating His at the TNC (Figure S2.7). In each case the imidazole ring has considerable freedom to rotate. An analysis of $\chi 2$ angles for a variety of 2-domain and 3-domain laccase structures reflects this freedom (Figure S2.8). This suggests that such ring motions might be responsible for the observed exchange behaviour. The detailed method is given in the supporting information.

Electron paramagnetic resonance spectroscopy

The NMR observations show the presence of at least 3 chemical exchange process at the TNC and we wondered whether one of it belongs to a ligand at the T2 site. If heterogeneity is present at the T2 site, distinct sites may show up in the EPR spectrum for the frozen protein. The low temperature EPR spectrum of SLAC-T1D yields a signal for the T2 site, while the coppers in the T3 site are anti-ferromagnetically coupled and thus EPR silent. The 9.5 GHz (X-band) spectrum at 40 K (Figure 2.3) reveals the copper hyperfine structure in the low-field part of the spectrum, the g_z region from 265 to 320 mT, be it not a simple pattern of four equidistant lines. In addition to the copper hyperfine structure, the spectrum shows a small but resolved hyperfine structure around 328 mT, which derives from the interaction of the copper electron spin with the nitrogen nuclear spins of the copper-coordinating histidine ligands. To interpret the X-band spectrum, we make use of the 275 GHz EPR spectrum taken at 10 K (Figure 2.3). At this high microwave frequency, the copper and nitrogen hyperfine structure is masked by line broadening due to *g*-strain. The higher *g*-resolution at this frequency clearly reveals two distinct signals in the g_z region, at 8.37 and 8.77 T, corresponding to $g_z = 2.352$ and $g_z = 2.246$. Starting from these values we simulated the EPR spectra at both microwave frequencies as the sum of the spectra of two components (Figure 2.3), which differ in the g_y, g_z, and A_z spin Hamiltonian parameters (Table S2.4). The separate contributions of the two components to the simulated spectra are shown in Figure S2.9. The parameters of the

major component 1 correspond to those previously reported for the T2 site of SLAC-T1D,(7) while the parameters of minor component 2 resemble those of the T2 site of multicopper oxidase from different organisms (Table S2.6 and references therein). The fraction of the minor component varies for different preparations, and is commonly between 30 and 40%. We believe that the distinct EPR signals for SLAC-T1D are evidence of heterogeneity in the T2 site of the TNC, in line with the observation of multiple states of the imidazole rings by NMR. The EPR spectrum at 275 GHz showing the difference in the value of g_z supports the presence of His ring motion at the T2 site, as a rearrangement/rotation of an imidazole ring will affect the delocalization of spin density between copper and the imidazole, thereby changing the spin density on the copper to which, through spin-orbit coupling, the g_z value is most sensitive.(28)

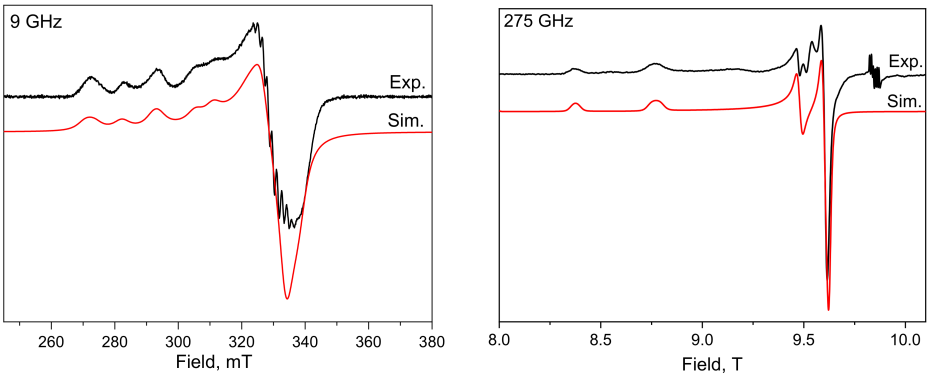


Figure 2.3. *Experimental and simulated EPR spectra of the resting form of SLAC-T1D (as purified) at microwave frequencies of 9.5 GHz and 275 GHz. The small signals around 9.85 T in the experimental spectrum at 275 GHz arise from a Mn (II) impurity in the sample. The hyperfine interaction of the copper electron spin with the nitrogen nuclei of the copper-coordinating histidine ligands is not considered for the simulations. The experimental and simulation details are summarized in supplementary material.*

2.3 Conclusion

NMR spectroscopy showed that at least 3 independent chemical exchange processes are present at the TNC and EPR spectroscopy showed that heterogeneity exists at the T2 site. We propose that in the NI state of SLAC there is chemical exchange at the TNC and this is due to the ring motions of coordinating histidine residues. The motions appear not to be concerted. Though the activation energies are similar within their error ranges, the exchange rates differ significantly (Table 2.1), indicating independent processes. Such motions could well be a general property of histidine rings, much like ring flips of aromatic residues. His ring flips in the influenza A M2 proton channel are associated with proton conduction, with an energy barrier greater than 59 kJ/mol.(29) A fast His flip (~2000 s^{-1}) was described in detail for the surface exposed, non-coordinating His61 in plastocyanin from *Anabaena variabilis*.(30) Here, the imidazole rings are not flipping (i.e. not rotating by 180°) because that would break the coordination bond, yet clearly two states exist, separated by a considerable activation barrier, perhaps representing two ring orientations with favourable coordination properties. It needs to be determined whether the same motions are present in wt SLAC. Given their local nature and the similarity in structures of T1D and wt laccases,(17, 19) it seems quite likely that also in wt SLAC such motions occur. Whether evolution has used His ring motions to the benefit of catalysis by SLAC, for example as a gatekeeper or for proton transfer, remains to be established.

2.4 Supporting Information

Production and purification of SLAC-T1D

SLAC-T1D was expressed and purified as described previously.(6, 8) Briefly, for fully protonated sample, pET20b plasmid containing the gene encoding SLAC C288S (type 1 depleted mutant) was transformed in BL21 pLysS strain of *Escherichia coli*. A colony of transformed cells was used to inoculate 25 mL lysogeny broth and the suspension was incubated overnight at 37°C. This preculture was diluted in 500 mL 2x YT medium, which was incubated at 30°C to an optical density at 600 nm of 1.0 to 1.5. Gene expression was induced with 0.5 mM IPTG. Then, the temperature was reduced to 25°C and cells were harvested after a further incubation during 18 hrs. For perdeuterated samples, the preculture was prepared in 25 mL of M9 minimal medium in water, which was transferred to 25 mL of M9 medium prepared in 99.99% D_2O for an overnight preculture. The latter was used to inoculate 500 mL D_2O-M9 minimal medium containing ^{15}N ammonium chloride and D-glucose-1,2,3,4,5,6,6-d7 as nitrogen and carbon sources respectively. Gene expression and protein harvesting was done as that of the fully protonated sample. Purification was done in 10 mM sodium phosphate buffer pH 7.3 (buffer A) for fully protonated and perdeuterated (with back-exchange of amide protons) samples.(6, 8) Briefly, the harvested cells were lysed with a French press in buffer A. After centrifugation, the soluble fraction was incubated with 1 mM $CuSO_4$ for 2-3 hrs at 4°C. Then, the soluble fraction was dialyzed against 5 L of buffer A for 18 hrs at 4°C. EDTA (1 mM) was added to the soluble fraction and dialyzed against 5 L of buffer A twice for 18 hrs at 4°C. The soluble fraction was pooled and loaded on a 10 ml DEAE column preequilibrated with buffer A and eluted with a gradient of 0-500 mM NaCl in buffer A in 40 column volumes. Fractions with green colour were pooled and concentrated using a Proteus X-spinner 10 kDa concentrator. For final purification the concentrated protein was loaded on a 120 mL Superdex 75 gel filtration column preequilibrated with buffer A with 150 mM NaCl. Green fractions were pooled, concentrated, buffer exchanged to buffer A at pH 6.8 and stored at -80°C after flash freezing for future use. The yield was 200 mg/L and 240 mg/L for fully protonated and perdeuterated samples respectively. After heating the samples at 95°C for 30s the purity was checked using 12.5% SDS PAGE gel, as shown in Figure. S2.1 where a band at ~ 37 kDa and ~ 75 kDa is observed belonging to monomer (M) and dimer (D) respectively. Under native condition from size exclusion chromatography with multi-angle light scattering (SEC-MALS) the molecular weight of the protein was ~ 105 kDa, which suggests the presence of a trimeric form.

NMR spectroscopy

Samples contained ~ 800 μM SLAC-T1D in 10 mM sodium phosphate buffer pH 6.8 with 10% D_2O for the samples that were fully protonated or perdeuterated with back-exchange. For samples in D_2O, the buffer was changed with a Proteus X-spinner 10 kDa concentrator to 10 mM sodium phosphate buffer pH 6.8 prepared in 99.99% D_2O. Experiments were done on a Bruker AV-III HD 600 MHz NMR spectrometer equipped with a TXI cryoprobe. 1D WEFT experiments were done with a WEFT delay and an interscan delay of 100 ms each (Figure 1.5a). Inversion recovery experiments to measure the spin-lattice relaxation rate were done using standard pulse sequence of d1–180–d2–90–acq where d1 is the interscan delay, which was set to 100 ms, d2 is the recovery time which was from 0.1 ms to 60 ms and acq is the acquisition. The intensity of the resonance vs the d2 time gives an exponential curve which was fitted with equation $I(t) = I(0)\left(1 - 2e^{(-t/T1)}\right)$, where $I(0)$ is the intensity at thermal equilibrium, t is the recovery time and T1 is the spin-lattice relaxation time. The inverse of the T1 relaxation time gives the spin-lattice relaxation rate and is summarized for the chemical exchange resonance pairs in Table S2.2. 2D ^{1}H-^{1}H EXSY(23, 31) experiments were recorded with an interscan delay of 200 ms and mixing times of 1, 2, 3.5, 5, 7 and 9 ms. For the study of the temperature dependence the samples were incubated at every temperature for 15 min. prior to data collection. The integral volume of cross peaks and diagonal peaks was obtained using TOPSPIN 4.0.5 (Bruker). The mixing time dependent integral volume profiles were fitted using equations S1-S4 (24) with IGOR Pro 6.3.7 to obtain the exchange rates. The fitting was done by constraining the K_{eq} (Table 2.1 of the main text) to the value of the ratio of the diagonal integral volume at zero mixing time.(24) The spin-lattice relaxation rates used in the fitting were obtained from inversion recovery experiments.

EPR spectroscopy

Sample concentration was 400 μM and 3 mM for measurement at 9.5 GHz and 275.7 GHz respectively, in 100 mM sodium phosphate buffer, pH 6.8. Measurements at 9.5 GHz were performed at 40 K with a microwave power of 100 nW and modulation amplitude of 0.5 mT. For measurements at 275.7 GHz these parameters were 10 K, 100 nW and 2.4 mT, respectively. The spectra were simulated using EasySpin (32) for frozen solutions.

Modelling studies to determine the freedom of His ring motion in the tri-nuclear copper center (TNC)

PDB 3cg8 (17) was used to study the extent of His ring rotation allowed at the TNC. Using UCSF Chimera (33) software, the $\chi 2$ dihedral angle of the His residues coordinating the copper at the TNC were changed. Applying the conditions

that there are no clashes with the surrounding atoms, the hydrogen bond (Table S3) with the His $N^{\delta 1}$ is kept and the distance between His $N^{\delta 1}$ – Cu(II) is ≤ 0.05 Å to maintain the coordination bond, the range of the allowed value of the $\chi 2$ dihedral angle was determined.

Equations to obtain exchange rates

$$\frac{\sum \text{Cross}}{\sum \text{Dia}} = \frac{I_{ij} + I_{ji}}{I_{ii} + I_{jj}} \ (24) \tag{S2.1}$$

where $\sum$ Cross and $\sum$ Dia is the summation of integral volumes of the cross peaks and diagonal peaks, respectively and,

$$I_{ii} = I_{i0}\frac{-(\lambda_2 - a_{ii})\mathrm{e}^{-\lambda_1\tau_m} + (\lambda_1 - a_{ii})\mathrm{e}^{-\lambda_2\tau_m}}{\lambda_1 - \lambda_2}$$
$$I_{jj} = I_{j0}\frac{-(\lambda_2 - a_{jj})\mathrm{e}^{-\lambda_1\tau_m} + (\lambda_1 - a_{jj})\mathrm{e}^{-\lambda_2\tau_m}}{\lambda_1 - \lambda_2} \tag{S2.2}$$

$$I_{ij} = I_{i0}\frac{a_{ji}\mathrm{e}^{-\lambda_1\tau_m} - a_{ji}\mathrm{e}^{-\lambda_2\tau_m}}{\lambda_1 - \lambda_2}$$
$$I_{ji} = I_{j0}\frac{a_{ij}\mathrm{e}^{-\lambda_1\tau_m} - a_{ij}\mathrm{e}^{-\lambda_2\tau_m}}{\lambda_1 - \lambda_2} \tag{S2.3}$$

$$\lambda_{1,2} = \frac{1}{2}\left\{(a_{ii} + a_{jj}) \pm \sqrt{(a_{ii} - a_{jj})^2 + 4k_{ij}k_{ji}}\right\} \tag{S2.4}$$

$$a_{ii} = R_i + k_{ij};\ a_{jj} = R_j + k_{ji};\ a_{ij} = -k_{ji};\ a_{ji} = -k_{ij}$$

Where I_{ii}, I_{jj} are the intensities of the diagonal peaks, I_{i0}, I_{j0} are the initial diagonal intensities at 0 ms mixing time, I_{ij}, I_{ji} are the intensities of the cross peaks, k_{ij}, k_{ji} are the forward and reverse exchange rates, respectively and R_i, R_j are the spin-lattice relaxation rates of the two sites.

Supporting figures and tables

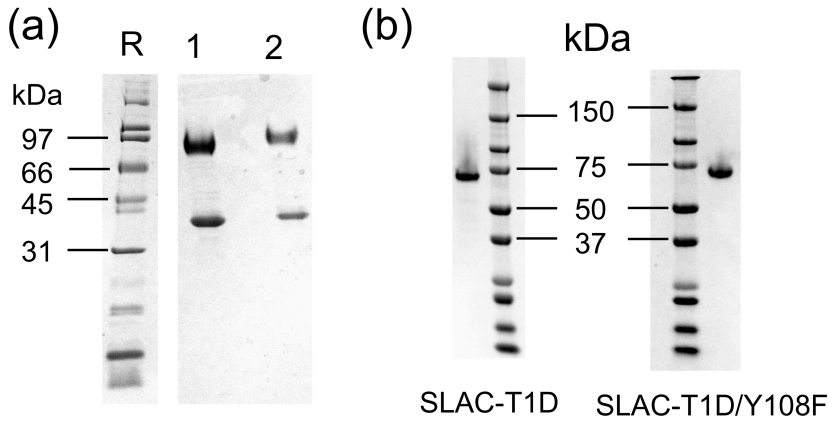


Figure S2.1. *(a) 12.5% SDS PAGE of purified SLAC-T1D. Lane R is the molecular marker with molecular weights in kDa, in lane 1 and 2 are the perdeuterated and fully protonated sample respectively. The samples were heated at 95°C for 30 s before loading on the gel. The detail description is given in the main text; (b) Image of a Bis-Tris precast SDS PAGE gel (ThermoFischer scientific) of purified SLAC-T1D and SLAC-T1D/Y108F without heating.*

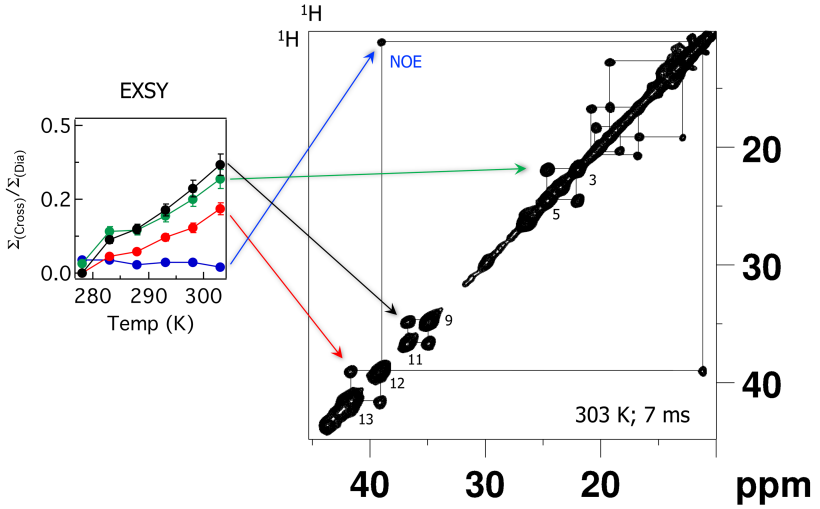


Figure S2.2. *^{1}H-^{1}H EXSY spectra acquired at 303 K and a mixing time of 7 ms. The plot on the left shows the temperature dependence of the integral volume of cross peaks normalized to the integral volume of the diagonal peaks for the resonance pair 3-5 (green), 9-11 (black), 13-12 (red) and 12- resonance at 11 ppm (blue) with the error bars that are the standard error of the mean derived from the duplicate experiments.*

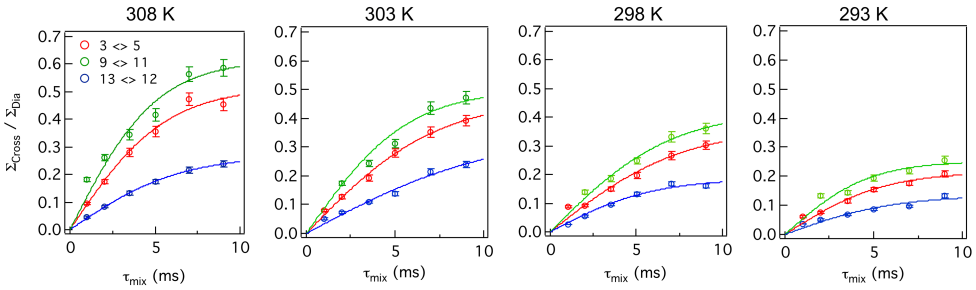


Figure S2.3. *Fits of the intensity profile of normalized cross peak integrals from the resonance pairs of 3-5, 9-11 and 13-12 at different temperatures to equations S2.1 to S2.4. The error bars represent the standard error of the mean derived from the duplicate experiments.*

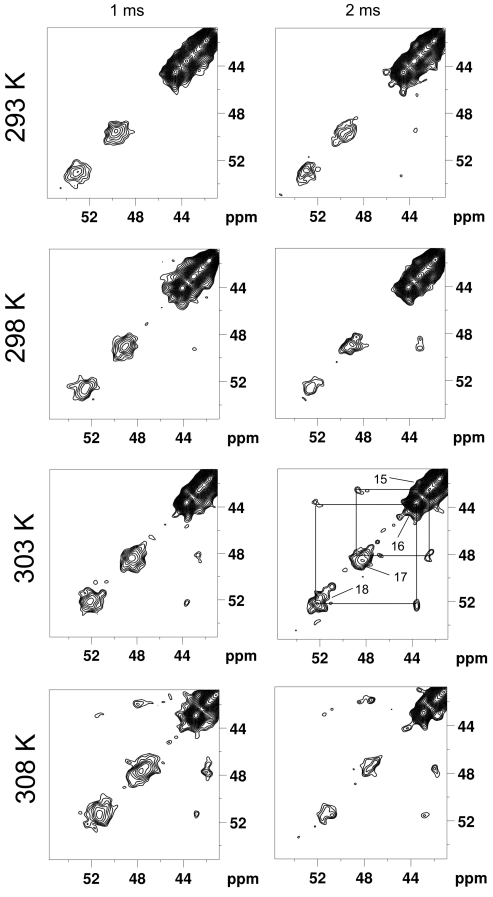
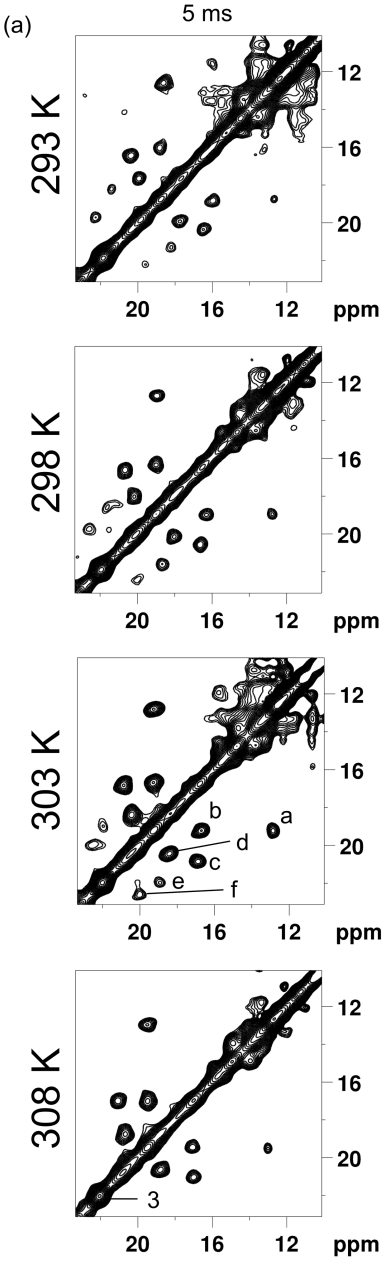


Figure S2.4. *^{1}H-^{1}H EXSY from resonances 17 and 18 at different temperatures and with mixing times of 1 ms and 2 ms. Cross-peaks are marked at 303 K with 2 ms mixing time between the resonance pairs 17-15 and 18-16.*



(b)

Cross peak	ppm (293 K)
	Dia 1 to Dia 2
a	18.62 to 12.65
b	18.78 to 16.00
c	20.34 to 16.40
d	19.89 to 17.66
e	21.35 to 18.21
f	22.20 to 19.62

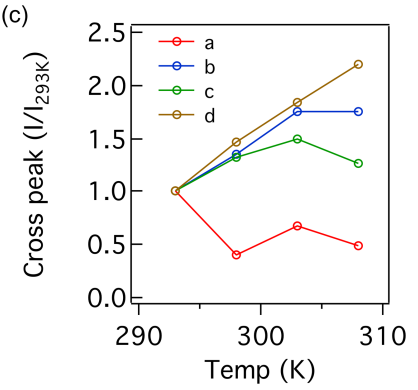


Figure S2.5. *(a) ^{1}H-^{1}H EXSY spectra at different temperatures, showing the region between 10 and 22 ppm. The cross peaks are labelled in the spectrum recorded at 303 K, (b) Chemical shifts of the diagonal peaks having cross peaks and (c) Temperature dependence of the cross-peak integrals of a, b, c and d.*

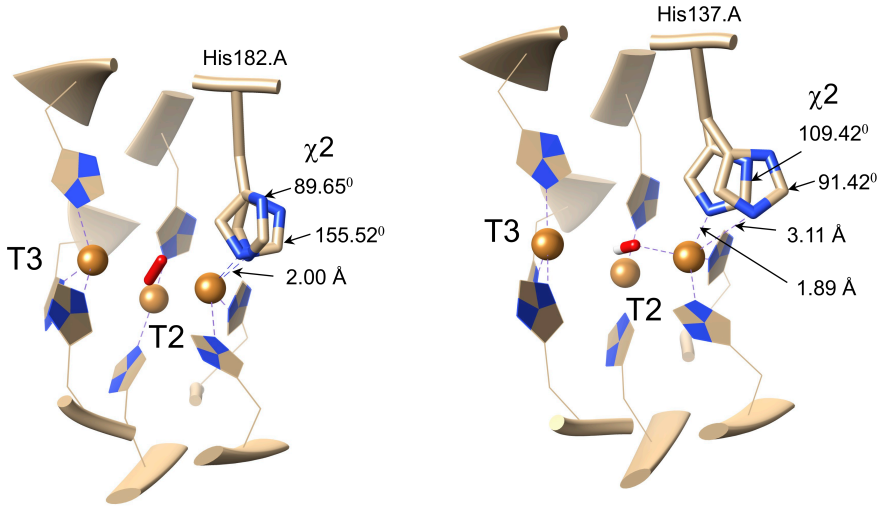
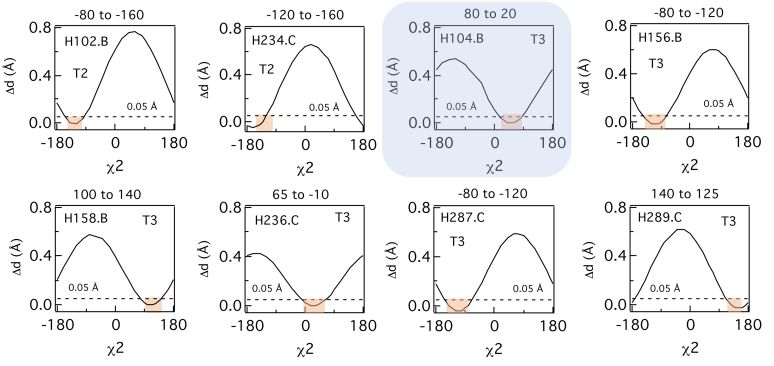


Figure S2.6. *Conformational freedom in TNC histidine ligands. (a) TNC of laccase from Campylobacter jejuni showing two conformations of His182.A (PDB 3zx1, resolution 1.95 Å) (26) due to a change in the χ2 dihedral angle. Both conformers coordinate the copper. (b) TNC of laccase from Thermus thermophilus HB27 (PDB 2xu9 resolution 1.50 Å) (27) showing two conformations for His137A. The χ2 dihedral changes by ~ 20° but the χ1 dihedral change by ~ 140° resulting in the loss of coordination of the copper.*



Residue	Original χ2 dihedral angle
His102.B	-114.02
His234.C	-131.47
His104.B	58.70
H156.B	-88.49
H158.B	114.62
H236.C	32.04
H287.C	-82.25
H289.C	127.01

Figure S2.7. *Difference of T3Cu – Nε2 distance from the original crystallographic distance as a function of the χ2 dihedral angle for His ligands (number.chain-ID) from PDB 3cg8 (17) of SLAC. Assuming that the coordination would be lost if the distance were to increase more than 0.05 Å and applying the condition that there are no clashes with the surrounding atoms and the hydrogen bond with the His Nδ1 is maintained, the structure would allow for the χ2 angle to vary between the values given above the graphs and highlighted in the graphs. Nδ1 of His104.B has no hydrogen bond (highlighted graph). The table shows the χ2 angle observed in the structure.*

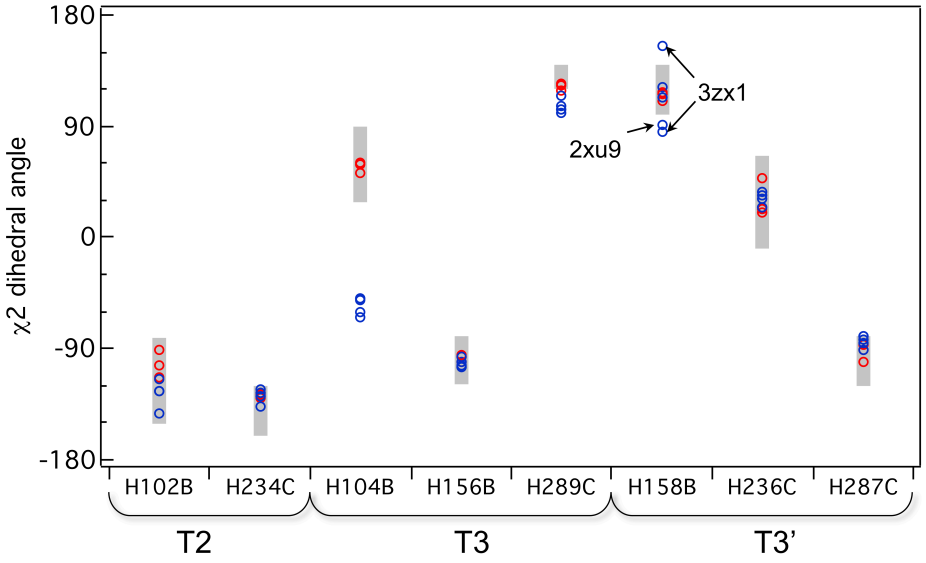


Figure S2.8. *Distribution of the χ2 dihedral angle of the His ligands at the TNC from structures of different prokaryotic laccases. The number and chain ID (residue.number.chain) scheme is adopted from PDB 3cg8, the structure of SLAC from S. coelicolor. Blue and red data points are from the bacterial 3-domain and 2-domain laccases, respectively. The grey bars represent the ranges shown in Figure S2.7. The crystal structures used are 3cg8,(17) 5lhl,(34) 1gsk,(35) 2fqe,(36) 3t9w,(37) 3g5w,(38) 2xu9,(27) and 3zx1(26) for laccases from S. coelicolor, S. griseoflavus, Bacillus subtilis, E. coli, Amycolatopsis sp. ATCC 39116, Nitrosomonas europaea, Thermus thermophilus HB27 and Campylobacter jejuni Cgug11284, respectively. In 3-domain laccases (1gsk, 2fqe, 3g5w, 2xu9 and 3zx1) the Nδ1 atom of H104 coordinates the copper rather than the Nε2 atom in the case of 2-domain laccases. For 3zx1 two χ2 dihedral angles were observed for H158.*

The Python code to extract the information of the χ2 dihedral angle of the histidine ligands from a PDB file can be found in:

https://github.com/rubindg/chi2_dihedral_angle_histidine_copper_protein

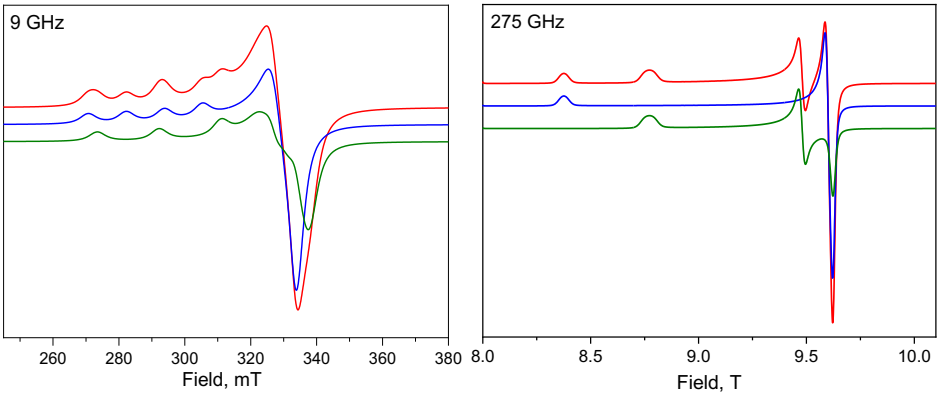


Figure S2.9. *Simulated (red line and Figure 2.3 in the main text) EPR spectra of the resting form of SLAC-T1D (as purified) at microwave frequencies of 9.5 GHz and 275 GHz. The separate contributions of major component 1 (65%) and minor component 2 (35%) to the simulated spectra are shown in blue and green, respectively. The hyperfine interactions of the copper electron spin with the nitrogen nuclei of the copper-coordinating histidine ligands are not considered for the simulations.*

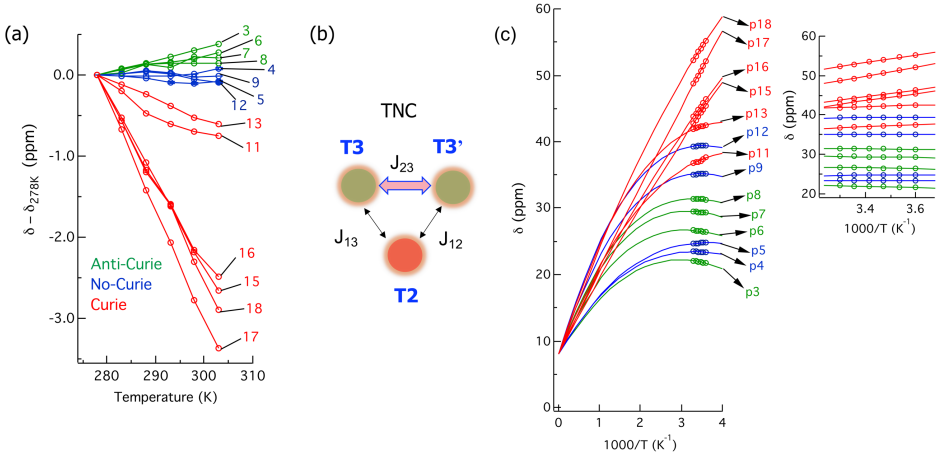


Figure S2.10*. (a) Temperature dependence of the FCS resonances marked as anti-Curie (green), Curie (red) and no-Curie (blue), (b) The tri-nuclear copper center with respective J couplings between different pairs of coppers and (c) Temperature dependence of the paramagnetically shifted resonances. Solid lines shows the simulation based on the J coupling values obtained from Machczynski et al. (2016) (19) The inset shows the zoomed area of the data points highlighting the quality of the simulation over the data points.*

Table S2.1*. Chemical shifts of the paramagnetically shifted resonances (corresponding to Figure 2.1b in the main text) at ^{1}H Larmor frequency of 600 MHz.*

Resonance	Chemical shift in ppm at 288 K
1	17.66
2	19.65
3	21.94
4	23.48
5	24.73
6	26.56
7	29.47
8	31.63
9	35.21
10	36.20
11	37.45
12	39.37
13	42.28
14	41.19
15	44.52
16	45.27
17	50.76
18	54.09

Table S2.2*. Spin-lattice relaxation rates (s^{-1})* as obtained from inversion recovery experiment and used in the fitting in equation S2.1.*

Temp (K)	Spin lattice relaxation (s^{-1})					
	3	***5***	***9***	***11***	***12***	***13***
293	169	509	144	525	180	499
298	225	457	240	464	170	492
303	180	404	241	422	407	566
308	192	486	225	463	210	477

[*] Error is estimated to be ~ ± 5% from duplicate measurements.

Table S2.3. *Residues and atoms that forms the hydrogen bond(s) (H-bond) with Nδ1 of coordinating His ligands at the TNC (obtained from PDB 3cg8). The residue number and chain ID are given. O is the backbone carbonyl oxygen or oxygen from water molecule. His ligands in red are from the T2 site.*

Ligand	Residue forming H-bond
H158.B	E163.B O H158.B O
H236.C	H_2O 676.C O
H287.C	C288.C O
H289.C	H289.C O
H156.B	D157.B O
H104.B	-
H102.B	H_2O 629.B O D113.B O
H234.C	D259.C O

Table S2.4*. Spin Hamiltonian parameters used for the simulation of the experimental EPR spectra of SLAC-T1D. A g-strain of (0.0015 0.0025 0.008) is included for both components.*

Spin Hamiltonian parameters	Major Component 1	Minor Component 2
A_x (MHz)	40	40
A_y (MHz)	50	50
A_z (MHz)	380	590
g_x	2.047	2.047
g_y	2.052	2.078
g_z	2.352	2.246

***Table S2.5**. Estimated PCS contribution to the observed chemical shift using equation 1.11 and the J coupling values of J_{12} = –120 cm^{-1}, J_{13} = –80 cm^{-1} and J_{23} = –150 cm^{-1} (Figure S2.10b).(19) The g-anisotropy for T3 site was assumed to be 0.4 (39) and for the T2 site it was calculated from Table S2.4 for major and minor components. The value of θ was 0°. The protons were modelled using add hydrogen tool in UCSF chimera to get an estimation of the distance to the copper atom using PDB 3cg8.(17, 33) Bold font represents the His coordinating the T2 copper, blue represents the His coordinating T3 site copper and black T3' copper.*

Proton (Hδ1)	PCS_T3 (ppm)	PCS_T3' (ppm)	PCS_T2_Component 1 (ppm)	PCS_T2_Component 2 (ppm)
His102	0.94	0.56	6.23	3.70
His234	0.55	0.84	5.90	3.50
His158	1.30	0.33	1.10	0.66
His236	1.58	0.32	4.50	2.72
His287	1.25	0.50	1.27	0.75
His289	0.60	1.58	1.23	0.73
His156	0.60	1.57	1.57	0.93
His104	0.37	1.62	5.56	3.30

***Table S2.6**. EPR parameters of the T2 site in g_z-region of multicopper oxidases from different organisms around pH 7. wt, T1D and T1Hg refer to wild-type, T1 copper depleted and T1 copper replaced by Hg, respectively.*

Protein	Organism	g_z	A_z (MHz)	Reference
Laccase-wt	*Trametes hirsuta*	2.260	557	(40)
Laccase-wt	*Trametes ochracea*	2.240	581	(40)
Laccase-wt	*Cerrena maxima*	2.240	581	(40)
Laccase-wt	*Coriolopsis fulvocinera*	2.230	582	(40)
Laccase-wt	*Rhus vernicefera*	2.237	599	(41)
Ceruloplasmin	Human	2.270	524	(42)
Fet3p-T1D	*Saccharomyces cerevisiae*	2.243	570	(43, 44)
Laccase-T1Hg	*Rhus vernicefera*	2.246	587	(45)
Laccase-wt	*Pleurotus ostreatus* (POXC)	2.233	587	(46)
Laccase-wt	*Rigidoporus lignosus* (POXB)	2.241	577	(46)

2.5 References

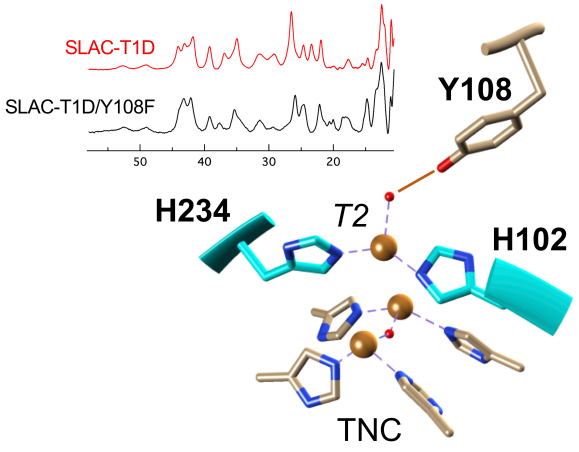
1. Mano, N., and A. de Poulpiquet. 2017. O_2 Reduction in Enzymatic Biofuel Cells. *Chem. Rev.*
2. Solomon, E.I., A.J. Augustine, and J. Yoon. 2008. O_2 Reduction to H_2O by the multicopper oxidases. *Dalton Trans.* 3921–3932.
3. Heppner, D.E., C.H. Kjaergaard, and E.I. Solomon. 2014. Mechanism of the Reduction of the Native Intermediate in the Multicopper Oxidases: Insights into Rapid Intramolecular Electron Transfer in Turnover. *J. Am. Chem. Soc.* 136:17788–17801.
4. Lee, S.-K., S.D. George, W.E. Antholine, B. Hedman, K.O. Hodgson, and E.I. Solomon. 2002. Nature of the Intermediate Formed in the Reduction of O_2 to H_2O at the Trinuclear Copper Cluster Active Site in Native Laccase. *J. Am. Chem. Soc.* 124:6180–6193.
5. Palmer, A.E., S.K. Lee, and E.I. Solomon. 2001. Decay of the Peroxide Intermediate in Laccase: Reductive Cleavage of the O−O Bond. *J. Am. Chem. Soc.* 123:6591–6599.
6. Machczynski, M.C., E. Vijgenboom, B. Samyn, and G.W. Canters. 2004. Characterization of SLAC: A small laccase from *Streptomyces coelicolor* with unprecedented activity. *Protein Science.* 13:2388–2397.
7. Tepper, A.W.J.W., S. Milikisyants, S. Sottini, E. Vijgenboom, E.J.J. Groenen, and G.W. Canters. 2009. Identification of a Radical Intermediate in the Enzymatic Reduction of Oxygen by a Small Laccase. *Journal of the American Chemical Society*. 131:11680–11682.
8. Gupta, A., I. Nederlof, S. Sottini, A.W.J.W. Tepper, E.J.J. Groenen, E.A.J. Thomassen, and G.W. Canters. 2012. Involvement of Tyr108 in the Enzyme Mechanism of the Small Laccase from *Streptomyces coelicolor*. *Journal of the American Chemical Society*. 134:18213–18216.
9. Wang, J., K. Wang, F.-B. Wang, and X.-H. Xia. 2014. Bioinspired copper catalyst effective for both reduction and evolution of oxygen. *Nat Commun*. 5:5285.
10. van Dijk, B., J.P. Hofmann, and D.G.H. Hetterscheid. 2018. Pinpointing the active species of the Cu(DAT) catalyzed oxygen reduction reaction. *Phys. Chem. Chem. Phys.* 20:19625–19634.
11. Langerman, M., and D.G.H. Hetterscheid. 2019. Fast Oxygen Reduction Catalyzed by a Copper(II) Tris(2-pyridylmethyl)amine Complex through a Stepwise Mechanism. *Angewandte Chemie*. 131:13108–13112.
12. Thorum, M.S., J. Yadav, and A.A. Gewirth. 2009. Oxygen Reduction Activity of a Copper Complex of 3,5-Diamino-1,2,4-triazole Supported on Carbon Black. *Angewandte Chemie International Edition*. 48:165–167.
13. Brookes, J.C. 2017. Quantum effects in biology: golden rule in enzymes, olfaction, photosynthesis and magnetodetection. *Proceedings of the Royal Society A: Mathematical, Physical and Engineering Science*. 473:20160822.
14. Dorner, R., J. Goold, L. Heaney, T. Farrow, and V. Vedral. 2012. Effects of quantum coherence in metalloprotein electron transfer. *Phys. Rev. E*. 86:031922.
15. Fröhlich, H. 1968. Long-range coherence and energy storage in biological systems. *Int. J. Quantum Chem*. 2:641–649.
16. Lloyd, S. 2011. Quantum coherence in biological systems. *J. Phys.: Conf. Ser.* 302:012037.
17. Skálová, T., J. Dohnálek, L.H. Østergaard, P.R. Østergaard, P. Kolenko, J. Dušková, A. Štěpánková, and J. Hašek. 2009. The Structure of the Small Laccase from *Streptomyces coelicolor* Reveals a Link between Laccases and Nitrite Reductases. *Journal of Molecular Biology*. 385:1165–1178.
18. Bertini, I., C. Luchinat, G. Parigi, and R. Pierattelli. 2005. NMR Spectroscopy of Paramagnetic Metalloproteins. *ChemBioChem*. 6:1536–1549.
19. Machczynski, M.C., and J.T. Babicz. 2016. Correlating the structures and activities of the resting oxidized and native intermediate states of a small laccase by paramagnetic NMR. *Journal of Inorganic Biochemistry*. 159:62–69.
20. Bertini, I., C. Luchinat, G. Parigi, and E. Ravera. 2017. NMR of paramagnetic molecules: applications to metallobiomolecules and models. Second edition. Amsterdam: Elsevier.
21. Bertini, I., C. Luchinat, and G. Parigi. 2002. Magnetic susceptibility in paramagnetic NMR. *Progress in Nuclear Magnetic Resonance Spectroscopy*. 40:249–273.
22. Bertini, I., C. Luchinat, G. Parigi, and R. Pierattelli. 2008. Perspectives in paramagnetic NMR of metalloproteins. *Dalton Transactions*. 0:3782–3790.

23. Jeener, J., B.H. Meier, P. Bachmann, and R.R. Ernst. 1979. Investigation of exchange processes by two-dimensional NMR spectroscopy. *J. Chem. Phys.* 71:4546–4553.
24. Farrow, N.A., O. Zhang, J.D. Forman-Kay, and L.E. Kay. 1994. A heteronuclear correlation experiment for simultaneous determination of ^{15}N longitudinal decay and chemical exchange rates of systems in slow equilibrium. *J Biomol NMR*. 4:727–734.
25. Zaballa, M.-E., L. Ziegler, D.J. Kosman, and A.J. Vila. 2010. NMR Study of the Exchange Coupling in the Trinuclear Cluster of the Multicopper Oxidase Fet3p. *J. Am. Chem. Soc.* 132:11191–11196.
26. Silva, C.S., P. Durão, A. Fillat, P.F. Lindley, L.O. Martins, and I. Bento. 2012. Crystal structure of the multicopper oxidase from the pathogenic bacterium *Campylobacter jejuni* CGUG11284: characterization of a metallo-oxidase. *Metallomics*. 4:37–47.
27. Serrano-Posada, H., S. Centeno-Leija, S.P. Rojas-Trejo, C. Rodríguez-Almazán, V. Stojanoff, and E. Rudiño-Piñera. 2015. X-ray-induced catalytic active-site reduction of a multicopper oxidase: structural insights into the proton-relay mechanism and O_2-reduction states. *Acta Cryst D*. 71:2396–2411.
28. van Gastel, M., J.W.A. Coremans, H. Sommerdijk, M.C. van Hemert, and E.J.J. Groenen. 2002. An ab Initio Quantum-Chemical Study of the Blue-Copper Site of Azurin. *J. Am. Chem. Soc.* 124:2035–2041.
29. Hu, F., W. Luo, and M. Hong. 2010. Mechanisms of Proton Conduction and Gating in Influenza M2 Proton Channels from Solid-State NMR. *Science*. 330:505–508.
30. Hass, M.A.S., D.F. Hansen, H.E.M. Christensen, J.J. Led, and L.E. Kay. 2008. Characterization of Conformational Exchange of a Histidine Side Chain: Protonation, Rotamerization, and Tautomerization of His61 in Plastocyanin from *Anabaena variabilis*. *J. Am. Chem. Soc.* 130:8460–8470.
31. Perrin, C.L., and T.J. Dwyer. 1990. Application of two-dimensional NMR to kinetics of chemical exchange. *Chem. Rev.* 90:935–967.
32. Stoll, S., and A. Schweiger. 2006. EasySpin, a comprehensive software package for spectral simulation and analysis in EPR. *Journal of Magnetic Resonance*. 178:42–55.
33. Pettersen, E.F., T.D. Goddard, C.C. Huang, G.S. Couch, D.M. Greenblatt, E.C. Meng, and T.E. Ferrin. 2004. UCSF Chimera—A visualization system for exploratory research and analysis. *Journal of Computational Chemistry*. 25:1605–1612.
34. Gabdulkhakov, A., I. Kolyadenko, O. Kostareva, A. Mikhaylina, P. Oliveira, P. Tamagnini, A. Lisov, and S. Tishchenko. 2019. Investigations of Accessibility of T2/T3 Copper Center of Two-Domain Laccase from *Streptomyces griseoflavus* Ac-993. *International Journal of Molecular Sciences*. 20:3184.
35. Enguita, F.J., L.O. Martins, A.O. Henriques, and M.A. Carrondo. 2003. Crystal Structure of a Bacterial Endospore Coat Component a laccase with enhanced thermostability properties. *J. Biol. Chem.* 278:19416–19425.
36. Li, X., Z. Wei, M. Zhang, X. Peng, G. Yu, M. Teng, and W. Gong. 2007. Crystal structures of *E. coli* laccase CueO at different copper concentrations. *Biochemical and Biophysical Research Communications*. 354:21–26.
37. Majumdar, S., T. Lukk, J.O. Solbiati, S. Bauer, S.K. Nair, J.E. Cronan, and J.A. Gerlt. 2014. Roles of Small Laccases from Streptomyces in Lignin Degradation. *Biochemistry*. 53:4047–4058.
38. Lawton, T.J., L.A. Sayavedra-Soto, D.J. Arp, and A.C. Rosenzweig. 2009. Crystal Structure of a Two-domain Multicopper Oxidase implications for the evolution of multicopper blue proteins. *J. Biol. Chem.* 284:10174–10180.
39. Tepper, A.W.J.W., L. Bubacco, and G.W. Canters. 2006. Paramagnetic Properties of the Halide-Bound Derivatives of Oxidised Tyrosinase Investigated by ^1H NMR Spectroscopy. *Chem. Eur. J.* 12:7668–7675.
40. Shleev, S.V., O.V. Morozova, O.V. Nikitina, E.S. Gorshina, T.V. Rusinova, V.A. Serezhenkov, D.S. Burbaev, I.G. Gazaryan, and A.I. Yaropolov. 2004. Comparison of physico-chemical characteristics of four laccases from different basidiomycetes. *Biochimie*. 86:693–703.
41. Malmström, B.G., B. Reinhammar, and T. Vänngård. 1970. The state of copper in stellacyanin and laccase from the lacquer tree *Rhus vernicifera*. *Biochimica et Biophysica Acta (BBA) - Bioenergetics*. 205:48–57.

42. Dawson, J.H., D.M. Dooley, and H.B. Gray. 1978. Coordination environment and fluoride binding of type 2 copper in the blue copper oxidase ceruloplasmin. *PNAS*. 75:4078–4081.
43. Augustine, A.J., L. Quintanar, C.S. Stoj, D.J. Kosman, and E.I. Solomon. 2007. Spectroscopic and Kinetic Studies of Perturbed Trinuclear Copper Clusters: The Role of Protons in Reductive Cleavage of the O−O Bond in the Multicopper Oxidase Fet3p. *J. Am. Chem. Soc.* 129:13118–13126.
44. Palmer, A.E., L. Quintanar, S. Severance, T.-P. Wang, D.J. Kosman, and E.I. Solomon. 2002. Spectroscopic Characterization and O_2 Reactivity of the Trinuclear Cu Cluster of Mutants of the Multicopper Oxidase Fet3p. *Biochemistry*. 41:6438–6448.
45. Tamilarasan, R., and D.R. McMillin. 1989. Spectroscopic studies of the type 2 and type 3 copper centres in the mercury derivative of laccase. *Biochemical Journal*. 263:425–429.
46. Garzillo, A.M., M.C. Colao, V. Buonocore, R. Oliva, L. Falcigno, M. Saviano, A.M. Santoro, R. Zappala, R.P. Bonomo, C. Bianco, P. Giardina, G. Palmieri, and G. Sannia. 2001. Structural and Kinetic Characterization of Native Laccases from *Pleurotus ostreatus, Rigidoporus lignosus*, and *Trametes trogii*. *J Protein Chem*. 20:191–201.

Chapter 3

Towards resolving the complex paramagnetic NMR spectrum of small laccase: Assignments of resonances to residue specific nuclei



This chapter is published as:
Dasgupta, R., K.B.S.S. Gupta, H.J.M. de Groot, and M. Ubbink. 2021. Towards resolving the complex paramagnetic nuclear magnetic resonance (NMR) spectrum of small laccase: assignments of resonances to residue-specific nuclei. *Magnetic Resonance*. 2:15–23. DOI: https://doi.org/10.5194/mr-2-15-2021

Laccases efficiently reduce dioxygen to water in an active site containing a tri-nuclear copper centre (TNC). The dynamics of the protein matrix is a determining factor for the efficiency in catalysis. To probe mobility, NMR spectroscopy is highly suitable. However, several factors complicate the assignment of resonances to active site nuclei in laccases. The paramagnetic nature causes large shifts and line broadening. Furthermore, the presence of slow chemical exchange processes of the imidazole rings of copper ligands results in peak doubling. A third complicating factor is that the enzyme occurs in two states, the native intermediate (NI) and resting oxidized (RO) states, with different paramagnetic properties. The present study aims at resolving the complex paramagnetic NMR spectra of the TNC of *S. coelicolor* small laccase (SLAC). With a combination of paramagnetically tailored NMR experiments, resonances of all eight His Nδ1 and Hδ1 for the NI state are identified, as well as His Hβ protons for the RO state. With the help of second shell mutagenesis, selective resonances are tentatively assigned to the histidine ligands of the copper in the type-2 site. This study demonstrates the utility of the approaches used for the sequence specific assignment of the paramagnetic NMR spectra of ligands in the TNC that ultimately may lead to a description of the underlying motion.

3.1 Introduction

Multicopper oxidases (MCOs) oxidize a wide variety of substrates at their type 1 (T1) site and catalyse the 4-electron reduction of molecular oxygen to water at the tri-nuclear copper center (TNC). The TNC consists of a type 2 (T2) copper site and a binuclear type 3 (T3) copper site. Based on crystallographic, spectroscopic and theoretical studies, the present model of the oxygen reduction mechanism by the TNC is shown in Figure 1.3.(1–5) The two-domain small laccase from *S. coelicolor* (SLAC) has been reported to involve the formation of a tyrosine radical (Tyr108$^{\bullet}$) near the T2 site during the peroxide intermediate (PI) to native intermediate (NI) conversion.(1, 4) This radical has been suggested to act as protection against the reactive oxygen species (ROS) that can be formed due to the long-lived peroxide intermediate state.(1, 6) The tyrosyl radical was shown to be reduced by the protein environment via tryptophan and tyrosine residues around the T2 site.(6) A similar role was proposed for Tyr107 in human ceruloplasmin (hCp). hCp is a ferroxidase critical for iron homeostasis. It oxidizes Fe^{2+} to Fe^{3+} for iron transport. In serum the hCp is active under low Fe^{2+} and high O_2 concentration. This leads to a partially reduced intermediate that can form ROS. The tyrosine radical protects the protein from this partially reduced state.(7)

Although the reaction mechanism of laccase is well characterized, information about motions around the TNC is limited. The oxygen reduction process

is a multi-step reaction involving transfer of four electron and protons with oxidation and reduction of the copper ions (Figure 1.3). Each step is associated with its respective activation energy barrier and the motions of the protein, especially within the active site, may be useful in reduction or crossing of these barriers. Such motions have been reported for many proteins, for example dihydrofolate reductase, adenylate kinase and cytochrome P450.(8–11) Characterisation of the motion at the TNC of laccase can help in designing a functional framework for understanding the natural process and the *de novo* design of efficient bioinspired catalysts. Three or more independent chemical exchange processes, tentatively assigned to the coordinating histidine residues at the TNC were reported using paramagnetic NMR spectroscopy on the T1 copper depleted variant of SLAC, SLAC-T1D (Chapter 2).(12) However, further characterisation of motions requires assignments of the NMR resonances very near to the TNC. The paramagnetic nature of the copper ions causes broadening and chemical shifts outside of the diamagnetic envelope, making it impossible to employ standard multidimensional protein assignment experiments. Assignment is further complicated by two reasons. SLAC spectra are a mixture of the RO and NI states. (13) In the RO state the T2 Cu^{2+} is isolated, causing broadening of the signals of nearby proton spins beyond detection. The two copper ions in the T3 site are antiferromagnetically coupled, with a low-lying triplet state that is populated at room temperature, causing paramagnetically shifted (in the range of 12 - 22 ppm), detectable resonances of nearby protons. In the NI state all copper ions are coupled, resulting in a frustrated spin system, with strongly shifted (> 22 ppm), but observable resonances.(14) The second cause of complexity is that the mentioned exchange processes of the coordinating histidine residues result in peak doublings, because the exchange rates are in the slow exchange regime relative to the resonance frequency differences. In this study, we aimed to resolve further this complicated paramagnetic NMR spectrum. Using differently labelled samples and tailored HMQC experiments, the presence of all eight-histidine ligand Nδ1 and Hδ1 resonance in the NI state could be established. The first studies of the RO state identified resonances as histidine Hδ1 or Hβ protons and a second coordination shell mutant allowed for the first residue and sequence specific assignment. The study demonstrates the utility of the approaches used for the sequence specific assignments of the ligands in the TNC that may ultimately lead to a description of the underlying motions.

3.2 Results and discussions

Identification of nitrogen attached protons in the NI state

The Fermi contact shifted resonances for SLAC-T1D were reported before and here we use the numbering used in our previous study (Chapter 2).(12, 13) Eighteen resonances were found between 15 and 60 ppm.(12) Resonances 1 and 2 were assigned to a region that is attributed to the RO state, therefore we followed the numbering from 3 to 18 in the present work (Figure 3.1a and 2.1a). Resonance 10 is from a proton bound to carbon and is overlapping with resonances 9 and 11 at temperatures > 293 K (12) (Figure 3.1a). The ^{1}H resonances that exhibited exchange processes (3-5, 9-11 and 13-12, see also Figure 2.2 and S2.2) were assigned to Hδ1 nuclei from histidine coordinated to the copper ion (Chapter 2). To verify this assignment, a paramagnetically tailored ^{15}N – ^{1}H HMQC experiment (Figure 1.5c, the detail of the experiment is given in the caption of Figure S3.2) was performed on a SLAC-T1D sample that was specifically labelled with ^{15}N histidine in a perdeuterated, back-exchanged environment. The evolution period was shortened to 500 μs, balancing the time required for formation of antiphase magnetisation and paramagnetic relaxation, to optimize S/N ratio for most of the resonances.(15, 16) A total of 10 resonances (3, 4, 5, 6, 9, 11, 12, 13, 14/15, 16, see Figure 3.1b) were observed at ^{1}H chemical shifts of > 21 ppm. Resonance 7, 8 and 10 were not observed in this experiment, which is consistent with their assignment to carbon attached protons (Chapter 2).(17) These results show unequivocally that the HMQC resonances derive from the Hδ1 protons of the coordinating histidine residues of the TNC, because only these protons are nitrogen attached and close enough to experience such large paramagnetic shifts. The three pairs or resonances representing exchange processes (3-5, 9-11 and 13-12) are thus also from Hδ1 proton, in line with the suggested histidine ring motion being the involved chemical exchange process. The HMQC spectrum of uniformly ^{15}N labelled SLAC-T1D is similar to the ^{15}N-His specifically labelled SLAC-T1D sample in a perdeuterated back-exchanged environment (data not shown for the ^{1}H resonances > 21 ppm but shown for the region 12 to 21 ppm, see Figure 3.2b).

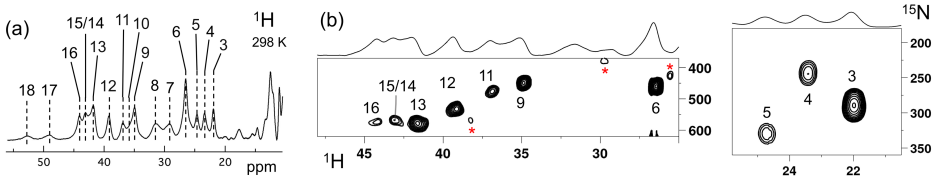


***Figure 3.1**. SLAC-T1D NMR spectra at 298 K. (a) 1D ^{1}H WEFT spectrum of SLAC-T1D and (b) ^{15}N-^{1}H HMQC spectra of ^{15}N-His perdeuterated SLAC-T1D in a back-exchanged environment. The numbering is adopted from (17). Noise peaks in the spectrum are marked with a red asterisk. The 1D ^{1}H WEFT spectrum is shown above the HMQC spectrum.*

The relative intensities of signals in the range 60-22 ppm with those of the region 21-12 ppm shows that SLAC-T1D is predominantly in the NI state (Figure 3.1 and 3.2). In the NI state, the T2 and the T3 sites are coupled thereby increasing the electronic relaxation rates of the unpaired electron spin S of the T2 site. This results in the reduction of the paramagnetic relaxation rates of the neighbouring nuclear spins. (18, 19) Therefore, it is expected that all eight ligand histidine residues are observable. In the ^{15}N–^{1}H HMQC ten resonances are seen, among which three undergo chemical exchange resulting in the observation of seven Nδ1-Hδ1 group. Resonance 17 and 18 have exchange cross-peaks with resonance 15/14 and 16, respectively at high temperatures (303 K and 308 K) and a short mixing time in an EXSY/NOESY experiment (1 and 2 ms) (Chapter 2, Figure S2.4).(17) At temperatures of 298 K and higher, resonances 14 and 15 overlap (Figure 3.1a).(17) Resonance 16 and 18 thus form a fourth exchange pair and the seventh histidine Nδ1-Hδ1 group. The eighth histidine Nδ1-Hδ1 group can be attributed to the exchange pair of resonance 17 with either 14 or 15.(17) Due to the overlapping of resonance 14 and 15 at 298 K, they are not observed distinctly in ^{15}N–^{1}H HMQC spectra (Figure 3.1b). In conclusion, all the eight Hδ1 from the coordinating histidine ligands of the TNC in SLAC-T1D for the NI state are identified in the spectral region > 21 ppm and five of them show peak doubling due to slow exchange.

Analysis of the RO state

Machczynski *et al*. (2016) reported that the signals in the spectral region between 12 to 21 ppm derive from the RO state, whereas the resonances > 21 ppm are attributed to the NI state.(13) In the RO state, the T2 copper is decoupled from the T3 site, resulting in a decrease of its electronic relaxation rate.(18) This effect broadens the resonances of nearby proton spins beyond detection for the T2 site ligands. In the RO state, the T3 copper ions are antiferromagnetically coupled and thus diamagnetic at low temperature.(18) At ambient temperature, the low-lying state with $S = 1$ is populated, resulting in paramagnetic shifts of the ligand protons.(18) The strong coupling via a hydroxyl group of the electron spins causes fast electronic relaxation and thus observable nuclear resonances for T3 ligands. T3 site ligands usually exhibit an anti-Curie behaviour, i.e. the chemical shift increases with an increase in temperature.(19–21)

All the resonances in the 12 to 22 ppm region of SLAC-T1D in an ^{1}H-^{1}H EXSY/NOESY spectrum display anti-Curie behaviour, suggesting that indeed they

derive from histidine protons of the T3 site (Figure 3.2). Comparing the ^{15}N–^{1}H HMQC and the ^{1}H-^{1}H EXSY/NOESY of the ^{15}N uniformly labelled sample in this region, resonances a1, a2, b2, c1, c2, d2, x1, x2, y, z and w are nitrogen linked protons (Figure 3.2). The RO state is the minor state in SLAC-T1D, so the S/N ratio for the HMQC resonances is low. For comparison, resonance 3, which belongs to the NI region of the spectrum (Figure 3.2b) is shown as well. ^{1}H resonances e1 and e2 could not be assigned to either carbon or nitrogen linked protons due to their low S/N ratio.

Using a two-metal center model to calculate the singlet-triplet energy gap ($2J$) from the temperature dependence of the chemical shifts (equation 1.5), a $2J$ value of -600 +/- 20 cm^{-1} was obtained, within the range of the previous reported values (-550 to -620 cm^{-1}) for the RO state of laccase (Figure 3.2c) (3, 13, 22). It was assumed that resonances a1, a2, b2, c1, c2, d2 (only isolated resonances were selected) are the Fermi contact shifted resonances of the Hδ1 of the coordinating histidine residues at the T3 site in the RO state (Figure 3.2d), as supported by their presence in the HMQC spectrum (Figure 3.2b). The diamagnetic chemical shift for these resonances was set to 9.5 ppm (BMRB average for histidine ring Hδ1).(14) To establish the diamagnetic chemical shifts of resonances b1 and d1, which are not nitrogen attached, the $2J$ coupling strength was then fixed to -600 cm^{-1} and the diamagnetic chemical shift was fitted and found to be 3.0 +/- 0.5 ppm. This value strongly suggests that these resonances are from the eight protons of coordinating histidine ligands (BMRB average for histidine Hβ is 3.1 ppm).

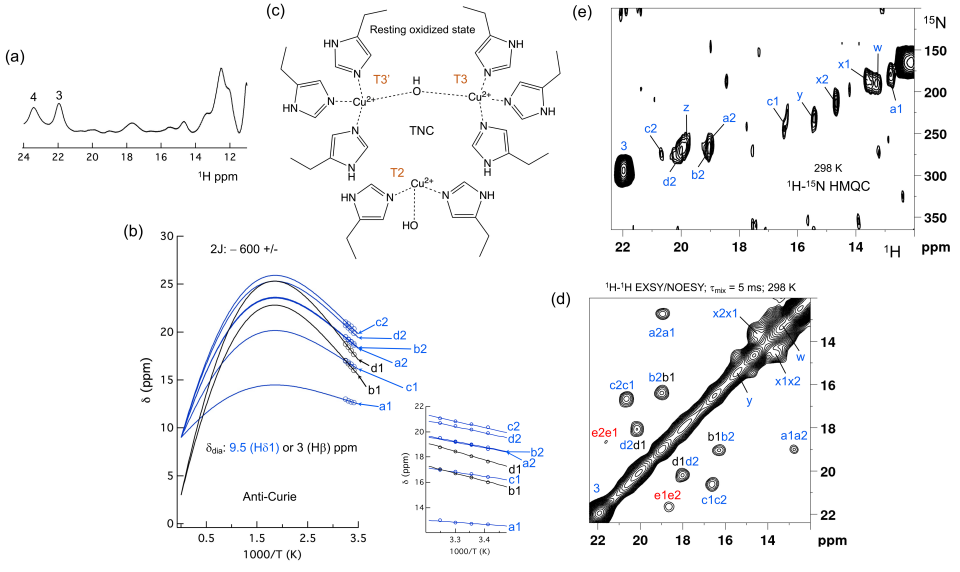


***Figure 3.2**. The spectral region of the RO state. (a) 1D ^{1}H spectra of the RO region from panel a of Figure 1. Resonances 3 and 4 of the NI spectral region are shown for comparison; (b) Temperature dependence of the chemical shift for the resonances a1, a2, b1, b2, c1, c2, d1 and d2, fitted to the two-metal center model (equation 1.5). The inset shows the experimental region of the fit. The corresponding hyperfine coupling constants are given in Table S3.5 of the supporting information; (c) Schematic representation of the RO state of the TNC. The T3 and T2 copper ions are marked. (d) ^{1}H-^{1}H EXSY/NOESY spectra of SLAC-T1D for the region between 12 to 22 ppm; (e) ^{15}N-^{1}H HMQC spectra of the ^{15}N uniformly labelled SLAC-T1D (12 to 22 ppm in the ^{1}H dimension). The resonances marked in blue are for the nitrogen attached protons while resonances in black are for carbon attached protons. Resonances in red in panel d could not be assigned to either nitrogen linked or carbon linked protons due to a low S/N ratio.*

Since the temperature dependence of the cross peak intensities as measured by their peak volume did not show a conclusive increasing trend with increase of temperature, we assumed them to be NOE rather than EXSY derived cross-peaks.(17) Therefore, the cross peaks of resonances b1-b2 and d1-d2 can be attributed to a NOE between the Hδ1 and Hβ proton of a histidine ligand. The cross-peaks between c1-c2 and a1-a2 appear to be NOE signals from nitrogen attached protons (Figure 3.2). The Hδ1 protons of the different histidine residues are not near, so it remains unclear from which spins these peaks derive. For the resonances x1, x2, y, z and w (Figure 3.2a) the analysis of the temperature dependence of the chemical shift was not possible due to the overlap.

Second shell mutagenesis to assist assignments

To aid in the assignment of the paramagnetic spectrum, mutagenesis could be employed. However, mutation of histidine ligands is expected to result in loss of copper or at least in a severe redistribution of unpaired electron density, changing the chemical shifts of all paramagnetically shifted protons. In contrast, mutations in the second coordination sphere, of residues that interact with the coordinating ligands, may have moderate effects on the electron spin density distribution. One such mutant, Y108F, has been reported before.(1) Tyr108 interacts with the TNC in two ways, with the T2 site through the water/hydroxide ligand and with the T3 ligand His104 through the hydrogen bonding network involving Asp259 (Figure S3.3a). Asp259 is conserved in all laccases, whereas Tyr108 is conserved in the two-domain laccases (Figure S3.3b). Asp259 has been reported to play a role in modulating the proton relay during the oxygen reduction reaction (23) and it may also stabilize the Tyr108-TNC interaction.

The 1D ^{1}H WEFT (24, 25) spectrum of SLAC-T1D/Y108F is similar to that of SLAC-T1D, suggesting that the variant SLAC is also predominantly in the NI state (Figure 3.2a). Some changes in the chemical shift are present. Due to the Y108F

mutation many of the ^{1}H resonances > 22 ppm are downfield shifted. Resonance 6 and 16 are upfield shifted and resonance 7, 8, 17 and 18 show no chemical shift change compared to SLAC-T1D (Figure 3.3 and Table S3.2). Also, a new resonance α is observed. The HMQC spectrum in the region > 22 ppm of the ^{1}H is very similar to that of SLAC-T1D, in agreement with the ^{1}H WEFT spectrum (Figure 3.3). Most of the ^{15}N resonances (3, 4, 5, 9, 11, 12 and 15) are downfield shifted except resonances 6, 13 and 16, which are upfield shifted (Figure 3.3 and Table S3.2). The three independent chemical exchange processes that were reported for the TNC of SLAC-T1D involving resonance pairs of 3 – 5, 9 – 11 and 13 – 12 (Chapter 2, Figure 2.2) are conserved and the rates are not affected by the Y108F mutation (Table S3.1, Figure 3.3b and Figure S3.1c), suggesting that the phenolic –OH group of Y108 is not involved in the chemical exchange process.(17) The chemical shift changes show that the two states represented by 3 – 5 and 9 – 11, respectively are affected similarly by the Y108F mutation (Figure 3.3d). In contrast, the two states represented by the resonance pair 13 – 12 are affected differently, because the nitrogen chemical shift is downfield shifted for resonance 12 and to upfield shifted for resonance 13 (Figure 3.3d).

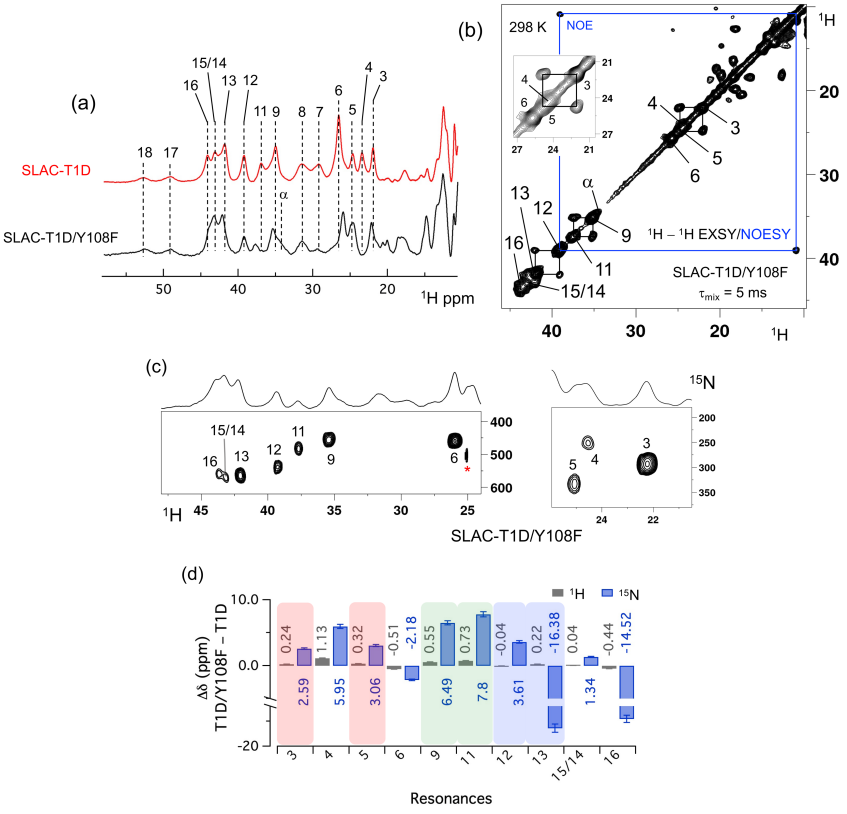


***Figure 3.3**. Spectra of SLAC-T1D/Y108F. (a) Comparison between 1D ^{1}H WEFT spectrum of SLAC-T1D (red) and SLAC-T1D/Y108F (black). The numbering is shown for SLAC-T1D and is adopted from (17); (b) ^{1}H-^{1}H EXSY/NOESY of SLAC-T1D/Y108F at 298 K with mixing time of 5 ms. NOE cross-peaks are connected with a blue rectangle. The remaining cross-peaks are exchange peaks. This distinction is based on the temperature dependent profile of the integral volume of the cross peaks as explained in (17). The inset shows that the exchange cross peaks are between 3 and 5. Resonance 4 is partly overlapping with 5; (c) ^{15}N-^{1}H HMQC spectra of ^{15}N uniformly labelled SLAC-T1D/Y108F; (d) The chemical shift changes ($\Delta\delta$) between SLAC-T1D/Y108F and SLAC-T1D for the ^{1}H (black) and ^{15}N (blue). The error bars represent the standard deviation in the determination of the chemical shift. The three pairs of resonances displaying chemical exchange are highlighted by equal background colours. Positive (negative) values represent shift to the downfield (upfield) ppm for SLAC-T1D/Y108F.*

It is proposed that resonances 13 and 16, which are most affected by the Y108F mutation (Figure 3.3d), are from the histidine ligands of the T2 copper. Due to the proximity of the T2 copper and strong hydrogen bond with a water or hydroxide ligand, the electron spin density can be expected to be delocalized to the tyrosine ring. The loss of the hydrogen bond between the phenolic -OH group of Tyr108 and the water/hydroxide ligand of the T2 copper can result in redistribution of the electron spin density on the coordinating histidine ligands. Figure 3.3d shows that the Nδ1 of the resonances 13 and 16 have the highest chemical shift perturbation of ~ –16 and –14 ppm respectively. Interestingly, resonance 13 is in an exchange process with resonance 12 (Figure 3.3b) (17) and for the latter resonance the Nδ1 exhibits a downfield shift due to the Y108F mutation. In the crystal structure 3cg8 (resolution 2.63 Å), the Nδ1 of His102 from the T2 site can have two hydrogen bonding partners, carbonyl oxygen of Asp113 and a water molecule (Figure 3.4a). Modelling the protons and changing the $\chi 2$ dihedral angle of His102 to –152° and –94°, hydrogen bonds can be formed between Hδ1 — Asp113 CO and Hδ1 — H_2O respectively. The $\chi 2$ dihedral change does not break the coordination of His102 Nε2 to the copper (Figure 3.4b and 3.4c) and is within the allowed range (–90° to –170°) (17). This shows that there can be a conformational exchange of His102 between two states with a hydrogen bond between Hδ1 and either Asp113 CO or the nearby H_2O molecule. The second shell mutation of Y108F suggests that the exchanging resonances 13 and 12 are from a Hδ1 nucleus of one of the two T2 copper histidine ligands. Thus, it is proposed that resonance 13 and 12 are from His102 Hδ1 for which the ring exchanges between the two states shown in panels Figure 3.4b and 3.4c. Consequently, resonance 16 can be tentatively assigned to the other T2 copper ligand, His234, being also strongly affected by the Y108F mutation. It does not exhibit chemical exchange at temperatures ≤ 298 K, in agreement with having a single, hydrogen bond with Asp259 CO (Figure 3.4a).

At higher temperatures (≥ 303 K) however, exchange with resonance 18 is observed. Whereas the 12/13 pair of resonances shows a difference of less than 3 ppm (17) and similar linewidth for both signals, the 16/18 pair shows almost 9 ppm difference in chemical shift and resonance 18 is much broader, indicating a more drastic change in spin density on the proton. In combination with the observation that there are no other hydrogen bond acceptors in the proximity, this suggests that resonance 18 represents the His234 Hδ1 in a state in which the hydrogen bond to Asp259 is broken. In such a state the proton would be prone to exchange with bulk water protons but the TNC is very buried, preventing rapid exchange. Similar situations as for His102 are observed for other histidine ligands in the TNC (Table S3.4). in the crystal structure of SLAC from *S. griseoflavus*, (PDB entry 6s0o resolution 1.8 Å) (26) Nδ1 of His237 can form a hydrogen bond with Asp114 Oδ1 or water O540, depending on rotation around $\chi 2$ (Figure S3.5). In the crystal structure of SLAC from *S. coelicolor* (PDB entry: 3cg8, resolution 2.68 Å) the equivalent Asp113 Oδ1 is moved away from the Nδ1 and therefore could not form a hydrogen bond (Figure S3.5a). Such exchange processes may well represent the resonances pair 3-5 and 9-11. Second-shell mutations around the respective histidine residues can help to confirm this hypothesis.

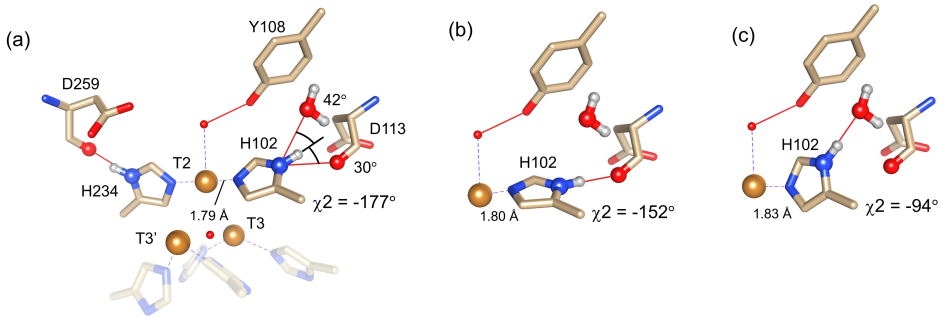


Figure 3.4*. Alternative hydrogen bond acceptors for His102. (a) T2 site histidine ligands showing the hydrogen bonds for the Nδ1-Hδ1 group. Protons were modelled using the algorithm as implemented in UCSF Chimera (27). His104 and H236 from the T3' and T3 sites, respectively, are omitted for clarity. Hydrogen bonds are shown as red lines. The $\chi 2$ dihedral angle and distance between His102 Nε2 and the T2 copper are indicated. Also, the values for the angles [Asp113 CO – His102 Nδ1 – His102 Hδ1] and [water O628 – His102 Nδ1 – His102 Hδ1] are indicated. Ring rotation brings the Hδ1 in optimal position for hydrogen bond formation with either the Asp113 CO (b) or the water (c). The new $\chi 2$ dihedral angles and the corresponding His102 Nε2 — T2 copper distances are indicated.*

The temperature dependence of Hδ1 resonance is also affected by the Y108F mutation (Figure 3.5). While the resonances that show clear Curie behaviour in SLAC-T1D also do so in the Y108F mutant, resonances that show anti-Curie or non-Curie behaviour tend more to Curie like behaviour, e.g. resonances 3, 6, 7 and 8. The overall

increase in the Curie-like behaviour for the Y108F mutant compared to that of SLAC-T1D, can be due to the decrease in the *J* coupling between copper ions due to a change in the geometry of the TNC (28) caused by the loss of the hydrogen bond between the Tyr108 the water/hydroxide. Slight chemical shift changes are also present for the ^{1}H resonances between 10 and 20 ppm in the spectrum of SLAC-T1D/Y108F relative to that of SLAC-T1D (Figure S3.4). The ^{1}H-^{1}H EXSY/NOESY spectrum shows six cross-peaks (a to f), caused by 12 diagonal signals (Figure S3.4). Among these, a1, b1, c1, c2, d1 and e1 are downfield shifted for the mutant, whereas a2, b2, d2 and e2 are upfield shifted (Figure S3.4b).

In summary, the Y108F mutation leads to the following tentative assignment of the resonances: 13 and 12 to His102 and 16 to His234 of the T2 site, with 13 and 12 being in chemical exchange.

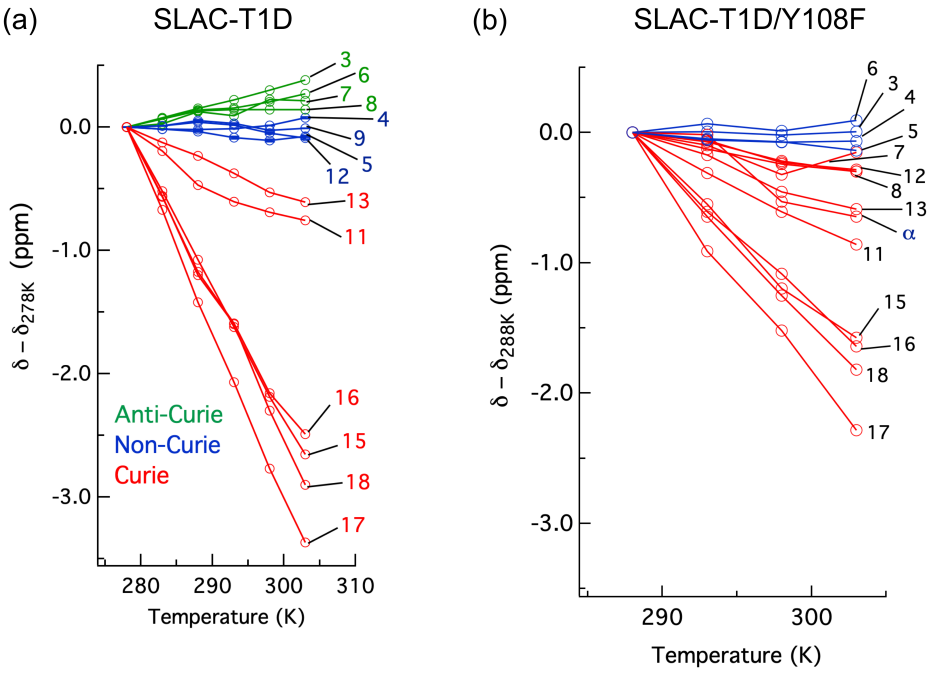


Figure 3.5. *Change in ^{1}H chemical shifts for (a) SLAC-T1D with temperature relative to 278 K and (b) SLAC-T1D/Y108F with temperature relative to 288 K. Anti-Curie, non-Curie and Curie behaviour are shown in green, blue and red, respectively.*

3.3 Conclusion

The SLAC-T1D comprises resonances from the NI and RO states, in which the RO state is the minor state.(13) Using differently labelled samples and a paramagnetically tailored ^{15}N–^{1}H HMQC experiment, all NI resonances of the Nδ1-Hδ1 groups of the eight coordinating histidine residues in the TNC were accounted for (Figure 3.1). The HMQC spectra also included the resonances that are in chemical exchange, consistent with the histidine ring motions being responsible for this phenomenon.(17) NOE cross-peaks for the RO state revealed resonances of Hβ protons of the coordinating histidine residues of the T3 site (Figure 3.2). The second shell mutation of Y108F of SLAC-T1D aided in the tentative assignment of the resonances 13 and 12 to His102 and 16 and 18 to His234 of the T2 site (Figures 3.3 and 3.4). This report shows the first sequential assignment of the paramagnetically shifted resonance to a coordinating histidine. More studies using second shell residue mutagenesis can help to provide a full sequence specific assignment, which is a prelude to a better understanding of the motions important for the catalytic mechanism

.

3.4 Supporting Information

Protein expression and purification

SLAC-T1D and SLAC-T1D/Y108F were expressed and purified as described previously. (17, 29) For ^{15}N histidine specific perdeuterated labelled sample, 50 mg/L of $^{15}N_3$-L-histidine hydrochloride monohydrate (Sigma Aldrich, USA) was added to the M9 medium consisting of ammonium chloride and D-glucose-1,2,3,4,5,6,6-d7 as nitrogen and carbon sources respectively. A volume of 200 µL of the M9 preculture was transferred to 25 mL of M9 medium prepared in 99.99% D_2O for an overnight preculture, which was used to inoculate 500 mL D_2O-M9 minimal medium. Gene expression and protein harvesting was done as for the uniform ^{15}N labelled sample. Purity was checked by SDS PAGE using a precast Bis-Tris gel (ThermoFischer scientific), as shown in Figure S3.1a. A band ~ 74 kDa is observed. Under native condition from size exclusion chromatography with multi-angle light scattering (SEC-MALS) the molecular weight of the proteins was ~ 105 kDa, in accord with the expected trimeric form.

NMR spectroscopy

Samples contained ~ 1 mM of protein in 10 mM sodium phosphate buffer pH 7.3 with 10% D_2O. Experiments were done on a Bruker AV-III HD 600 MHz NMR spectrometer equipped with a TXI cryoprobe. 1D ^1H WEFT, Inversion recovery experiments to measure the spin-lattice relaxation rate and 2D ^1H-^1H EXSY/NOESY (30) experiments were recorded as described previously (Chapter 2). (17) The mixing time dependent integral volume profiles were fitted using equations S2.1 to S2.4 (17, 31) with IGOR Pro 6.3.7 to obtain the exchange rates. The fitting was done by constraining the K_{eq} (Table S3.1) to the value of the ratio of the diagonal integral volume at mixing time of 0 ms. The spin-lattice relaxation rates used in the fitting were obtained from inversion recovery experiments.

2D ^{15}N–^1H HMQC experiments were recorded using the pulse sequence shown in Figure 1.5c and S3.2. The transfer delay d2 was optimized to 0.5 ms to enhance the paramagnetically shifted signals > 20 ppm. 48 t1 increment points were acquired with 30720 number of scans corresponding to the total acquisition time of 54 h for each experiment.

Supporting figures and tables

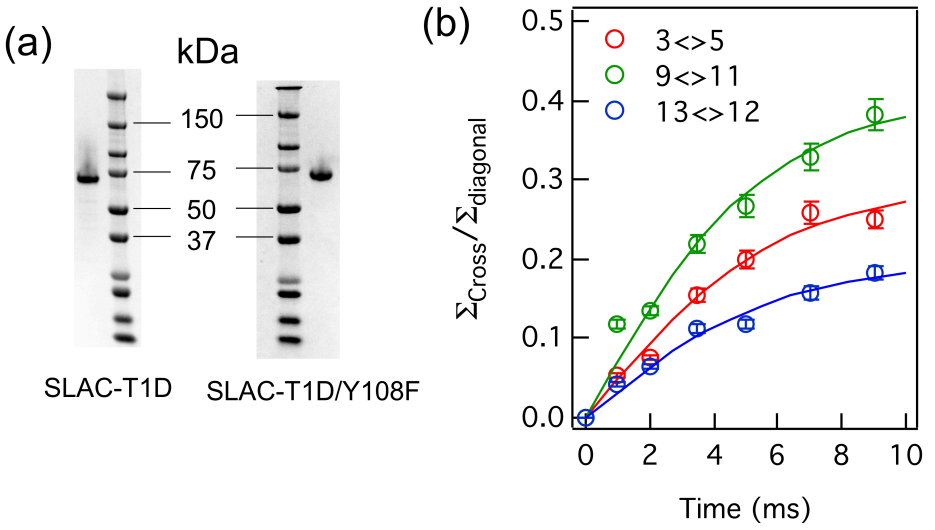


Figure S3.1*: (a) Image of a Bis-Tris precast SDS PAGE gel (ThermoFischer scientific) of purified SLAC-T1D and SLAC-T1D/Y108F; (b) Fits of the intensity profile of normalized cross peak integrals from the resonance pairs of 3-5, 9-11 and 13-12 from 2D ^{1}H-^{1}H EXSY of SLAC-T1D/Y108F to determine the exchange rates (17, 31). The error bars represent the standard error of the mean derived from the duplicate experiments.*

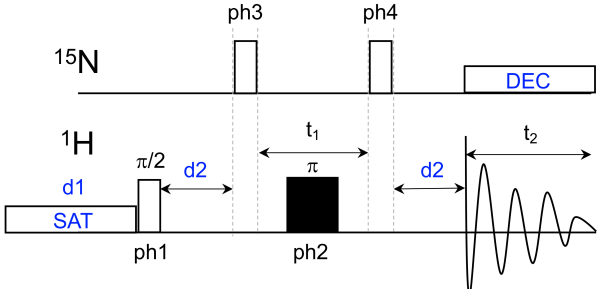


Figure S3.2. *^{15}N–^{1}H HMQC pulse sequence used in this study. Open rectangles are for 90° pulse and filled ones are for 180° pulse. The interscan delay d1 is 100 ms and SAT is the continuous wave water saturation pulse with phase of x. DEC is GARP composite pulse decoupling during the t_2 evolution. The evolution period d2 was set to 0.5 ms, corresponding to the FWHM of the paramagnetically shifted ^{1}H resonances (~ 0.8 ppm) (15, 18). The phase cycling is ph1 = x, ph2 = x, ph3 = x -x, ph4 = x x -x -x and for the receiver it was x -x x -x.*

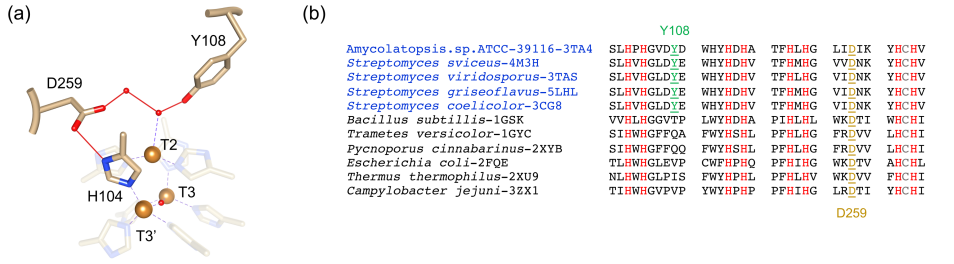


Figure S3.3. *The second coordination shell residue Tyr108. (a) Crystal structure of SLAC (PDB entry 3cg8, resolution 2.63 Å) (32), showing the hydrogen bonding network between Tyr108 and His104 via Asp259 (red lines). The hydrogen bonds were determined by the default parameter of UCSF Chimera program (27) with relaxed hydrogen bond constraints of 0.4 Å and 20.0° (Mills and Dean, 1996); (b) Sequence alignment of the two-domain (blue) and three-domain laccases (black) for which crystal structures are available (PDB code indicated). The copper coordinating residues are shown in red. Tyr108 and Asp259 (numbering from PDB 3cg8) are shown in green and gold, respectively and are underlined. The type 1 copper site ligand, cysteine, is marked in grey.*

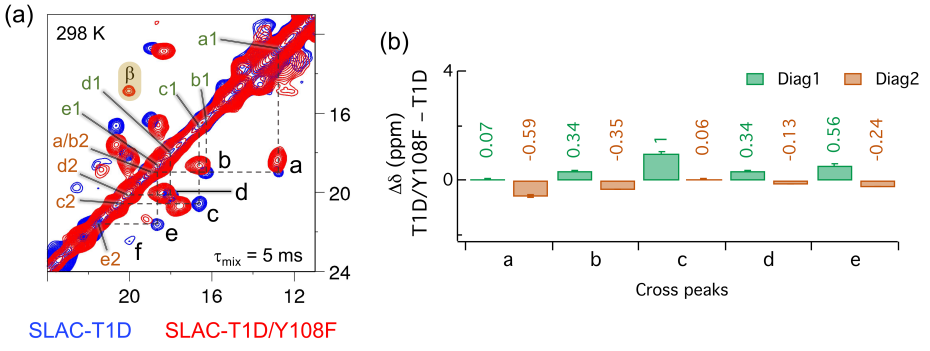


Figure S3.4. *Comparison of the RO spectral regions for SLAC-T1D and SLAC-T1D/Y108F. (a) Overlaid ^{1}H-^{1}H EXSY/NOESY spectra at 298 K with mixing time of 5 ms of SLAC-T1D (blue) and SLAC-T1D/Y108F (red) for the region between 11 and 22 ppm. Cross-peaks and diagonal peaks for SLAC-T1D are marked. Diagonal peaks are marked as a1, a2, b1, b2 etc. The new cross peak β in SLAC-T1D/Y108F is highlighted; (b) Chemical shift changes between SLAC-T1D and SLAC-T1D/Y108F. Positive values mean the diagonal peak in SLAC-T1D/Y108F is downfield shifted, while for the negative value it is upfield shifted. Diagonal peak 1 (Diag1: a1, b1, c1, d2 and e1) are shown in green while diagonal peaks 2 (Diag2: a2, b2, c2, d2, and e2) are shown in light brown. Resonance f and b are not shown since they are unique to SLAC-T1D and SLAC-T1D/Y108F respectively. More experiments are needed to identify these resonances.*

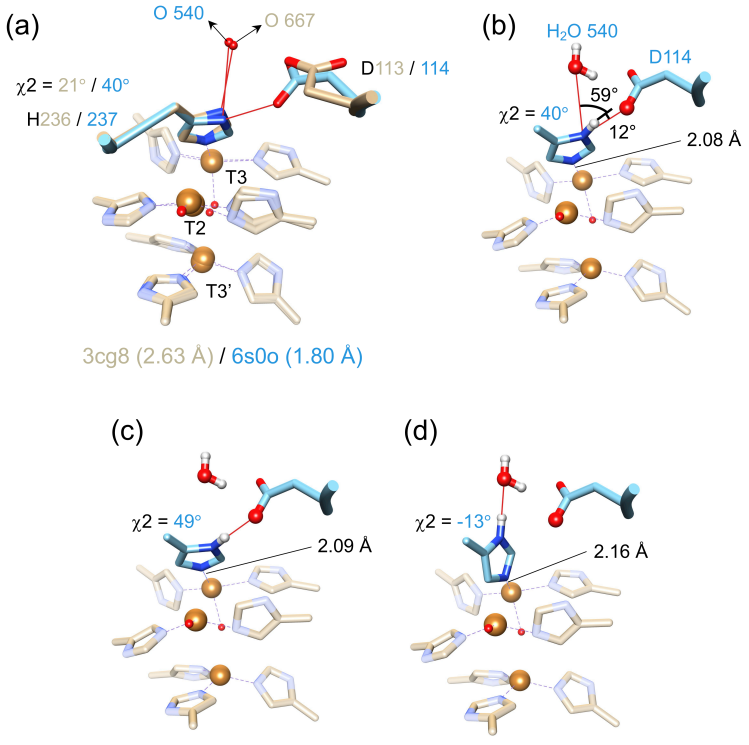


Figure S3.5. *Two H-bond acceptors for His236. (a) Overlaid TNC from crystal structure 3cg8 in gold and 6s0o in blue highlighting the hydrogen bond of the Nδ1 from the T3 histidine ligand His236/237 (26, 32). The χ2 dihedral angle for histidine 236/237 is shown for both crystal structures. Hydrogen bonds are shown as red lines; (b) Protons are modelled for the crystal structure 6s0o using the algorithm as implemented in UCSF Chimera (26, 27). The values of the angles between [Asp114 Oδ1 – His237 Nδ1 – His237 Hδ1] and [water O540 – His237 Nδ1 – His237 Hδ1] are indicated along with the distance between His237 Nε2 - T3 copper (with arrows); (c, d) The ring rotation that brings the Hδ1 to the optimal position for a hydrogen bond with Asp114 Oδ1 (c) and the water (d) are shown. The new χ2 dihedral angle and the corresponding His237 Nε2 - T3 copper distances are indicated.*

Table S3.1*. Exchange and spin lattice relaxation rates at 298 K for SLAC-T1D/Y108F. In brackets the values for SLAC-T1D are shown for comparison (17).* R_{1A} *and* R_{1B} *are the spin-lattice relaxation rates for state A and B respectively. Errors in the values are ~ 5% from the duplicate experiments.*

	3 – 5	9 – 11	13 – 12
k_A (s^{-1})	37 (33)	51 (29)	26 (29)
k_B (s^{-1})	60 (62)	91 (91)	39 (34)
k_{ex} (s^{-1})	97 (95)	142 (120)	65 (63)
K_{eq} (k_A/k_B)	0.62 (0.53)	0.56 (0.32)	0.67 (0.85)
R_{1A} (s^{-1})	225 (225)	240 (240)	170 (170)
R_{1B} (s^{-1})	518 (457)	524 (464)	483 (492)

Table S3.2. *^{1}H and ^{15}N chemical shift in ppm of the paramagnetically shifted resonances (> 21 ppm in 1D ^{1}H WEFT spectrum) at 298 K. Resonance showing no change between SLAC-T1D/Y108F and SLAC-T1D are highlighted. Resonance pairs undergoing chemical exchange are color coded as red for 3-5, green for 9-11 and blue for 13-12. ^{15}N chemical shift of resonance 7, 8, 17 and 18 are not observed from the ^{15}N-^{1}H HMQC spectra. Resonance 7 and 8 were reported to be carbon attached protons (17) while the ^{1}H resonance of 17 and 18 are broad (~ 1.1 ppm), which can affect the evolution period d2 in the ^{15}N-^{1}H HMQC (Figure S3.2). Since the d2 was set to 0.5 ms, corresponding to the ^{1}H line with of 0.8 ppm (Figure 2.1) at 600 MHz, resonance 17 and 18 might not be observable due to their large line broadening.*

Resonance	SLAC-T1D		SLAC-T1D/Y108F	
	^{1}H	^{15}N	^{1}H	^{15}N
3	22.00	291.65	22.24	294.24
4	23.40	245.21	24.53	251.16
5	24.75	330.35	25.07	333.41
6	26.46	461.91	25.95	459.73
7	29.26	-	29.26	-
8	31.65	-	31.65	-
9	34.88	450.30	35.43	456.79
11	36.95	477.39	37.68	485.19
12	39.24	535.44	39.20	539.05
13	41.82	581.87	42.04	565.49
15	43.09	569.04	43.13	570.38
16	44.11	574.13	43.67	559.61
17	49.17	-	49.17	-
18	52.52	-	52.52	-

***Table S3.3**. ^{1}H and ^{15}N chemical shift in ppm at 298 K for the resonance between 12 and 21 ppm of the RO state.*

Resonance	SLAC-T1D	
	^{1}H	^{15}N
a1	12.82	179
a2	19.01	266
b1	16.29	-
b2	19.06	270
c1	16.65	248
c2	20.59	277
d1	18.01	-
d2	20.02	275
e1	18.64	-
e2	21.64	-
x1	13.58	185
x2	14.68	213
y	15.43	232
w	13.29	190
z	19.90	265

***Table S3.4**. Potential hydrogen bond acceptors for T3 His Nδ1 atoms as defined by (33). Data based on chains E and F from PDB entry 6s0O (resolution 1.80Å) (26).*

Histidine	Potential hydrogen bond acceptors
His 105.E	Asp 260.F Oδ1 and H_2O 546.E O
His 290.F	Gln 292.F Oε1 and H_2O 540.F O
His 159.E	Glu 164.E CO and H_2O 540.E O
His 237.F	Asp 114.E Oδ1 and H_2O 501.E O

Table S3.5*. The estimated hyperfine constant A from the fit in of the chemical shift temperature dependence in Figure 3.2b of the main text using equation 1.5.*

Resonance	Hyperfine coupling constant *A* (MHz)
a1	0.7 +/- 0.2
b1	2.7 +/- 0.3
c1	1.5 +/- 0.1
d1	3.0 +/- 0.5
a2	2.0 +/- 0.2
b2	2.0 +/- 0.2
c2	2.3 +/- 0.4
d2	2.2 +/- 0.3

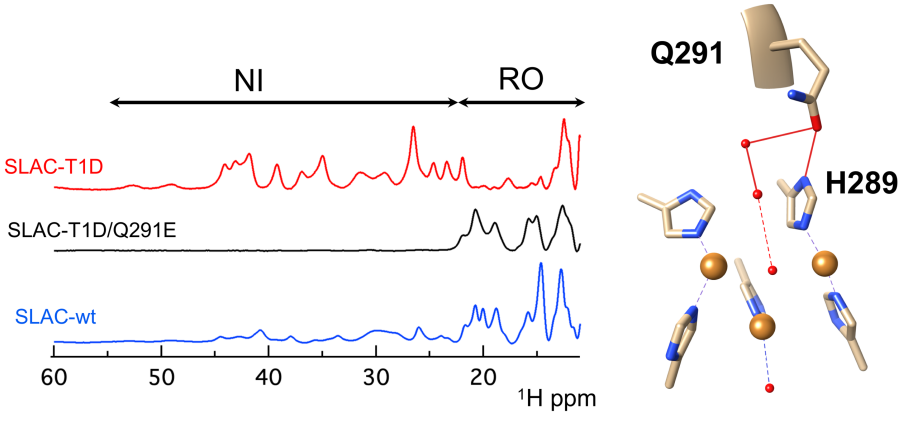
3.5 References

1. Gupta, A., I. Nederlof, S. Sottini, A.W.J.W. Tepper, E.J.J. Groenen, E.A.J. Thomassen, and G.W. Canters. 2012. Involvement of Tyr108 in the Enzyme Mechanism of the Small Laccase from *Streptomyces coelicolor*. *Journal of the American Chemical Society*. 134:18213–18216.
2. Heppner, D.E., C.H. Kjaergaard, and E.I. Solomon. 2014. Mechanism of the Reduction of the Native Intermediate in the Multicopper Oxidases: Insights into Rapid Intramolecular Electron Transfer in Turnover. *J. Am. Chem. Soc.* 136:17788–17801.
3. Quintanar, L., J. Yoon, C.P. Aznar, A.E. Palmer, K.K. Andersson, R.D. Britt, and E.I. Solomon. 2005. Spectroscopic and Electronic Structure Studies of the Trinuclear Cu Cluster Active Site of the Multicopper Oxidase Laccase: Nature of Its Coordination Unsaturation. *J. Am. Chem. Soc.* 127:13832–13845.
4. Tepper, A.W.J.W., S. Milikisyants, S. Sottini, E. Vijgenboom, E.J.J. Groenen, and G.W. Canters. 2009. Identification of a Radical Intermediate in the Enzymatic Reduction of Oxygen by a Small Laccase. *J. Am. Chem. Soc.* 131:11680–11682.
5. Yoon, J., and E.I. Solomon. 2007. Electronic Structure of the Peroxy Intermediate and Its Correlation to the Native Intermediate in the Multicopper Oxidases: Insights into the Reductive Cleavage of the O−O Bond. *J. Am. Chem. Soc.* 129:13127–13136.
6. Kielb, P., H.B. Gray, and J.R. Winkler. 2020. Does Tyrosine Protect *S. Coelicolor* Laccase from Oxidative Degradation? DOI: 10.26434/chemrxiv.12671612.v1
7. Tian, S., S.M. Jones, and E.I. Solomon. 2020. Role of a Tyrosine Radical in Human Ceruloplasmin Catalysis. *ACS Cent. Sci.* DOI: 10.1021/acscentsci.0c00953
8. Hammes-Schiffer, S. 2006. Hydrogen Tunneling and Protein Motion in Enzyme Reactions. *Acc. Chem. Res.* 39:93–100.
9. Hammes-Schiffer, S., and S.J. Benkovic. 2006. Relating Protein Motion to Catalysis. *Annual Review of Biochemistry*. 75:519–541.
10. Henzler-Wildman, K.A., V. Thai, M. Lei, M. Ott, M. Wolf-Watz, T. Fenn, E. Pozharski, M.A. Wilson, G.A. Petsko, M. Karplus, C.G. Hübner, and D. Kern. 2007. Intrinsic motions along an enzymatic reaction trajectory. *Nature*. 450:838–844.
11. Poulos, T.L. 2003. Cytochrome P450 flexibility. *Proceedings of the National Academy of Sciences*. 100:13121–13122.
12. Dasgupta, R., K.B.S.S. Gupta, F. Nami, H.J.M. de Groot, G.W. Canters, E.J.J. Groenen, and M. Ubbink. 2020. Chemical Exchange at the Trinuclear Copper Center of Small Laccase from *Streptomyces coelicolor*. *Biophysical Journal*. 119:9–14.

13. Machczynski, M.C., and J.T. Babicz. 2016. Correlating the structures and activities of the resting oxidized and native intermediate states of a small laccase by paramagnetic NMR. *Journal of Inorganic Biochemistry*. 159:62–69.
14. Zaballa, M.-E., L. Ziegler, D.J. Kosman, and A.J. Vila. 2010. NMR Study of the Exchange Coupling in the Trinuclear Cluster of the Multicopper Oxidase Fet3p. *J. Am. Chem. Soc.* 132:11191–11196.
15. Ciofi-Baffoni, S., A. Gallo, R. Muzzioli, and M. Piccioli. 2014. The IR-^{15}N-HSQC-AP experiment: a new tool for NMR spectroscopy of paramagnetic molecules. *Journal of Biomolecular NMR*. 58:123–128.
16. Gelis, I., N. Katsaros, C. Luchinat, M. Piccioli, and L. Poggi. 2003. A simple protocol to study blue copper proteins by NMR. *European Journal of Biochemistry*. 270:600–609.
17. Dasgupta, R., K.B.S.S. Gupta, F. Nami, H.J.M. de Groot, G.W. Canters, E.J.J. Groenen, and M. Ubbink. 2020. Chemical Exchange at the Trinuclear Copper Center of Small Laccase from *Streptomyces coelicolor*. *Biophysical Journal*. 119:9–14.
18. Bertini, I., C. Luchinat, G. Parigi, and E. Ravera. 2017. NMR of paramagnetic molecules: applications to metallobiomolecules and models. Second edition. Amsterdam: Elsevier.
19. Banci, L., I. Bertini, and C. Luchinat. 1990. The ^{1}H NMR parameters of magnetically coupled dimers—The Fe2S2 proteins as an example. In: Bioinorganic Chemistry. Berlin, Heidelberg: Springer. pp. 113–136.
20. Bubacco, L., E. Vijgenboom, C. Gobin, A.W.J.W. Tepper, J. Salgado, and G.W. Canters. 2000. Kinetic and paramagnetic NMR investigations of the inhibition of *Streptomyces antibioticus* tyrosinase. *Journal of Molecular Catalysis B: Enzymatic*. 8:27–35.
21. Tepper, A.W.J.W., L. Bubacco, and G.W. Canters. 2006. Paramagnetic Properties of the Halide-Bound Derivatives of Oxidised Tyrosinase Investigated by ^{1}H NMR Spectroscopy. *Chem. Eur. J.* 12:7668–7675.
22. Battistuzzi, G., G. Di Rocco, A. Leonardi, and M. Sola. 2003. ^{1}H NMR of native and azide-inhibited laccase from *Rhus vernicifera*. *Journal of Inorganic Biochemistry*. 96:503–506.
23. Quintanar, L., C. Stoj, T.-P. Wang, D.J. Kosman, and E.I. Solomon. 2005. Role of Aspartate 94 in the Decay of the Peroxide Intermediate in the Multicopper Oxidase Fet3p. *Biochemistry*. 44:6081–6091.
24. Bertini, Ivano., Paola. Turano, and A.J. Vila. 1993. Nuclear magnetic resonance of paramagnetic metalloproteins. *Chem. Rev.* 93:2833–2932.
25. Patt, S.L., and B.D. Sykes. 1972. Water Eliminated Fourier Transform NMR Spectroscopy. *J. Chem. Phys.* 56:3182–3184.
26. Gabdulkhakov, A., I. Kolyadenko, O. Kostareva, A. Mikhaylina, P. Oliveira, P. Tamagnini, A. Lisov, and S. Tishchenko. 2019. Investigations of Accessibility of T2/T3 Copper Center of Two-Domain Laccase from *Streptomyces griseoflavus* Ac-993. *International Journal of Molecular Sciences*. 20:3184.
27. Pettersen, E.F., T.D. Goddard, C.C. Huang, G.S. Couch, D.M. Greenblatt, E.C. Meng, and T.E. Ferrin. 2004. UCSF Chimera—A visualization system for exploratory research and analysis. *Journal of Computational Chemistry*. 25:1605–1612.
28. Solomon, E.I., A.J. Augustine, and J. Yoon. 2008. O_2 Reduction to H_2O by the multicopper oxidases. *Dalton Trans.* 3921–3932.
29. Machczynski, M.C., E. Vijgenboom, B. Samyn, and G.W. Canters. 2004. Characterization of SLAC: A small laccase from *Streptomyces coelicolor* with unprecedented activity. *Protein Science*. 13:2388–2397.
30. Jeener, J., B.H. Meier, P. Bachmann, and R.R. Ernst. 1979. Investigation of exchange processes by two-dimensional NMR spectroscopy. *J. Chem. Phys.* 71:4546–4553.
31. Farrow, N.A., O. Zhang, J.D. Forman-Kay, and L.E. Kay. 1994. A heteronuclear correlation experiment for simultaneous determination of ^{15}N longitudinal decay and chemical exchange rates of systems in slow equilibrium. *J Biomol NMR*. 4:727–734.
32. Skálová, T., J. Dohnálek, L.H. Østergaard, P.R. Østergaard, P. Kolenko, J. Dušková, A. Štěpánková, and J. Hašek. 2009. The Structure of the Small Laccase from *Streptomyces coelicolor* Reveals a Link between Laccases and Nitrite Reductases. *Journal of Molecular Biology*. 385:1165–1178.
33. Mills, J.E.J., and P.M. Dean. 1996. Three-dimensional hydrogen-bond geometry and probability information from a crystal survey. *J Computer-Aided Mol Des*. 10:607–622.

Chapter 4

The resting oxidized state of small laccase analyzed with paramagnetic NMR spectroscopy



This chapter is published as:
Dasgupta, R., K.B.S.S. Gupta, H.J.M. de Groot, and M. Ubbink. 2021. The Resting Oxidized State of Small Laccase Analyzed with Paramagnetic NMR Spectroscopy. *ChemPhysChem*. 22:733–740. DOI: https://doi.org/10.1002/cphc.202100063

The enzyme laccase catalyzes the reduction of dioxygen to water at the trinuclear copper center (TNC). The TNC comprises a type-3 (T3) and a type-2 (T2) copper site. The paramagnetic NMR spectrum of the small laccase from *S. coelicolor* (SLAC) without the substrate shows a mixture of two catalytic states, the resting oxidized (RO) state and the native intermediate (NI) state. An analysis of the resonances of the RO state is reported. In this state, hydrogen resonances only of the T3 copper ligands can be found, in the region of 12 – 22 ppm. Signals from all six histidine ligands are found and can be attributed to Hδ1, Hβ or backbone amide H^N nuclei. Two sequence specific assignments are proposed on the basis of a second-coordination shell variant that also lacks the copper ion at the T1 site, SLAC-T1D/Q291E. This double mutant is found to be exclusively in the RO state, revealing a subtle balance between the RO and the NI states.

4.1 Introduction

The multicopper oxidase laccase can perform oxygen reduction with very little overpotential (~ 20 mV).(1) It comprises two active sites, a type-1 (T1) copper site to oxidize substrates and a tri-nuclear copper center (TNC) to reduce dioxygen to water. The TNC can be divided in a type-3 (T3) and a type-2 (T2) copper site. The T1 site is comprised of a single Cu(II) ion and is characterized by a strong 600 nm response in the absorption spectrum due to metal-sulfur transition between the Cu(II) and cysteine.(2) The T3 site has two interacting Cu(II) ions via a OH^- group while the T2 site has a single Cu(II) ion in a trigonal planar geometry coordinated to two histidine ligands and a water/OH^- group.(2) The current model of the reaction mechanism was previously described in detail (Figure 1.3).(3) In brief, the resting oxidized (RO) state is reduced to the fully reduced (FR) state by extracting four electrons from the substrates at the T1 site. The TNC has three cuprous ions in the FR state and can bind an oxygen molecule. Donation of two electrons from the TNC copper ions to the molecular oxygen leads to the formation of the peroxide intermediate (PI) state. At this stage the TNC needs one additional electron for complete oxygen reduction, which can be transferred from the reduced T1 site. In addition, for small laccase and human ceruloplasmin an electron can be transferred from the tyrosine residue near the T2 site, by forming a tyrosine radical.(4, 5) The two electron transfers coupled with a single proton transfer convert the PI state to the native intermediate (NI) state in which the peroxide bond between the oxygen atoms is broken. After three protons transfers from the protein environment, two water molecules are released and the NI state is converted into the RO state without the substrates, or into the FR state, with the substrates in the environment.

However, somewhat in contrast with this standard model, the NMR spectrum of a small laccase from *S. coelicolor* (SLAC) showed that the enzyme without substrate exists as a mixture of RO and NI states with all the copper ions in the cupric form (chapter 2 and 3).(6, 7) In the NI state, the T2 copper ion is coupled to the T3 copper ions via an oxygen atom (Figure 1.3 and S4.2b). The T2 copper ion is decoupled in the RO state (Figure 1.3. and S4.2a). The ^{1}H signals in the NMR spectrum of the RO state are less paramagnetically shifted (12 to 22 ppm) than those of the NI state (22 to 55 ppm).(6, 7) The wild type protein (SLAC-wt) is predominantly in the RO state, while the T1 site copper depleted mutant (SLAC-T1D the native, holoprotein, with copper ions in all sites) is mostly in the NI state (chapter 2 and 3).(6, 7) Five chemical exchange processes ascribed to ring motions of histidines coordinating coppers in both T3 and T2 sites were shown to be present for the NI state of SLAC-T1D (chapter 2 and 3).(7, 8) Further characterization of these exchange processes requires sequence specific assignment of the resonances to the histidine ligand nuclei. The assignment of the resonances is complicated by the paramagnetic nature of the copper ions, resulting in line broadening and hyperfine shifted resonances (up to 60 ppm in SLAC). This makes it impossible to use standard multidimensional NMR experiments for the assignments. Mutations in the second shell of coordination were considered as a means to obtain assignments. Using such a mutation, two of the chemical exchange processes in the NI state could be assigned to the T2 site histidines (chapter 3).(7) However, a detailed characterization of the RO state could not be done due to its low population in SLAC-T1D, resulting in the low S/N ratio of the corresponding resonances.(7)

In the current study, SLAC-wt is studied to characterize the RO state. The electronic coupling between the two coppers leads to fast electronic relaxation, yielding observable signals even for nuclei close to the metals.(9–11) The signals from nuclei in the T2 site ligands are broadened beyond detection because of the longer electronic relaxation time of the isolated electron spin on the copper.(7, 10, 12) The resonances from the T1 site are expected to be shifted to different spectral regions, 500 to 700 ppm for cysteine Hβ, 30 to 50 ppm for histidine ring, < 0 ppm for histidine Hβ and 12 to 20 ppm for other ligands(13–15). The signals from the T3 site are observed in the region from 12 to 22 ppm(6). They can be differentiated from the signals of the T1 site by their temperature dependence. T3 site signals have anti-Curie behavior, i.e. an increase in hyperfine coupling with increase in temperature, whereas the T1 site signals have Curie type behavior, i.e. a decrease in hyperfine coupling with increasing in temperature(12). The temperature dependence of the resonances in the 12-22 ppm region observed for the RO state was reported(6) and later shown to have anti-Curie. This suggests that all in that region arise from the T3 site ligands.

Using paramagnetically tailored NMR experiments and a mutation near the T3 site, the sequence specific assignment of two T3 site histidine ligands is reported for the RO state. In addition, resonances corresponding to all the six histidine ligands

of the T3 site could be found. Interestingly, the mutant enzyme is exclusively in the RO state, indicating that there is a subtle balance between the NI and RO states. Ultimately, assignment of the NMR resonances of nuclei at the heart of active site can lead to a better description of the TNC and aid in characterizing underlying motions, which may help to explain how laccases can so efficiently break the stable dioxygen bond.

4.2 Results and discussions

RO state in SLAC-wt

The NMR spectra of the RO state comprise signals from the T3 site histidine ligands that spans the spectral region between 12 and 22 ppm, while the NI state has signals from both the T3 and the T2 site histidine ligands in the spectral region between 22 and 55 ppm (chapter 3).(6, 7) The spectrum of SLAC-wt reveals a mixture of the NI and the RO states, similar to SLAC-T1D (chapter 3).(6, 7) The relative intensities of the signals in the RO and the NI spectral regions shows that SLAC-wt is predominantly in the RO state, contrary to SLAC-T1D. A Gaussian deconvolution of the ^{1}H spectral region between 10 and 22 ppm yields 14 resonances (Figure 4.1a). On the basis of 2D EXSY/NOESY (Figure 4.1b) and HMQC (Figure 4.1c) spectra, it can be concluded that some resonances derive from overlapping signals. The resonance at ~11 ppm is a superposition of proton signals (u0, c0, b0, e0 and x0), the resonances at ~16 ppm (u1 and b1) and 21.5 ppm (e2 and θ) are from two protons with strong overlap, and the resonance at ~19 ppm (b2, e1 and a2) is the summation of three proton signals. The cross-peaks between the resonances in the spectral region of 10 to 12 ppm have low S/N ratio and, therefore, we focus on the resonances in the region of 12 to 22 ppm for further analysis (a1, x1, d0, x2, u1, b1, c1, d1, b2, e1, a2, d2, c2, θ and e2) (Figure 4.1b). These resonances show anti-Curie behavior, where the hyperfine coupling increases with temperature (Figure 4.1e), which is well in line with previous observations.(6) Using the coupled two-metal center model (equation 1.2), the singlet-triplet energy gap was estimated to be $2J = -560$ cm^{-1} with $S = 0$ being the ground state and the $S = 1$ being the excited state. This is within the range of the reported values for the RO state of laccases (–550 to –620 cm^{-1}).(6, 7, 16) Extrapolation of the fitted curves to infinite temperature yields the diamagnetic chemical shifts (δ_{dia}).(12, 17, 18) On the basis of BMRB statistics, resonances related to the Hδ1, Hβ and backbone amide H^{N} protons of the T3 histidine ligand are distinguished (Figure 4.1e, see also Experimental Procedures in the Supporting Information). Resonances e2, c2, d2, b2, c1 and a2 derive from Hδ1, with a globally fitted δ_{dia} of 10 ppm, in line with the BMRB average for the histidine ring Hδ1 of 9.5 ppm. The resonances e1, d1, b1 and u1 are from Hβ with a δ_{dia} of 3.3 ppm matching the BMRB average of histidine Hβ of

3.2 ppm, while resonances a1, x2, d0 and x1 are attributed to backbone amide H^N with a δ_{dia} of 8.6 ppm with a BMRB average for the histidine backbone amide proton of 8.2 ppm. Assignments of resonances to nitrogen attached protons were validated by observation in a ^{15}N-^{1}H HMQC spectrum. Finally, an additional resonance θ is is poorly resolved due to strong overlap with resonance c2.

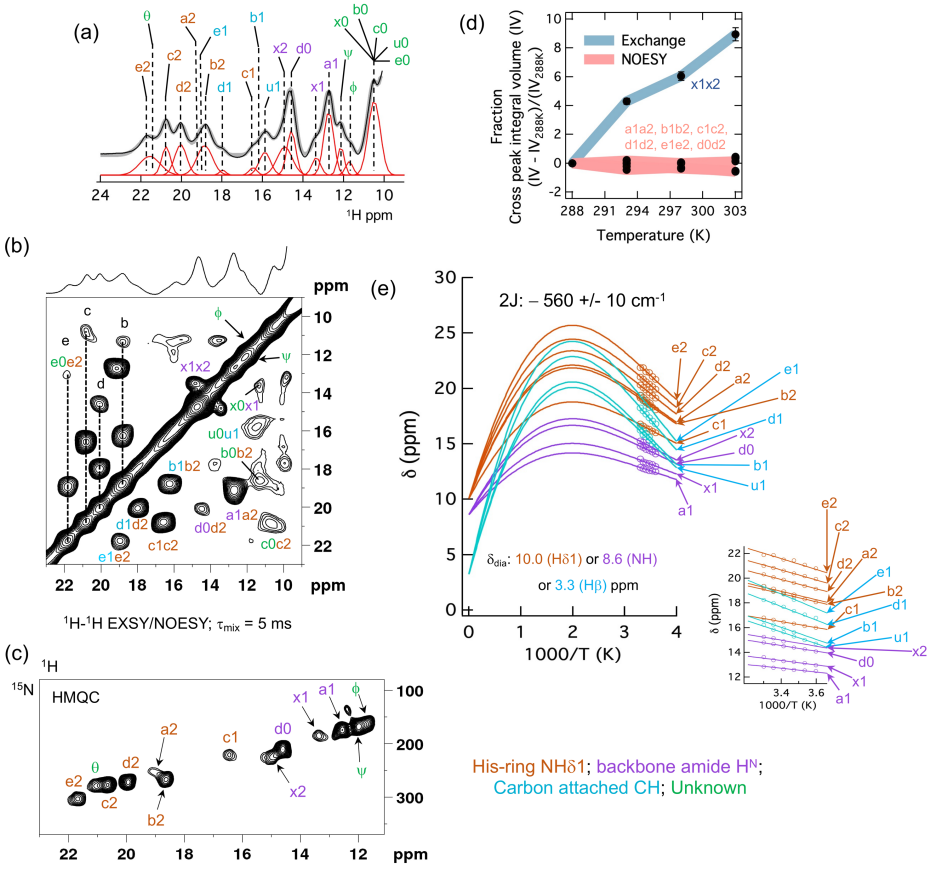


Figure 4.1*. NMR spectra of SLAC-wt. (a) 1D WEFT (19, 20) ^{1}H spectrum of the spectral region from 10 to 24 ppm corresponding to the RO state. The WEFT delay was set to 100 ms. Gaussian deconvolution is shown in red and the summation of the deconvoluted resonances is indicated with a solid grey trace; (b) 2D ^{1}H-^{1}H EXSY/NOESY spectrum at 298 K with mixing time (τ_{mix}) of 5 ms. The 1D ^{1}H spectrum is shown on top of the spectrum; (c) 2D ^{15}N-^{1}H HMQC spectrum. The delay for polarization transfer was set to 0.5 ms (7); (d) The temperature dependence of the fractional cross peak integrals to differentiate between the NOE and exchange cross peaks; (e) Temperature dependence of the chemical shift of the resonances marked in panels a, b and c. The solid lines represent the fit using equation S1. The 2J value and the diamagnetic chemical shifts are shown. The inset shows an enlargement of the experimental region. The corresponding hyperfine coupling constants A (MHz) are given in Table S4.3. The chemical shift values at different temperatures for each*

resonance in panel e is given in Table S4.4. The chemical shift values for resonances a2, x2, e1 and b1 were obtained from the temperature dependence of the cross peak in panel b. Color codes are given below panel d as brown for protons from the His-ring Hδ1, purple for the protons of the backbone amide H^N, cyan for the carbon attached protons and green for unknown. All spectra were recorded at 14 T.

The temperature dependence of the cross-peak intensities from the EXSY/NOESY spectrum shows that resonances x1 and x2 are in chemical exchange (Figure 4.1d), whereas other peaks are NOE cross peaks (a1a2, b1b2, c1c2, d0d2, d1d2 and e1e2). Cross peaks e1e2, d1d2 and b1b2 are the NOEs between the Hδ1 and Hβ protons, whereas cross peaks d0d2, and a1a2 are between the Hδ1 and backbone amide H^N protons. Cross peak c1c2 will be discussed further in the analyses of the double mutant SLAC-T1D/Q291E. Figure 4.1b shows that the resonances c, b, d and e have two cross peaks. The cross peaks e0e2, b0b2 and c0c2 could not be analyzed further due to their low S/N ratio but for resonance d NOE cross peaks are present between Hδ1 – Hβ and Hδ1 – backbone amide H^N protons (Figure 4.1b and e).

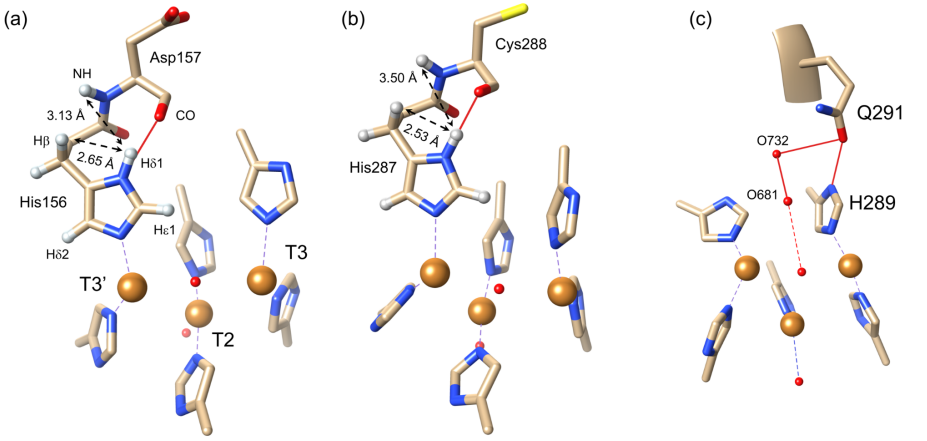


***Figure 4.2**. Histidine ligands in the TNC of SLAC. (a, b) Protons are shown near Hδ1 of His156 (a) and His287 (b) from the crystal structure of small laccase from S. coelicolor (PDB 3cg8)(15). Hydrogen bonds are shown as red lines. Amino acid residues are shown in golden sticks and copper ions as orange spheres. Distances between the Hδ1-Hβ and Hδ1-H^N are shown as double-sided arrows. Protons of the histidine ring are marked in panel a. The protons were modelled using the "AddH" algorithm as implemented in UCSF Chimera program(16) (for more details, see supporting information). His289 and 287 in panel a and His156 and 158 in panel b are not shown for clarity; (c) Hydrogen bonds are shown from Gln291 Oε1 to His289 Nδ1 and the bound water molecule O732 (red sphere), which is part of the water channel (Figure S4.3). O732 is hydrogen bonded to the next water molecule O681*

in the water channel. A possible hydrogen bond from O681 to the T3 site oxygen is shown as a red dashed line. His156, 158 and 102 are not shown for clarity.

Analysis of the crystal structure (PDB 3cg8) (21) of *S. coelicolor* SLAC reveals that in His156 and His287 (numbering from the crystal structure 3cg8) the Hδ1 proton is close to both Hβ and a backbone amide H^N proton (Figure 4.2), which could give rise to the observed NOE cross peak pairs for the d resonances. The Hδ1 proton of His156 is at 2.65 Å from the nearest Hβ proton and at 3.13 Å from the backbone amide H^N of Asp157. In His287, the Hδ1 proton is at 2.53 Å from the closest Hβ proton and at 3.50 Å from the backbone amide H^N of Cys288 (Figure 4.2). According to previous studies the resonances of nuclei in ligands of the T1 site, including Cys288, are subject to Curie behavior, and the hyperfine coupling decreases with increasing in temperature.(23) In contrast, resonance d0 shows an anti-Curie behavior (Figure 4.1e), which is generally observed for nuclei interacting with a coupled metal ion system.(12, 17, 18, 23) This suggests that the resonance d can be assigned to His156, showing NOEs between the Hδ1 - Hβ and Hδ1 - Asp157 H^N. The chemical shifts of the Hδ1, Hβ and Asp157 backbone amide H^N protons are 20, 18 and 14.5 ppm, with the paramagnetic shift contributions of about 10, 15 and 6 ppm, respectively. Interestingly, the paramagnetic contribution to the chemical shift of Hδ1 is less than for Hβ, although the former is four bonds away from the metal center, and the latter five. Perhaps this can be explained by (a) the higher electronegativity of nitrogen sequestering much spin density compared to carbon, resulting in less spin density on the nitrogen attached proton and (b) His156 Hδ1 having a strong hydrogen bond with the carbonyl CO of Asp157 that can result in an extended Nδ1-Hδ1 bond, thus further reducing the electron spin density on the proton. The shift of the H^N appears quite large for an FCS of a nucleus so many bonds away from the copper ion but it is noted that this is based on an estimate for the diamagnetic chemical shift of 8.6 ppm. Amide proton chemical shifts can vary widely. Also, a pseudo-contact shift could contribute to the observed shift.

Similar to the cross peak d0d2, a1a2 is also a NOE between a Hδ1 (a1, 12.68 ppm) and a backbone amide H^N proton (a2, 19.17 ppm). From the available crystal structures of small laccase, it is not possible to specifically assign it to any of the T3 histidine ligands. Cross peaks b1b2 and e1e2 can be from any of the remaining five T3 histidine ligands. Overall, resonances a, b, d (1-2) and e represent signals from four of the six T3 site histidine ligands, with resonance d (1-2) assigned to His156 and d0 to Asp 157 H^N (Table S4.1). A two-site, slow chemical exchange is observed for a backbone amide H^N proton (resonances x1 and x2, Figure 4.1). Although it is paramagnetically shifted, there are no NOE cross peaks with other resonances from the T3 site histidine ligands. In the state corresponding to x1, a weak cross peak is observed with resonance x0 (Figure 4.1b). It remains unclear to which nuclei these signals can be assigned.

Comparison between SLAC-wt and SLAC-T1D

Similar to SLAC-wt, the NMR spectrum of SLAC-T1D shows a mixture of the RO and the NI states.(6, 7) A strong response in the NI region (22 to 55 ppm) compared to the RO region (12 to 22 ppm) provides convincing evidence that SLAC-T1D is predominantly in the NI state (Figure 4.3a).(7) The proton resonances from the 1D ^{1}H WEFT spectra of the RO region in SLAC-T1D are not well resolved due to their low S/N ratio (Figure 4.3b). However, the RO spectral region in the 2D ^{1}H-^{1}H EXSY/NOESY spectra shows that the cross-peaks (a1a2, b1b2, c1c2, d1d2, e1e2 and x1x2) are present in both SLAC-T1D and SLAC-wt (Figure 4.3d). Cross-peak d0d2 is not observed in SLAC-T1D due to its low S/N ratio. The ^{15}N-^{1}H HMQC spectrum is also similar between the two proteins, although some changes can be observed (Figure 4.3e). In SLAC-T1D, resonances a1, x1, y, b2 and d2 are shifted downfield, while resonance x2 is shifted upfield in the proton dimension and resonance c1 is shifted downfield in the nitrogen dimension. Additional resonances w and z are observed in SLAC-T1D. A downfield shifted resonance is correlated to an increase in the spin density on the nucleus and vice-versa for an upfield shifted resonance.(12, 24) This suggests that in the RO state of SLAC-T1D, protons represented by resonances a1, x1, y, b2 and d2 have more spin density and x2 has less spin density compared to SLAC-wt. These changes can be attributed to the loss of the T1 copper in the T1D mutant, due to which the TNC is affected structurally and electronically.(6) Some structural change of the TNC is also suggested by the change in the singlet-triplet energy gap $2J = -560$ cm^{-1} for the RO state of SLAC-wt which is $2J = -600$ cm-1 for SLAC-T1D (7), because it was shown that a change in 2J value is related to the change in the angle between the hydroxyl bridged T3 copper ions (Cu^{2+}– OH^{-} – Cu^{2+}) and distance between the T3 coppers.(2, 3)

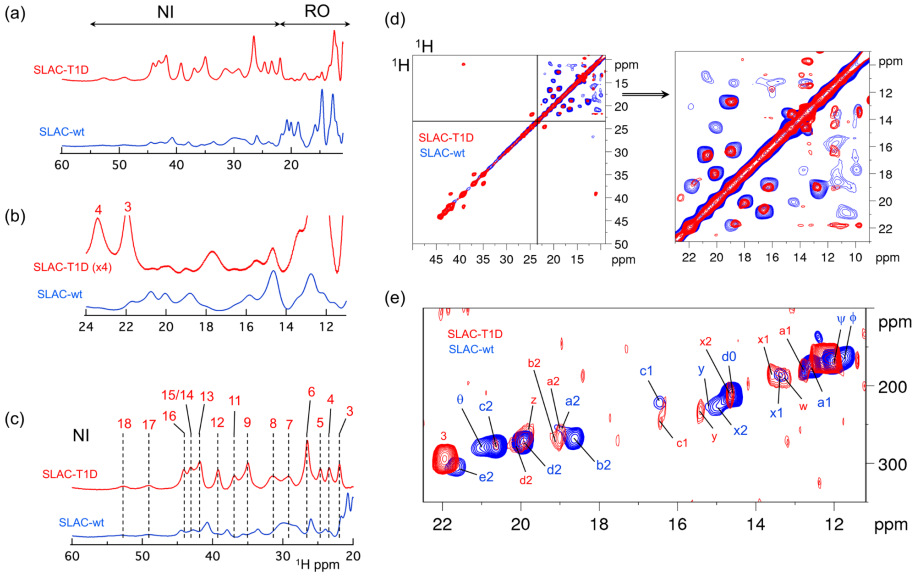


***Figure 4.3**: Comparison of SLAC-T1D and SLAC-wt. (a) Overlaid 1D ^{1}H spectra of SLAC-T1D (red) and SLAC-wt (blue). The spectral regions for the NI (22 to 55 ppm) and the RO (12 to 22 ppm) states are marked; (b) Expansion of the spectral region corresponding to the RO state where the spectral intensity of SLAC-T1D is multiplied by a factor 4; (c) Expansion of the spectral region corresponding to the NI state. The chemical shift values are given in Table S4.2 of the supporting information; (d) Overlaid ^{1}H-^{1}H EXSY/NOESY spectra of SLAC-wt and SLAC-T1D with an expansion of the spectral region 12 to 22 ppm. The resonance notations are in panel b of Figure 4.1; (e) Overlaid ^{15}N-^{1}H HMQC spectra for the RO region.*

The NI spectral region (22 to 55 ppm) of the 1D ^{1}H WEFT spectrum shows a similar pattern for SLAC-wt and SLAC-T1D. However, the resonances are broader for the SLAC-wt (Figure 4.3c). The resonances in SLAC-T1D are mostly downfield shifted compared to SLAC-wt, except for resonance 16, which is upfield shifted (Table S4.2). For resonances 17 and 18 the variation in chemical shifts are small compared to their large linewidth. In summary, resonances from RO and NI states can be observed for both SLAC-wt and SLAC-T1D proteins, consistent with the previous observations.(6, 7)

Analysis of SLAC-T1D/Q291E

It was shown that a mutation in the second coordination shell can help in assigning the complex paramagnetic NMR spectra of the nuclei in the TNC.(7) Using the SLAC-T1D/Y108F double mutant, the chemical exchange pairs 13-12 and 16-18 of the NI state (Figure 4.3c) were assigned to Hδ1 of His102 and His234 in the T2 site, respectively. (7) Following this method, a residue near the T3 site, Gln29, was mutated to aid in further assignment of the TNC ligands. A double mutant variant SLAC-T1D/Q291E was made to remove the effects of the T1 site copper. Gln291 is located near the T3 site of the TNC and its side chain is oriented toward the water channel leading into the TNC (Figure S4.3). This water channel has been proposed to be the source of protons in the formation of waters from dioxygen(21, 25). Gln291 also forms a strong hydrogen bond with the Nδ1 of His289 (Figure 4.2c), a ligand in the T3 site.

The 1D ^{1}H NMR spectrum of the double mutant SLAC-T1D/Q291E is compared with those of SLAC-T1D and SLAC-wt in Figure 4.4a. The NMR spectrum of the double mutant SLAC-T1D/Y108F was reported to be a mixture of the NI and the RO states with the NI state being the most populated, similar to the situation in SLAC-T1D(7). The NMR spectrum of SLAC-T1D/Q291E shows the enzyme to be exclusively in the RO state, without any signals from the NI state (Figure 4.4a).

A gaussian deconvolution of the ^{1}H spectral region between 12 and 24 ppm shows 11 resonances (Figure 4.4b). The 2D ^{1}H-^{1}H EXSY/NOESY spectrum (Figure 4.4d) reveals that the resonance ~14.5 ppm consists of two resonances, d0 and x2, and similarly, in resonance ~16.8 ppm c1' and b1 are overlaid. The response at ~19 ppm consists of four overlapping resonances d1, b2, e1 and a2. The temperature dependencies of the proton chemical shifts can be fitted to a coupled two-metal center model (equation 1.2) yielding a $2J = -560$ cm^{-1}, which is same for SLAC-wt (Figure 4.4e and 4.1e). The resonances could not be specifically assigned to His Hδ1, Hβ and backbone amide H^{N} protons from this temperature dependency due to substantial signal overlap (Figure 4.4b). However, the similarity between the spectra of SLAC-T1D/Q291E and SLAC-wt (Figure 4.5a) indicates comparable assignments.

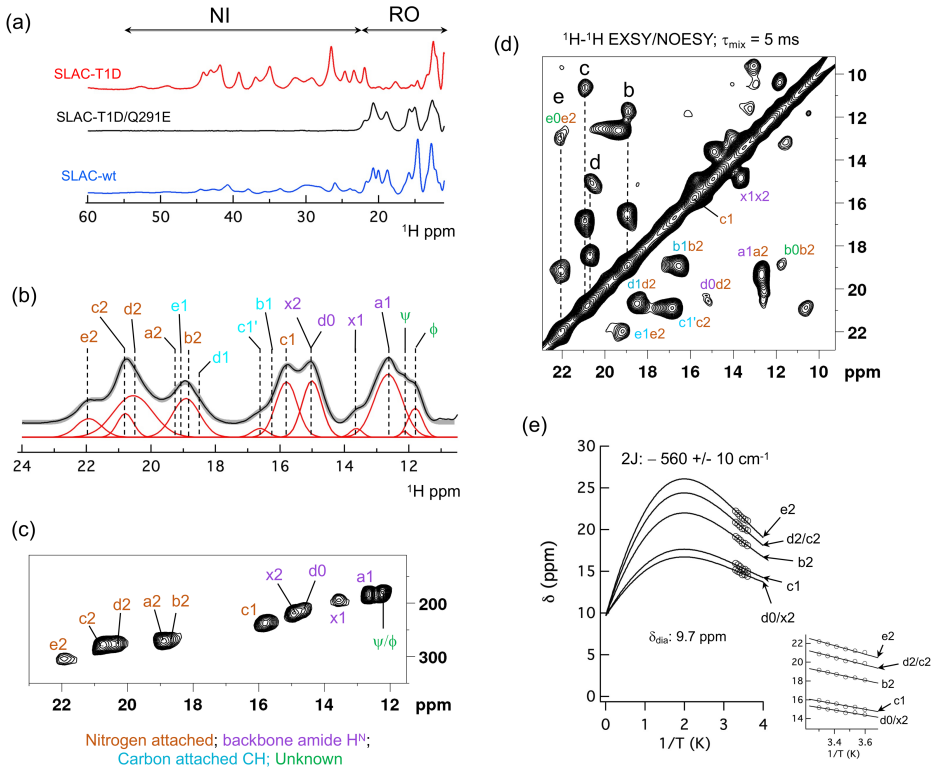


***Figure 4.4**: NMR spectra of SLAC-T1D/Q291E. (a) 1D ¹H spectra of SLAC-T1D (red), SLAC-T1D/Q291E (black) and SLAC-wt (blue). The spectral regions for the NI and the RO states are denoted; (b) 1D ¹H spectrum of SLAC-T1D/Q291E in the spectral region from 11 to 24 ppm. A Gaussian deconvolution is shown in red and the summation of the deconvoluted resonances is shown a solid grey trace; (c) ¹⁵N-¹H HMQC spectrum and (d) ¹H-¹H EXSY/NOESY spectrum of SLAC-T1D/Q291E for the ¹H spectral region of the RO state; (e) Temperature dependence of the resonances marked in panel b. The solid line is the fit to equation 1.5 (for more details see the Experimental procedures in the supporting information). The inset shows an enlargement of the data region. The 2J value and the diamagnetic chemical shifts are shown. The corresponding hyperfine coupling constants A (MHz) are given in Table S4.3. The chemical shifts at different temperatures for each resonance in panel e are given in Table S4.5. The color code and the assignments are same as in Figure 4.1.*

Overlaid NMR spectra of SLAC-wt and SLAC-T1D/Q291E reveal the changes in the RO state of the protein due to the Q291E mutation. The ¹H resonances for SLAC-T1D/Q291E are broader than for SLAC-wt (Figure 4.5a). Chemical shift perturbations are clear from the 2D ¹H-¹H EXSY/NOESY spectra, showing that resonances b2, c2, d0, d2, e2, x1 and x2 are downfield shifted, while resonance c1 is upfield shifted and resonance a1 is unperturbed (Figure panels 4.5b and 4.5d). Most of the resonances are

downfield shifted, suggesting that the Q291E mutation leads to an increase in the spin density delocalization over the ligands in the TNC. It is of interest to note the ^{1}H-^{1}H cross peak c1c2 in SLAC-wt and c1'c2 in SLAC-T1D/Q291E. In the 2D ^{15}N-^{1}H HMQC, the resonance assigned as c1 in SLAC-wt is upfield shifted in the proton dimension and downfield shifted in the nitrogen dimension in the equivalent spectrum of SLAC-T1D/Q291E (Figure 4.5c). However, in the EXSY/NOESY spectrum the cross peak for c1c2 moves slightly downfield in the c1 dimension (Figure 4.5b). This cross-peak was assigned as c1'c2 in SLAC-T1D/Q291E and since c1' is suppressed in the HMQC data compared to the EXSY/NOESY spectrum it can be attributed to a carbon attached proton (Figure 4.4c). It is therefore concluded that the resonances c1 and c1' are overlapped in SLAC-wt (Figure 4.1b and 4.5b), whereas in the spectrum of SLAC-T1D/Q291E they can be distinguished (Figure 4.5c). Resonances c1 and c1' may well belong to different histidines. The temperature dependence of the chemical shift showed that resonance c1 derives from a Hδ1 nucleus. The resonance c2 also derives from a Hδ1 nucleus and because c1' can be attributed to a carbon attached hydrogen, the c1'c2 cross-peak is likely to represent another Hδ1-Hβ NOE from one of the T3 His ligands.

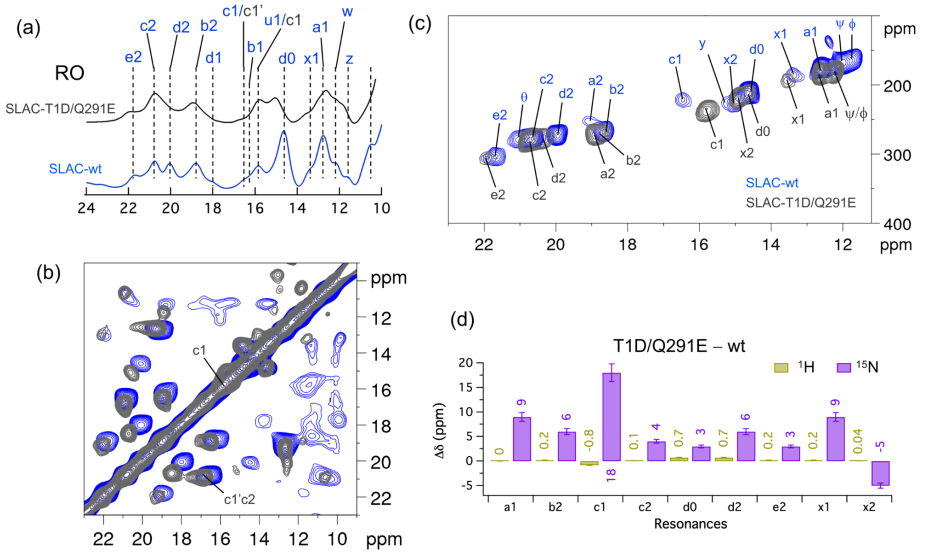


***Figure 4.5**: Comparison of SLAC-T1D/Q291E and SLAC-wt. Overlaid 1D ^{1}H NMR spectra (a), 2D ^{1}H-^{1}H EXSY/NOESY with the resonances c1, c1' and c2 marked (b) and ^{15}N-^{1}H HMQC with all the resonances marked (c) of SLAC-T1D/Q291E (black) and SLAC-wt (blue) of the spectral region 10 to 23 ppm; (d) Chemical shift perturbations as the difference in chemical shift between SLAC-T1D/Q291E and SLAC-wt.*

The chemical shift perturbations between SLAC-T1D/Q291E and SLAC-wt show that the strongest perturbation is for the resonance c1. Since Gln291 has a strong hydrogen bond with His289 (Figure 4.2c), the Q291E mutation can have a pronounced effect on the chemical shift of its Nδ1 and Hδ1 nuclei. Due to the negative charge, Glu291 is likely to have a stronger hydrogen bond with the Hδ1 of His289, increasing the N-H bond length and reducing the spin density on the proton while increasing it on the nitrogen. This will result in an upfield shift for the proton and a downfield shift for nitrogen, in line with the observation in the HMQC spectrum (Figure 4.5c). Therefore, we propose that resonance c1 is from Hδ1 of His289 in the T3 site.

4.3 Conclusion

The NMR spectrum of SLAC-wt is a mixture of the RO and the NI states, and the intensity profile shows that the RO state is most populated. Paramagnetically tailored NMR experiments and the double mutant SLAC-T1D/Q291E helped to provide residue specific assignments for the Hδ1 nuclei of all the six histidine ligands of the T3 site (a2, b2, c1, c2, d2 and e2). The resonances d1 and d2 are assigned to His156 Hβ and Hδ1, respectively, d0 to Asp 157 H^N and resonance c1 is assigned to His289 Hδ1. Cross peaks in the ^1H spectral region of 10-12 ppm could not be analyzed due to their low S/N ratio. Some of the cross peaks (b0b2, c0c2 and u0u1) are associated with resonances assigned to the T3 histidine ligands. Assuming that b0, c0 and u0 arise from the backbone amide H^N protons, cross peaks b0b2 and c0c2 might be NOEs between the His Hδ1 (b2 and c2) and backbone amide protons (b0 and c0). Cross peak u0u1 may be a NOE between a Hβ and a H^N.

Chapter 2 and 3 shows the presence of five chemical exchange processes in the NI state involving Hδ1 protons and attributed to His ring motions.(7, 8) In the RO state, these exchange processes are not observed. Perhaps the exchange is still present but not visible because the lower spin density on nuclei causes smaller FCS. For the NI state, the differences in chemical shift between the states represent ~10% of the FCS. The differences in chemical shift between the different states may be too small in the RO state to result in observable exchange peaks. Alternatively, the RO state may be more rigid, slowing down His ring motions sufficiently to bring the exchange rate outside the window that results in exchange cross peaks (80 – 200 s^{-1}). For the RO state, one exchange process was observed, between signals x1 and x2. However, these resonances do not derive from Hδ1 but from a shifted backbone amide signal. It provides evidence that some motion is occurring in the RO state as well, but we have not been able to assign it to a particular nucleus. We expect that the use of second coordination shell mutations can allow further assignment of the paramagnetic NMR signals from the TNC, providing spectroscopic probes that can help to

understand how motions of the histidine ligands assist in progressing rapidly through the consecutive steps of the catalytic cycle.

4.4 Supporting Information

Site directed mutagenesis

The plasmid pET-20b containing the gene encoding SLAC-T1D (pET-20b/SLAC-T1D) (8) was used as a template to prepare the double mutant SLAC-T1D/Q291E. A two-fragment Gibson assembly (26) approach was used for the site directed mutagenesis. The primers used for the mutagenesis are as follows:

Q291E (mutation is given in bold):
Forward primer: 5'– G TAC CAC AGC CAC GTC **GAA** AGC CAC TCC GAC ATG – 3'
Reverse primer: 5'– CAT GTC GGA GTG GCT **TTC** GAC GTG GCT GTG GTA C – 3'
Primers for generating two-fragments:
pTarget-split-Forward primer: 5'– AAATACTGTCCTTCTAGTGTAGCCGTAGTTAG – 3'
pTarget-split-Reverse primer: 5'– TTCTTGAAGTGGTGGCCTAACTACGG – 3'

Two parts of the pET-20b/SLAC-T1D plasmid were PCR-amplified. Fragment 1 was amplified using the Q291E-forward and pTarget-split-Reverse primers and fragment 2 using the Q291E-reverse and pTarget-split-Forward primers. The resulting fragments (2585 and 2548 base pairs, respectively) were extracted from an agarose gel using GFX™ PCR DNA and Gel Band Purification Kit (Merck, Germany) and combined using Gibson assembly master mix at 50°C.(26) The resulting plasmid pET-20b/SLAC-T1D/Q291E was introduced in the DH5α strain of *Escherichia coli* for propagation. The desired mutation was confirmed by DNA sequencing (BaseClear, Leiden, The Netherlands).

Protein expression and purification

^{15}N uniformly labelled SLAC-wt, SLAC-T1D and SLAC-T1D/Q291E were produced and purified as described previously.(7, 8) Purity was checked using SDS PA-gel electrophoresis and a band ~ 74 kDa was observed in each case (Figure S4.1). This corresponds to the molecular weight of a dimer. However, under native conditions, the molecular weight of the proteins was ~ 105 kD as determined by size-exclusion chromatography coupled to multi-angle light scattering detection, in line with the expected trimeric form.(21)

NMR spectroscopy

Samples contained ~1 mM of protein in 10 mM sodium phosphate buffer pH 7.3 with 10% D_2O. 1D ^1H water eliminated Fourier transform, 2D ^1H-^1H EXSY/NOESY and 2D ^1H-^{15}N HMQC spectra were obtained as described previously.(7, 8) Experiments were carried on a Bruker AV-III HD 600 MHz NMR spectrometer equipped with a TXI cryoprobe.

Modelling protons

The protons were modelled in the crystal structure 3cg8 using "AddH" algorithm as implemented in UCSF Chimera program.(22) The hydrogen bonds were taken into consideration and the protonation states of histidine were kept unspecified so that the program can add hydrogens based on the hydrogen bonds and steric clash.

Temperature dependence of the chemical shift

For two cupric coppers at close distance, antiferromagnetic coupling results in a $S = 0$ state at low temperature. At ambient temperature, the $S = 1$ state can be populated. The energy gap between the two states is given by the coupling constant $2J$ (in cm^{-1}). The observed chemical shift, δ_{obs}, depends on the spin density on the nucleus, given by A, the isotropic hyperfine coupling constant, and value of $2J$ according to equation 1.2. For the temperature dependency of the resonances from SLAC-wt in Figure 4.1e of the main text a global fit algorithm as implemented in IGOR pro 6.37 was used to fit the data by linking the $2J$ values for all the resonances. This resulted in an estimation of δ_{dia} for respective resonances at $k_BT >>> 2J$. These were grouped as His ring Hδ1, His Hβ and H^N by comparison to the chemical shifts obtained from the BMRB statistics, where δ_{dia} for Hδ1, Hβ and H^N are 9.5, 3.2 and 8.2 ppm, respectively. For the final global fit, the $2J$ values for all the data were linked and the δ_{dia} values were linked for resonances belonging to the same type, being Hδ1, Hβ or H^N. For the resonance from SLAC-T1D/Q291E, the $2J$ values and the δ_{dia} were linked for all. The only variable that was not linked during the global fit was A in both the proteins.

Supporting figures and tables

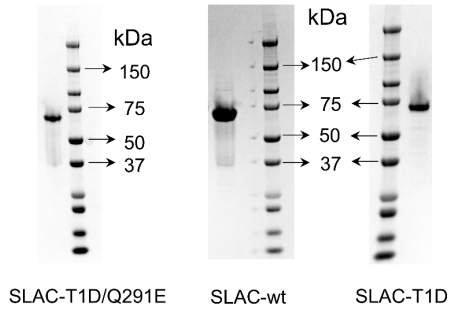


***Figure S4.1**: Image of Bis-Tris precast SDS PAGE-gels (ThermoFischer Scientific) of purified SLAC-T1D/Q291E, SLAC-wt and SLAC-T1D.*

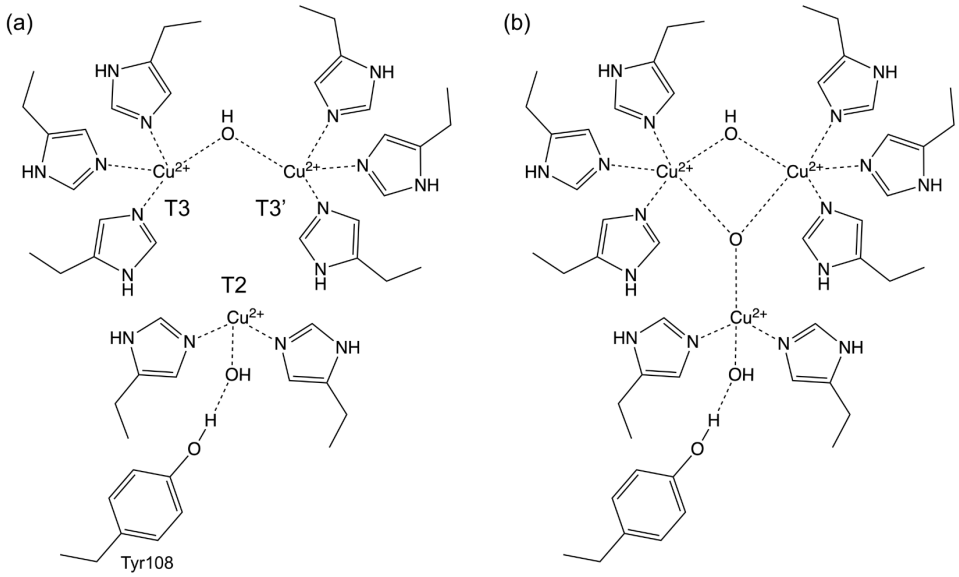


***Figure S4.2**: Schematic of the TNC in (a) the resting oxidized (RO) state and (b) the native intermediate (NI) state. The Tyr108 residue and respective coppers are marked in panel a. The numbering is adopted from the crystal structure 3cg8 (from S. coelicolor, resolution 2.68 Å).(21)*

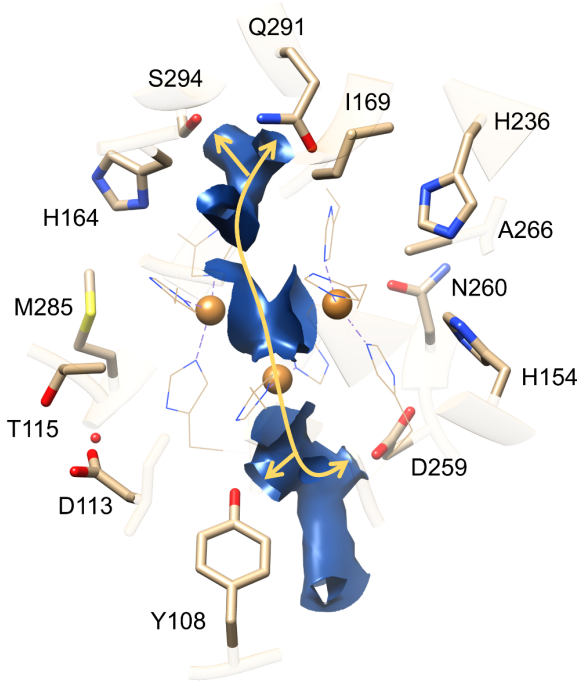


***Figure S4.3**: The second shell residues at the TNC in SLAC from S. coelicolor (PDB 3cg8). (21) The water channel is shown as the electron density surface of the water molecules in the TNC. (25) The double-sided arrows show possible proton transfer paths. Coordinating histidine ligands are shown as wire and the second coordination sphere residues are shown as sticks. The red sphere is a water molecule. The copper ions are shown as orange spheres.*

***Table S4.1**: Chemical shift (ppm) of the resonances in the ^{1}H spectral region of 12 to 22 ppm attributed to the T3 site histidine ligands from SLAC-wt and SLAC-T1D/Q291E at 298 K. The type of protons associated with the resonances are indicated. Hδ1 and Hβ are from histidine and H^{N} is a backbone amide proton. Assignment of resonance c1 and d (d0, d1 and d2) to specific histidine is also indicated. The numbering is adopted from the crystal structure of SLAC from S. coelicolor PDB 3cg8.(21)*

		SLAC-wt		SLAC-T1D/Q291E		Proton	Assignment
	Resonance	^{1}H	^{15}N	^{1}H	^{15}N		Numbering from PDB 3cg8
T3 site histidine ligands	a1	12.68	175	12.68	185	H^{N}	
	a2	19.17	256	19.37	274	Hδ1	
	b1	16.25	-	16.52	-	Hβ	
	b2	18.80	268	18.96	274	Hδ1	
	c1	16.56	221	15.80	240	Hδ1	His289
	c1'	ol	-	16.84	-	Hβ	
	c2	20.81	278	20.95	283	Hδ1	
	d0	14.48	212	15.14	215	H^{N}	Asp 157
	d1	17.99	-	18.47	-	Hβ	His 156
	d2	20.07	272	20.07	280	Hδ1	
	e1	18.96	-	19.16	-	Hβ	
	e2	21.8	304	22.02	307	Hδ1	
	x1	13.43	187	13.66	197	H^{N}	
	x2	14.83	225	14.95	221	H^{N}	

ol: overlap with c1

***Table S4.2**: Chemical shift in ppm for the resonances in the ^1H spectra region of 22 to 55 ppm belonging to the NI state of SLAC-T1D and SLAC-wt at 298 K.*

Resonance	SLAC-T1D	SLAC-wt
3	21.94	Overlap with resonance e2
4	23.42	23.33
5	24.70	23.91
6	26.52	25.96
7	29.27	28.52
8	31.48	30.14
9	34.99	33.67
11	36.95	35.66
12	39.21	37.96
13	41.86	40.72
14/15	43.14	42.83
16	44.07	44.43
17	49.21	49.21
18	52.77	52.77

***Table S4.3**: Hyperfine coupling constants (A) obtained from fitting the temperature dependencies of the chemical shifts to equation 1.5 for SLAC-wt and SLAC-T1D/Q291E. The error values are ~ 5% from the fit.*

SLAC-wt		SLAC-T1D/Q291E	
Resonance	*A* (MHz)	Resonance	*A* (MHz)
a1	0.7	d0/x2	0.9
x1	0.8	c1	1.0
u1	2.1	b2	1.6
b1	2.2	d2/c2	1.9
d0	1.0	e2	2.0
x2	1.1		
d1	2.5		
c1	1.1		
a2	1.5		
e1	2.6		
b2	1.5		
d2	1.7		
c2	1.8		
e2	2.0		

***Table S4.4**: Chemical shift at different temperatures for the resonances in the RO state of SLAC-wt.*

	Temperature (K)					
	278	283	288	293	298	303
Resonance	Chemical shift (ppm)					
e2	20.81	21.08	21.44	21.51	21.88	21.89
c2	19.93	20.17	20.40	20.62	20.84	21.01
d2	19.13	19.38	19.63	19.87	20.09	20.32
b2	18.06	18.30	18.52	18.75	18.91	19.14
d1	16.80	17.06	17.35	17.70	17.99	18.24
c1	16.00	16.14	16.32	16.46	16.64	16.81
u1	14.70	15.00	15.30	15.63	15.83	16.23
x2	ol	ol	ol	14.90	15.15	15.26
d0	14.08	14.25	14.40	14.51	14.67	14.81
x1	12.97	13.14	13.23	13.29	13.38	13.63
a1	12.50	12.55	12.58	12.65	12.76	12.86
b1	ol	ol	15.63	15.95	16.25	16.60
a2	ol	ol	18.65	18.90	19.13	19.34
e1	ol	ol	18.27	18.70	18.94	19.37

ol: Chemical shift could not be determined due to resonance overlap

***Table S4.5**: Chemical shift at different temperatures for the resonances in the RO state of SLAC-T1D/Q291E.*

	Temperature (K)					
	278	283	288	293	298	303
Resonance	Chemical shift (ppm)					
e2	21.057	21.219	21.408	21.662	21.927	22.213
d2/c2	19.897	20.115	20.153	20.438	20.673	20.884
b2	18.112	18.347	18.423	18.717	18.928	19.172
c1	14.984	15.234	15.275	15.578	15.758	15.952
d0/x2	14.438	14.651	14.628	14.882	15.015	15.183

4.5 References

1. Mano, N., V. Soukharev, and A. Heller. 2006. A Laccase-Wiring Redox Hydrogel for Efficient Catalysis of O $_2$ Electroreduction. *J. Phys. Chem. B*. 110:11180–11187.
2. Solomon, E.I., D.E. Heppner, E.M. Johnston, J.W. Ginsbach, J. Cirera, M. Qayyum, M.T. Kieber-Emmons, C.H. Kjaergaard, R.G. Hadt, and L. Tian. 2014. Copper Active Sites in Biology. *Chemical Reviews*. 114:3659–3853.
3. Solomon, E.I., A.J. Augustine, and J. Yoon. 2008. O2 Reduction to H2O by the multicopper oxidases. *Dalton Trans*. 3921–3932.
4. Gupta, A., I. Nederlof, S. Sottini, A.W.J.W. Tepper, E.J.J. Groenen, E.A.J. Thomassen, and G.W. Canters. 2012. Involvement of Tyr108 in the Enzyme Mechanism of the Small Laccase from Streptomyces coelicolor. *Journal of the American Chemical Society*. 134:18213–18216.
5. Tian, S., S.M. Jones, and E.I. Solomon. 2020. Role of a Tyrosine Radical in Human Ceruloplasmin Catalysis. *ACS Cent. Sci.*
6. Machczynski, M.C., and J.T. Babicz. 2016. Correlating the structures and activities of the resting oxidized and native intermediate states of a small laccase by paramagnetic NMR. *Journal of Inorganic Biochemistry*. 159:62–69.
7. Dasgupta, R., K.B.S.S. Gupta, H.J.M. de Groot, and M. Ubbink. 2020. Towards resolving the complex paramagnetic NMR spectrum of small laccase: Assignments of resonances to residue specific nuclei. *Magnetic Resonance Discussions*. 1–13.
8. Dasgupta, R., K.B.S.S. Gupta, F. Nami, H.J.M. de Groot, G.W. Canters, E.J.J. Groenen, and M. Ubbink. 2020. Chemical Exchange at the Trinuclear Copper Center of Small Laccase from Streptomyces coelicolor. *Biophysical Journal*. 119:9–14.
9. Bubacco, L., J. Salgado, A.W.J.W. Tepper, E. Vijgenboom, and G.W. Canters. 1999. ^{1}H NMR spectroscopy of the binuclear Cu(II) active site of Streptomyces antibioticus tyrosinase. *FEBS Letters*. 442:215–220.
10. Murthy, N.N., K.D. Karlin, I. Bertini, and C. Luchinat. 1997. NMR and Electronic Relaxation in Paramagnetic Dicopper(II) Compounds. *J. Am. Chem. Soc.* 119:2156–2162.
11. Maekawa, M., S. Kitagawa, M. Munakata, and H. Masuda. 1989. Nuclear magnetic resonance studies of dicopper(II) complexes with binucleating ligands containing imidazoles. *Inorg. Chem*. 28:1904–1909.
12. Bertini, I., C. Luchinat, G. Parigi, and E. Ravera. 2017. NMR of paramagnetic molecules: applications to metallobiomolecules and models. Second edition. Amsterdam: Elsevier.
13. Kalverda, A.P., J. Salgado, C. Dennison, and G.W. Canters. 1996. Analysis of the paramagnetic copper(II) site of amicyanin by 1H NMR spectroscopy. *Biochemistry*. 35:3085–3092.
14. Canters, G.W., H.A.O. Hill, N.A. Kitchen, and E.T. Adman. 1984. The assignment of the 1H nuclear magnetic resonance spectrum of azurin. An investigation of the 1H NMR spectrum of the blue copper protein, azurin, from Pseudomonas aeruginosa, with reference to the previously determined crystal structure. *European Journal of Biochemistry*. 138:141–152.
15. Bertini, I., S. Ciurli, A. Dikiy, R. Gasanov, C. Luchinat, G. Martini, and N. Safarov. 1999. High-Field NMR Studies of Oxidized Blue Copper Proteins: The Case of Spinach Plastocyanin. *Journal of the American Chemical Society*. 121:2037–2046.
16. Quintanar, L., J. Yoon, C.P. Aznar, A.E. Palmer, K.K. Andersson, R.D. Britt, and E.I. Solomon. 2005. Spectroscopic and Electronic Structure Studies of the Trinuclear Cu Cluster Active Site of the Multicopper Oxidase Laccase: Nature of Its Coordination Unsaturation. *J. Am. Chem. Soc.* 127:13832–13845.
17. Bertini, I., C. Luchinat, L. Messori, and M. Vasak. 1989. Proton NMR spectra of the Co4S11 cluster in metallothioneins: a theoretical model. *J. Am. Chem. Soc.* 111:7300–7303.
18. Banci, L., I. Bertini, and C. Luchinat. 1990. The 1H NMR parameters of magnetically coupled dimers—The Fe2S2 proteins as an example. In: Bioinorganic Chemistry. Berlin, Heidelberg: Springer. pp. 113–136.
19. Patt, S.L., and B.D. Sykes. 1972. Water Eliminated Fourier Transform NMR Spectroscopy. *J. Chem. Phys.* 56:3182–3184.
20. Bertini, I., C. Luchinat, G. Parigi, and R. Pierattelli. 2005. NMR Spectroscopy of Paramagnetic Metalloproteins. *ChemBioChem*. 6:1536–1549.

21. Skálová, T., J. Dohnálek, L.H. Østergaard, P.R. Østergaard, P. Kolenko, J. Dušková, A. Štěpánková, and J. Hašek. 2009. The Structure of the Small Laccase from Streptomyces coelicolor Reveals a Link between Laccases and Nitrite Reductases. *Journal of Molecular Biology*. 385:1165–1178.
22. Pettersen, E.F., T.D. Goddard, C.C. Huang, G.S. Couch, D.M. Greenblatt, E.C. Meng, and T.E. Ferrin. 2004. UCSF Chimera—A visualization system for exploratory research and analysis. *Journal of Computational Chemistry*. 25:1605–1612.
23. Banci, L., I. Bertini, C. Luchinat, R. Pierattelli, N.V. Shokhirev, and F.A. Walker. 1998. Analysis of the Temperature Dependence of the 1H and 13C Isotropic Shifts of Horse Heart Ferricytochrome c: Explanation of Curie and Anti-Curie Temperature Dependence and Nonlinear Pseudocontact Shifts in a Common Two-Level Framework. *J. Am. Chem. Soc.* 120:8472–8479.
24. Bertini, I., C. Luchinat, and G. Parigi. 2002. Magnetic susceptibility in paramagnetic NMR. *Progress in Nuclear Magnetic Resonance Spectroscopy*. 40:249–273.
25. Gabdulkhakov, A., I. Kolyadenko, O. Kostareva, A. Mikhaylina, P. Oliveira, P. Tamagnini, A. Lisov, and S. Tishchenko. 2019. Investigations of Accessibility of T2/T3 Copper Center of Two-Domain Laccase from Streptomyces griseoflavus Ac-993. *International Journal of Molecular Sciences*. 20:3184.
26. Gibson, D.G., L. Young, R.-Y. Chuang, J.C. Venter, C.A. Hutchison, and H.O. Smith. 2009. Enzymatic assembly of DNA molecules up to several hundred kilobases. *Nature Methods*. 6:343–345.

Chapter 5

Electronic structure of the tri-nuclear copper center in the resting oxidized state for small laccase

5.1 Introduction

Laccases are multicopper oxidases that oxidize substrates and efficiently reduce oxygen to water.(1) They consist of two active sites, a type-1 (T1) copper site for oxidizing substrates and a tri-nuclear copper center (TNC) for the oxygen reduction reaction. The TNC comprises of two sites a type-3 (T3) site and a type-2 (T2) site. The T3 copper site is characterized by two coupled copper ions via a hydroxide ion and each of the Cu(II) ions are coordinated by three histidine ligands. The T2 site is characterized by a single Cu(II) ion which is coordinated by two histidine ligands and water/OH^- (Figure 1.4a). Using spectroscopic techniques coupled with quantum mechanical calculations the catalytic mechanism of the oxygen reduction reaction was described for an iron oxidizing laccase Fet3p from *Saccharomyces cerevisiae* (Figure 1.3).(2) Fet3p belongs to the class of three-domain laccase where the catalytic motif of the TNC consists of the three copper ions and its coordinated imidazolyl ligands (Figure 1.4a). All ligands are thought to remain protonated throughout the catalytic cycle, which puts a positive charge bias on the entire catalytic motif. When the reaction proceeds, negative charge is accumulated, shuttled between the copper ions and the ligands, and finally transferred to oxygen.

In the two-domain laccase, the catalytic motif also has a tyrosine residue near the T2 site. This tyrosine residue was reported to take part in the oxygen reduction reaction by forming a radical during the peroxide intermediate (PI) to native intermediate (NI) conversion or during the resting oxidized (RO) state to the fully reduced (FR) state (Figure 1.3).(3–5) Although the electronic structure of the TNC for different catalytic states is defined for the three-domain laccase, this information for the two-domain laccase including the tyrosine residue is not described.

5.2 Results and discussions

The RO state of the TNC of small laccase is modelled according to the procedure described by Solomon *et al*. using the crystal structure 6s0o (chain D and E, resolution 1.80 Å; small laccase from *S. griseoflavus*) including the Tyr109 residue near the T2 site (Figure 5.1).(6, 7) In this procedure, the structure is first optimized for high, unrestricted spin, and the actual spin density is modeled in a broken symmetry single point calculation where one of the spins is flipped to match the spin state of the catalytic motif.(6, 8) Different models of the RO state were studied based on the water derived T2 site ligand and orientation of the phenolic -OH group of tyrosine (for details see Supporting Information) (Figure 5.1).

In the models where the proton of the phenolic -OH group is directed towards the water/OH^- ligand of the T2 site (model B and D in Figure 5.1) the T2 copper ion is reduced to Cu^{1+} with a formation of a neutral tyrosine radical. In contrast, when the proton of the phenolic -OH group is directed away (model A and C in Figure 5.1) the T2 site copper remains oxidized as Cu^{2+} and the spin density distribution is similar to that reported by Solomon *et al.* (2005, 2001) (Figure 5.1).(6, 9) Some difference in the spin density distribution at the T2 site is observed between model A and C. In model A (Figure 5.1) the electron spin density is delocalized over a copper ion and its OH^- ligand while in model C most of the spin density is localized on the copper ion. The spin density distribution at the T3 site is essentially the same for all the models. In model A and C, the T2 Cu^{2+} ion is a three-coordinated site with a planar geometry. It has as an open coordination oriented towards the center of the cluster with a "$d_{x^2-y^2}$" ground state (Figure 5.2). The two T3 site copper ions are antiferromagnetically coupled with each having a four-coordination environment. The T3 copper ion has the "d_{xz}" ground state while the T3' site has the "$d_{x^2-y^2}$" ground state with an open coordination directed toward the center of the cluster (Figure 5.2). These observations are consistent with experimental evidence for the RO state and previous calculations.(6, 9) The X-band EPR spectrum of the T2 site has $g_{||} > g_{\perp} > 2.00$ with large parallel hyperfine splitting suggesting a "$d_{x^2-y^2}$" ground state. While, the splitting of the absorption band at 330 nm into two-bands in the circular dichroism spectrum suggest a μ-OH bridged two Cu^{2+} ions, the characteristic feature of the T3 site.(6, 9, 10) The spin density distribution for model B and D suggests that the orientation of the proton of the phenolic -OH group of the tyrosine towards the water/OH^- ligand of the T2 site spontaneously leads to radical formation (Figure 5.1). In model A and C, the radical formation is not observed and this can be attributed to the distant orientation of the proton of the phenolic -OH group of the tyrosine (Figure 5.1). The energy difference between the models shows that the tyrosine radical state for models B and D is the excited state and the non-radical state in models A and C is the ground state that is relevant to describe the small laccase (Table 5.1).

5.3 Conclusion

In conclusion, the spin density distribution and geometric properties of model A and C of the RO state for small laccase is well in line with the previous report for laccase and can be considered the relevant state for the resting oxidized state of the protein under investigation, small laccase.(6) In contrast, the orientation of the phenolic -OH group from the Tyr109 residue towards the T2 site forms a tyrosine radical at higher energy. The radical formation might be an excited state that is inaccessible in the RO state. This is corroborated by experimental observations where

the radical formation is observed only after the reduction of the T3 site copper ions and the T1 site is unable to provide the next electron for the formation of a fully reduced TNC.(3, 5) This study shows that the RO state from small laccase with the tyrosine residue could be modelled and is similar to previous reports.(6) Using similar strategy other states (PI and NI) can also be modelled. It was reported that using a combination of DFT calculations and solid-state NMR spectroscopy, the resonance assignment and geometry around a single copper center can be determined with picometer resolution.(11) A similar approach can be used to assign the NMR signals reported in Chapters 2 to 4 for the RO and the NI states of small laccase. The current calculations can be used in achieving this goal.

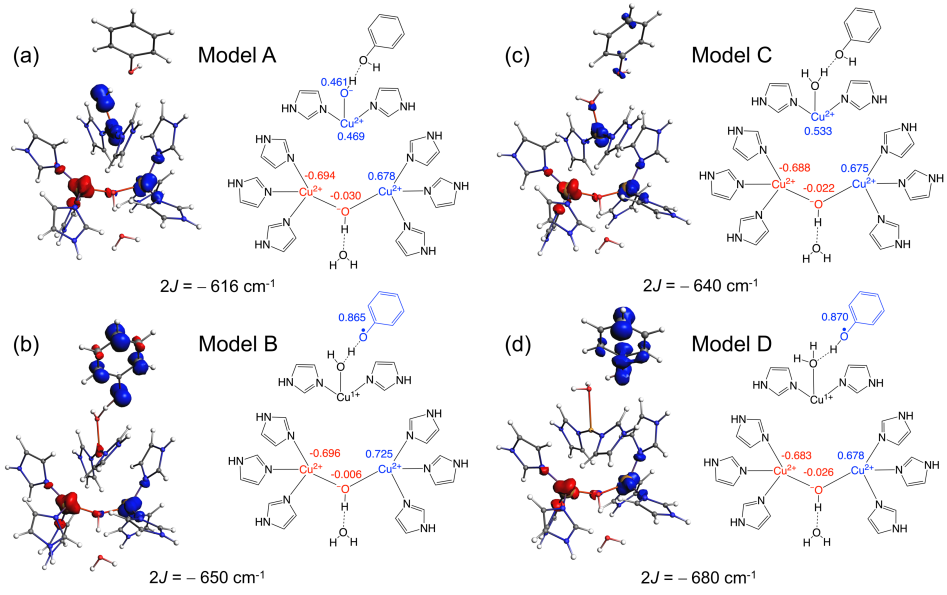


Figure 5.1*. Models of the resting oxidized state based on the water/OH⁻ ligands of the T2 site and the orientation of the phenolic OH group representing the tyrosine 109 residue (from the crystal structure 6s0o, resolution 1.80 Å, organism S. greseoflavus) near the T2 site. Each panel shows the electron spin density distribution of the TNC, the schematic representation of the model with the Mulliken spin density on the three copper ions, OH⁻ ligand of the T2 site (panel a) and the phenolic group (panel b and d) and the model names. The singlet triplet energy gap (2J) is indicated below each panel. Spin densities are represented as isosurfaces. Red denotes negative phase of the spin density while blue denotes positive phase.*

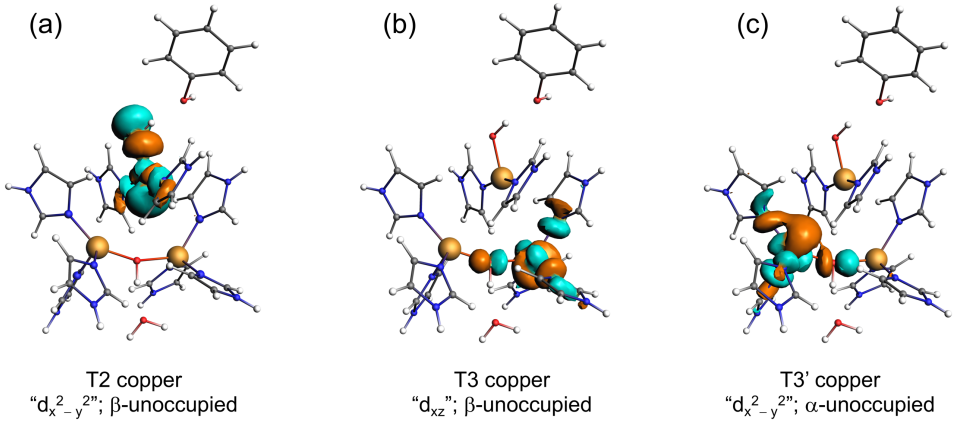


Figure 5.2. *Isosurface of α- and β-LUMOs based on the T2/T3' "$d_{x^2-y^2}$" and T3 "d_{xy}" respectively. The isosurfaces were obtained from the broken-symmetry state calculation.(6, 8)*

Table 5.1. *Energy of the high spin and broken symmetry spin state of the models of the RO state in Figure 5.1. The singlet-triplet energy gap (2J) is also shown.*

	Energy in kcal/mol			
	Model A	Model B	Model C	Model D
High Spin (HS)	-14628.220	-14615.771	-14553.125	-14551.558
Broken symmetry (BS)	-14629.100	-14616.700	-14554.040	-14552.530
Singlet-triplet gap (2*J*) 2(BS-HS)	-1.760 (-616 cm^{-1})	-1.858 (-650 cm^{-1})	-1.830 (-640 cm^{-1})	-1.944 (-680 cm^{-1})

5.4 Supporting Information

Model building

The models for the RO state as shown in Figure 5.1 were built using the crystal structure 6s0o chain D and E (resolution of 1.80 Å) (7). The histidine ligands were replaced with imidazolyl and the Tyr109 (Figure 5.3) was replaced with a phenol to mimic only the side chain of these residues. The water/OH^- ligand of the T2 site and the bridging OH^- between the T3 copper ions were included. An additional conserved water molecule with a strong hydrogen bond with the bridging OH^- was also included. The protons were modelled using the "AddH" algorithm as implemented in the program UCSF Chimera (12). The protons at the water/OH^- ligand of the T2 site and the phenol were arranged as follows: model A: T2 site ligand of OH^- with the phenolic -OH group directed away, model B: reorientation of T2 site OH^- ligand in model A such that the phenolic -OH group can be directed towards it, model C: T2 site ligand of H_2O and the phenolic -OH group directed away from it and model D: reorientation of the T2 site water ligand in model C such that the phenolic -OH can be directed towards it (Figure 5.1). These models were based on the hydrogen bonding pattern of the T2 site as shown in Figure 5.3.

DFT calculation

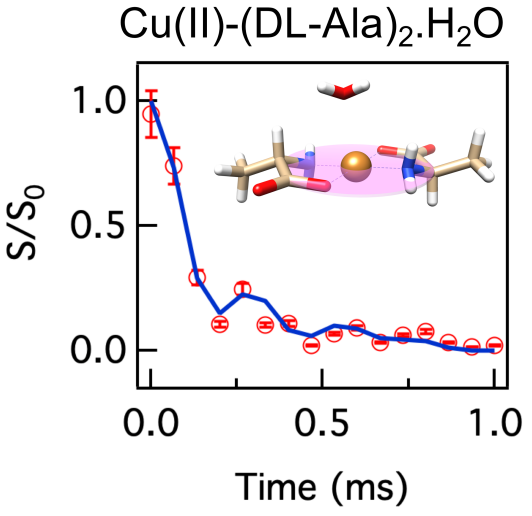
DFT calculations were done using Amsterdam density functional suite (13). During geometry optimization constraints were applied to reflect the crystal structure geometry of the TNC (14). The hydrogen atom replacing the side chain of the histidine ligands and the tyrosine were fixed. The dihedral angles defined by N-T3-T3'-N (T3 and T3' coppers are defined in Figure 5.1 and 5.3) were fixed to keep the eclipsed conformation. The angle of the oxygen atom from the water/OH^- ligand of the T2 copper relative to the histidine rings was fixed. This would prevent its artificial binding to the T3 histidine ligand. Solvent effects reflecting the protein dielectric environment was considered using conductor-like screening model as implemented in ADF suite with a dielectric constant of 4.0 (14, 15). Hybrid B3LYP (20% Hartree-Fock exchange) functional was used for all the calculations (16). A Slater-type basis set was used for all calculations (17). For geometry optimization double-ζ basis set was used for copper and nitrogen atoms while single-ζ basis set for the rest. For single-point broken-symmetry calculations the triple-ζ basis set was used for coppers and nitrogen atoms with a double-ζ basis for the rest. Broken-symmetry calculations were done by flipping the spin on the T3 copper ion (Figure 5.1).

5.5 References

1. Mano, N., and A. de Poulpiquet. 2017. O_2 Reduction in Enzymatic Biofuel Cells. *Chem. Rev.*
2. Palmer, A.E., L. Quintanar, S. Severance, T.-P. Wang, D.J. Kosman, and E.I. Solomon. 2002. Spectroscopic Characterization and O2 Reactivity of the Trinuclear Cu Cluster of Mutants of the Multicopper Oxidase Fet3p. *Biochemistry*. 41:6438–6448.
3. Gupta, A., I. Nederlof, S. Sottini, A.W.J.W. Tepper, E.J.J. Groenen, E.A.J. Thomassen, and G.W. Canters. 2012. Involvement of Tyr108 in the Enzyme Mechanism of the Small Laccase from *Streptomyces coelicolor*. *Journal of the American Chemical Society*. 134:18213–18216.
4. Tepper, A.W.J.W., S. Milikisyants, S. Sottini, E. Vijgenboom, E.J.J. Groenen, and G.W. Canters. 2009. Identification of a Radical Intermediate in the Enzymatic Reduction of Oxygen by a Small Laccase. *J. Am. Chem. Soc.* 131:11680–11682.
5. Tian, S., S.M. Jones, and E.I. Solomon. 2020. Role of a Tyrosine Radical in Human Ceruloplasmin Catalysis. *ACS Cent. Sci.*
6. Quintanar, L., J. Yoon, C.P. Aznar, A.E. Palmer, K.K. Andersson, R.D. Britt, and E.I. Solomon. 2005. Spectroscopic and Electronic Structure Studies of the Trinuclear Cu Cluster Active Site of the Multicopper Oxidase Laccase: Nature of Its Coordination Unsaturation. *J. Am. Chem. Soc.* 127:13832–13845.
7. Gabdulkhakov, A., I. Kolyadenko, O. Kostareva, A. Mikhaylina, P. Oliveira, P. Tamagnini, A. Lisov, and S. Tishchenko. 2019. Investigations of Accessibility of T2/T3 Copper Center of Two-Domain Laccase from *Streptomyces griseoflavus* Ac-993. *International Journal of Molecular Sciences*. 20:3184.
8. Onofrio, N., and J.-M. Mouesca. 2010. Valence Bond/Broken Symmetry Analysis of the Exchange Coupling Constant in Copper(II) Dimers. Ferromagnetic Contribution Exalted through Combined Ligand Topology and (Singlet) Covalent-Ionic Mixing. *J. Phys. Chem. A*. 114:6149–6156.
9. Solomon, E.I., P. Chen, M. Metz, S.-K. Lee, and A.E. Palmer. 2001. Oxygen Binding, Activation, and Reduction to Water by Copper Proteins. *Angewandte Chemie International Edition*. 40:4570–4590.
10. Solomon, E.I., U.M. Sundaram, and T.E. Machonkin. 1996. Multicopper Oxidases and Oxygenases. *Chem. Rev.* 96:2563–2606.
11. Bertarello, A., L. Benda, K.J. Sanders, A.J. Pell, M.J. Knight, V. Pelmenschikov, L. Gonnelli, I.C. Felli, M. Kaupp, L. Emsley, R. Pierattelli, and G. Pintacuda. 2020. Picometer Resolution Structure of the Coordination Sphere in the Metal-Binding Site in a Metalloprotein by NMR. *J. Am. Chem. Soc.* 142:16757–16765.
12. Pettersen, E.F., T.D. Goddard, C.C. Huang, G.S. Couch, D.M. Greenblatt, E.C. Meng, and T.E. Ferrin. 2004. UCSF Chimera—A visualization system for exploratory research and analysis. *Journal of Computational Chemistry*. 25:1605–1612.
13. Velde, G. te, F.M. Bickelhaupt, E.J. Baerends, C.F. Guerra, S.J.A. van Gisbergen, J.G. Snijders, and T. Ziegler. 2001. Chemistry with ADF. *Journal of Computational Chemistry*. 22:931–967.
14. Yoon, J., and E.I. Solomon. 2007. Electronic Structure of the Peroxy Intermediate and Its Correlation to the Native Intermediate in the Multicopper Oxidases: Insights into the Reductive Cleavage of the O−O Bond. *J. Am. Chem. Soc.* 129:13127–13136.
15. Pye, C.C., and T. Ziegler. 1999. An implementation of the conductor-like screening model of solvation within the Amsterdam density functional package. *Theoretical Chemistry Accounts: Theory, Computation, and Modeling (Theoretica Chimica Acta)*. 101:396–408.
16. Stephens, P.J., F.J. Devlin, C.F. Chabalowski, and M.J. Frisch. 1994. Ab Initio Calculation of Vibrational Absorption and Circular Dichroism Spectra Using Density Functional Force Fields. *J. Phys. Chem.* 98:11623–11627.
17. Lenthe, E.V., and E.J. Baerends. 2003. Optimized Slater-type basis sets for the elements 1–118. *Journal of Computational Chemistry*. 24:1142–1156.

Chapter 6

Dipolar dephasing for structure determination in a paramagnetic environment



This chapter is published as:
Dasgupta, R., K.B.S.S. Gupta, D. Elam, M. Ubbink, and H.J.M. de Groot. 2021. Dipolar dephasing for structure determination in a paramagnetic environment. *Solid State Nuclear Magnetic Resonance*. 113:101728.
DOI: http://doi.org/10.1016/j.ssnmr.2021.101728

We demonstrate the efficacy of the REDOR-type sequences in determining dipolar coupling strength in a paramagnetic environment. Utilizing paramagnetic effects of enhanced relaxation rates and rapid fluctuations in Cu(II)-(DL-Ala)$_2$.H_2O, the dipolar coupling strength for the methyl C-H that is 4.20 Å away from the Cu^{2+} ion, was estimated to be ~ 8.8 ± 0.6 kHz. This coupling is scaled by a factor of ~ 0.3 in comparison to the rigid limit value of ~ 32 kHz, in line with partial averaging of the dipolar interaction by rotational motion of the methyl group. Limited variation in the scaling factor of the dipolar coupling strength at different temperatures is observed. The C-H internuclear distance derived from dipolar coupling strength is similar to the crystal structure. The errors observed in the REDOR-type experiments are similar to those reported for diamagnetic systems. Increase in resolution due to the Fermi contact shifts, coupled with MAS frequencies of 30–35 kHz allowed to estimate the hyperfine coupling strengths for protons and carbons from the temperature dependence of the chemical shift and obtain a high resolution ^1H–^1H spin diffusion spectrum. This study shows the utility of REDOR-type sequences in obtaining reliable structural and dynamical information from a paramagnetic complex. We believe that this can help in studying the active site of metalloproteins which are paramagnetic in nature at high resolution.

6.1 Introduction

Paramagnetic solid-state NMR has undergone a revolution in the past decade due to the development of high spinning frequency probes and tailored pulse sequences. Studying the ligands that directly coordinate the paramagnetic metal ions with NMR can provide insight into the structure and dynamics of the system.(1–4) Among the various interactions, dipolar interactions are attractive for characterizing fast cooperative dynamics that can be measured using rotational-echo double resonance (REDOR) type solid state NMR experiments including shifted-REDOR for probing anisotropic motions.(5–7)

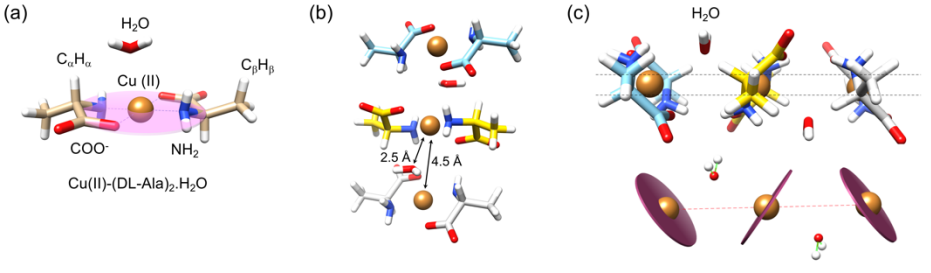


***Figure 6.1**. Cu(II)-(DL-Ala)$_2$.H$_2$O crystal structure (cif:1153761).(8) (a) Monomer depicting the plane of coordination and the respective proton and carbon orientations (b) Trimeric representation of chain with distance between copper atoms and between copper and oxygen of water and (c) Coordination plane of copper and position of water molecule.*

In this study we show that rapid paramagnetic fluctuations favorably affect REDOR and shifted REDOR experiments therefore, those can be performed with high sensitivity and resolution. We find that internuclear dipolar couplings can be determined with high accuracy that is comparable to what has been achieved for diamagnetic systems. We have selected Cu(II)-(DL-Ala)$_2$.H$_2$O (Figure 6.1) as a model system to test the utility of the REDOR type sequences and to probe the C–H dipolar coupling of the methyl group in the alanine ligand, which is directly coordinating the paramagnetic metal center.(8–11) Recently, well-resolved heteronuclear dipolar correlation spectroscopy was reported for Cu(II)-(DL-Ala)$_2$.H$_2$O.(10, 12–14) The possibility to sustain internuclear dipolar transfer in the immediate vicinity of paramagnetic ions can be attributed to rapid paramagnetic fluctuations that average the anisotropic and traceless electron-nuclear dipolar interactions while leaving the isotropic contact shifts unaffected. Here, the J-coupling between the copper ions determines the fluctuation frequencies for averaging dipolar couplings, which are traceless without isotropic component and is intrinsic to a one-dimensional chain. This results in the motional narrowing from spin waves running along the chain.(15) This opens up a window of opportunity, since essential advantages of paramagnetism, such as rapid acquisition and increased spectral dispersion can be combined with the power of dipolar correlation spectroscopy for resolving static or dynamic structure quantitatively. To demonstrate this, we implement a REDOR method for Cu(II)-(DL-Ala)$_2$.H$_2$O by adapting the REDOR refocusing period to the fast rotation needed for signal detection in paramagnetic systems with their enhanced relaxation that limits the acquisition time. The Cu(II)-(DL-Ala)$_2$.H$_2$O form 1-dimensional chains in which the Cu^{2+} ions are weakly coupled.(11) The antiferromagnetic coupling $2J = -2.21$ cm^{-1} translates into a characteristic frequency of ~ 70 GHz for the electronic spin fluctuations.(11) The properties of enhanced relaxation and rapid averaging of electron-nuclear dipolar interactions by paramagnetic fluctuations that are much faster than the frequency scale of the heteronuclear dipolar coupling of ~ 10 kHz or less, allow to perform heteronuclear dipolar recoupling experiments with fast MAS in a very short time, much shorter than for diamagnetic species. In addition, we show how ^{1}H□^{1}H spin diffusion spectra and the temperature dependence of proton and carbon shifts from 1D Hahn-echo experiments can help to collect structural information from paramagnetic systems with ultra-fast MAS.

6.2 Results and discussions

NMR characterization of Cu(II)-(DL-Ala)$_2$.H$_2$O

There are several advantages when working with Cu(II) paramagnetic systems. Since Cu(II) has small susceptibility the Fermi-contact interaction is stronger than the paramagnetic relaxation enhancement (PRE).(16) This results in a better resolution because of the increase in the spectral dispersion without adversely affecting the linewidth. Additionally, reduction of experimental time due to fast longitudinal relaxation compared to diamagnetic systems can be achieved. In contrast, with other metal ions such as Tb(III) the susceptibility anisotropy is large and may lead to resonances broadened beyond detection due to increase in PRE-effects.(16) Figure 6.2 shows the 1D spectra of ^{1}H and ^{13}C at different spinning frequencies and magnetic fields. The resolution is enhanced by the paramagnetic shifts at very fast MAS (> 20 kHz).(12–14, 17–19)

The 1D proton rotor-synchronized Hahn-echo spectra (Figure 6.2a and b) show three prominent resonances attributed to CH_α at 8 ppm and C**H**$_3$1 at 32 ppm and C**H**$_3$2 at 21 ppm. We observed that the intensity of C**H**$_3$1 is 4 times that of H_α and C**H**$_3$2, while H_α and C**H**$_3$2 show similar intensities. The carbon spectrum shows three prominent resonances for C_α1 at -280 ppm, *C*O at -200 ppm and C_β1 at 180 ppm and two minor resonances for C_α2 at -258 ppm and C_β2 at 88 ppm, (Figure 6.2c, 6.2d and Table S6.1).(10, 13, 19) The two components were attributed to two orientations of the methyl group as a consequence of crystal packing, where the major component (C**H**$_3$1/C_β1) is closer to the copper atom while the minor component (C**H**$_3$2/C_β2) is away.(8, 20) The proton signals from the NH_2 group (data not shown) were reported to be at -132.7 and -159.5 ppm.(10) The protons from the water molecule are generally broadened beyond detection due to fast exchange dynamics.(10, 19) The methyl group of the major component was reported to be undergoing fast rotation which results in a single resonance for the three methyl protons (Figure 6.2a and b).(10)

A dipolar-INEPT experiment was performed to check the quality of the sample and the efficiency of polarization transfer via dipolar interactions, which was previously shown to be superior to cross polarization based transfer for paramagnetic systems.(13, 21) It shows the similar spectrum (Figure 6.2d) as reported earlier albeit with better resolution and S/N allowing to identify the splitting of the methyl group response that arises due to crystal packing effects.(8, 13, 20)

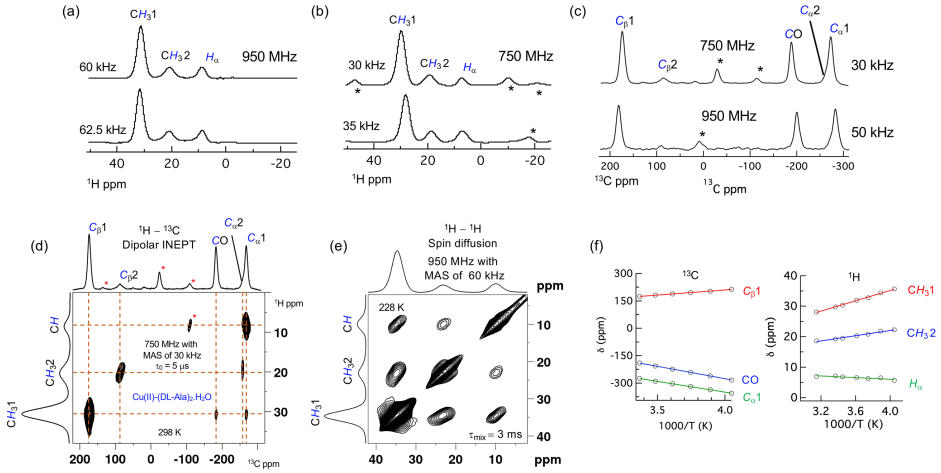


Figure 6.2. *(a) 1D ^{1}H rotor synchronized Hahn-echo spectra at MAS frequencies of 60 and 62.5 kHz in an external magnetic field of 950 MHz; (b) 1D ^{1}H rotor synchronized Hahn-echo spectra at MAS frequencies of 30 and 35 kHz in an external magnetic field of 750 MHz; (c) 1D ^{13}C rotor synchronized Hahn-echo spectra at MAS frequencies of 30 and 50 kHz in an external magnetic field of 750 and 950 MHz respectively; (d) The 2D ^{1}H-^{13}C dipolar-INEPT spectra at a MAS frequency of 30 kHz in an external magnetic field of 750 MHz with a transfer delay τ_0 of 5 μs at 298 K; (e) 2D ^{1}H-^{1}H spin diffusion at a MAS frequency of 60 kHz in an external magnetic field of 950 MHz with a mixing time τ_{mix} of 5 ms at 228 K; (f) Temperature dependence of the chemical shift for carbon and protons where* C**H**$_3$1 *and* C_β *are in red,* C**H**$_3$2 *and carbonyl carbon* CO *are in blue and* H_α *and* C_α *are in green. Solid lines are the fit using equation S6.9. The spinning side bands in the upper panels are marked with asterisks. The assignments in panel (a) to (e) of ^{1}H and ^{13}C responses are shown in italics and blue color.*

The 2D ^{1}H–^{1}H spin diffusion spectra acquired at 950 MHz with a MAS frequency of 60 kHz (Figure 6.2e and S6.3), show that a high resolution homonuclear 2D spectra can be obtained under paramagnetic conditions with modification of the pulse sequence to consider the paramagnetic effects of increased relaxation and rapid fluctuations. Similar observations were reported for copper cyclam complexes.(21)

The temperature dependence of the chemical shift shows strong Curie behavior for CO, C_α1, C_β1, C**H**$_3$1 and C**H**$_3$2 while weak anti-Curie behavior is observed for H_α (Figure 6.2f and Figure S6.2a). The hyperfine coupling strengths are summarized in table 1, obtained after fitting the data with equation 9 (Figure 6.2f).(22) It is interesting to observe that, although the H_α is close to the copper, the hyperfine coupling constant and hence the spin density on it is less than for H_β. This was also observed in DFT calculations for Cu(II)-(DL-Ala)$_2$.H$_2$O showing very little spin density localized on the H_α atom.(22, 23) The sign of the hyperfine coupling strength provides

the spin polarization of the electron on the nucleus with respect to the external magnetic field. It was observed to be parallel for $C_\beta 1$, $C\mathbf{H}_3 1$ and $C\mathbf{H}_3 2$ and anti-parallel for $C_\alpha 1$, CO and H_α (Table 6.1 and Figure 6.2f). These observations are in line with the calculations performed on copper alanine complexes and previously reported data.(22) The estimated δ_{dia} from the fit of the temperature dependencies of the chemical shift (Figure 6.2f) is summarized in table 6.1. They differ from the expected diamagnetic chemical shift of DL-alanine (Table S6.3). This difference can be attributed to the differences in crystal packing of Cu(II)-(DL-Ala)$_2$.H_2O and DL-alanine (Figure S6.6). The NMR chemical shift tensor for small molecules in solid state NMR differs significantly between different crystal forms due to changes in hydrogen bonding, stacking, ring current, C–H···π interactions etc.(24) DFT calculations of different crystal forms of purine derivatives show that the change in the diamagnetic chemical shift can be as high as 6.5 ppm, 20 ppm and 55 ppm for proton, carbon and nitrogen respectively.(24)

***Table 6.1**. Hyperfine coupling strength (A) and the estimated diamagnetic chemical shift from temperature dependencies of the resonances for carbon and protons.*

Nuclei	*A* (MHz)	δ_{dia} (ppm)
$C_\alpha 1$	-3.7 ± 0.3	120 ± 4
$C_\beta 1$	1.8 ± 0.9	-12 ± 1
CO	-4.3 ± 0.4	265 ± 5
H_α	-0.2 ± 0.04	11.0 ± 1.0
$C\mathbf{H}_3 2$*	0.5 ± 0.03	5.0 ± 0.9
$C\mathbf{H}_3 1$*	1.0 ± 0.03	1.5 ± 0.8

** The protons in question are indicated in bold.*

The full width at half of the maximum (FWHM) of the resonances decreases with increasing temperature (Figure S6.2b and S6.2c). Most likely, an increase in the electronic relaxation rate with temperature reduces the paramagnetic relaxation enhancement.

Dipolar coupling strength estimation

Dipolar coupling measurements can provide insight into the dynamics of the molecule.(5, 25) Here, we have employed REDOR (Figure S6.4c) and shifted-REDOR (Figure S6.4d) to measure the dipolar coupling between ^1H and ^{13}C of the methyl group in Cu(II)-(DL-Ala)$_2$.H_2O.(5, 6) The choice of these pulse sequences was based on their robustness for amplitude mis-setting, inhomogeneities in the radiofrequency field, carrier offset and CSA.(5) The methyl group was used as a probe because of the

presence of intrinsic methyl rotation that partially averages the dipolar coupling and its higher S/N ratio compared to that of other protons (Figure 6.2a and b).

Figure 6.3a shows the $^{1}H–^{13}C$ REDOR curves of the C-H in C**H**$_3$1 group at 277 K, 287 K and 297 K obtained at a MAS frequency of 30 kHz. The dipolar coupling strengths estimated after the fitting are 8.6 kHz, 10.0 kHz and 9.2 kHz respectively (Table 6.2 and Figure 6.3b). These values correspond with a scaling factor of ~ 0.3 (Table 6.2) relative to the rigid limit value of ~ 32 kHz, consistent with previously reported data for alanine in the diamagnetic crystalline state and similar to the theoretical scaling factor of 0.333.(26) The accuracy of the paramagnetic measurement is similar to that reported for the diamagnetic systems.(5, 6)

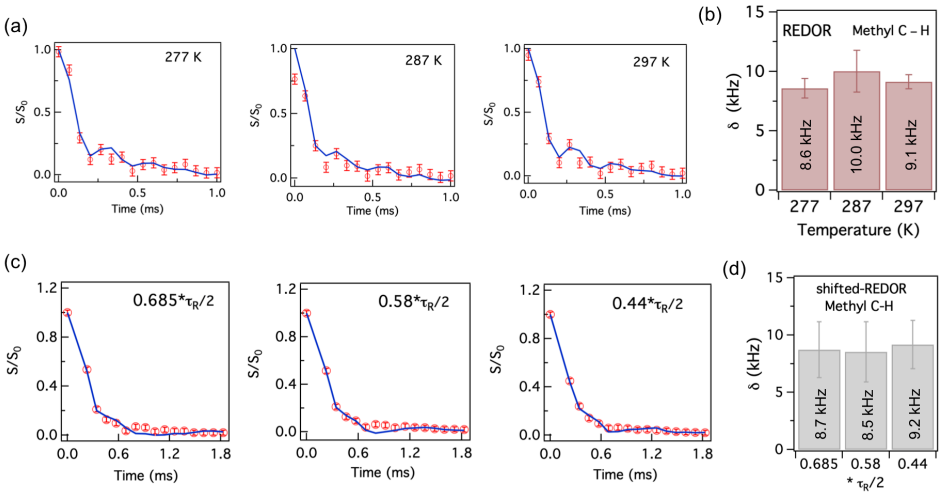


Figure 6.3. *(a) REDOR curve for methyl C-H (*C_β1 *and* C**H**$_3$1*) in Cu(II)-(DL-Ala)$_2$.H$_2$O at 277 K, 287 K and 297 K, the solid lines represent the fit; (b) The dipolar coupling strength estimated from fitting the REDOR curve for the methyl C-H (*C_β1 *and* C**H**$_3$1*); (c) Shifted-REDOR curves at a MAS frequency of 30 kHz with different shift of the π pulse from ideal $\tau_R/2$ (16.67 μs). The solid blue lines are fit with asymmetric parameter η value of 0.1; (d) Dipolar coupling strength estimated from the shifted-REDOR curve fit of methyl C-H (*C_β1 *and* C**H**$_3$1*).*

The corresponding internuclear $^{1}H–^{13}C$ (C_β1 and C***H***$_3$1) distances derived after dividing the dipolar coupling strength with the scaling factor is ~ 1.0 Å (Table 6.2) which is very similar to the crystal structure (1.0 Å).(8, 23) This demonstrates the efficacy of the REDOR sequence in obtaining reliable distance information in a paramagnetic system. It is noteworthy that although the paramagnetic shift is temperature dependent the dipolar coupling strength is preserved. This property can be explored to characterize the dipolar coupling strength between the nuclei in the

vicinity of the metal at the active site of the paramagnetic metalloproteins and consequently get insight into the dynamics.

***Table 6.2**. Dipolar coupling strength between C-H (*$C_\beta 1$ *and* $CH_3 1$*) at different temperatures using REDOR with a MAS frequency of 30 kHz.*

Temp (K)	δ kHz	Scaling factor	Methyl C-H ($C_\beta 1$ and $CH_3 1$) distance (Å)
277	8.6 ± 0.8	0.29 ± 0.03	1.1 ± 0.1
287	10.0 ± 1.7	0.34 ± 0.06	1.0 ± 0.2
297	9.1 ± 0.6	0.32 ± 0.02	1.0 ± 0.1

It was recently reported that using a variant of REDOR where the π pulses are shifted from its original position, known as shifted-REDOR (Figure S6.4d), is able to identify anisotropic motions present in the protein via the asymmetry parameter η easily by scaling down the oscillation.(5, 6) We investigated the dephasing behavior in the presence of the paramagnetic metal center at a spinning frequency of 30 kHz and at 297 K with the π pulse shift (τ_S) of 0.685 or 0.58 or 0.44 times $\tau_R/2$ (Figure 6.3c). The dipolar coupling strength between the methyl C-H nuclei does not change with varying τ_s and it matches with the values obtained from REDOR (Table 6.3 and 6.4). The derived internuclear distance is ~ 1.0 Å (Table 6.3), consistent with the crystal structure and similar to REDOR. Hence, shifted-REDOR appears also robust and reliable for obtaining structural information. The asymmetry parameter η of 0.1 gave the best fit, which is in line with the lack of anisotropic motion in the methyl group rotation. While there was no anomaly in the implementation of shifted-REDOR for Cu(II)-(DL-Ala)$_2$.H_2O, in shifted-REDOR (Figure 6.3c), the oscillatory behavior observed in the REDOR (Figure 6.3a) is diminished which can be due to the presence of additional protons (NH_2 and Hα). This is consistent with the observations of Schanda *et al.* (2011), who showed that the presence of additional protons near the observed nuclei reduces the oscillatory nature of the shifted-REDOR for ubiquitin crystals.(5, 6)

***Table 6.3**. Dipolar coupling strength of methyl C-H (*$CH_3 1$*) using shifted-REDOR and at different fraction of $\tau_R/2$ by which the π pulse is shifted at MAS frequency of 35 kHz.*

Fraction of $\tau_R/2$ shift	δ kHz	Scaling factor	Methyl C-H distance (Å)
0.685	8.7 ± 2.4	0.30 ± 0.08	1.0 ± 0.3
0.580	8.5 ± 2.6	0.29 ± 0.09	1.1 ± 0.3
0.440	9.2 ± 2.1	0.32 ± 0.07	1.0 ± 0.2

In summary, both REDOR and shifted-REDOR sequences provide reliable estimates of the dipolar coupling strength and consequently information about the structure and methyl rotation.

6.3 Conclusions

This study shows that high resolution ^{1}H based solid-state NMR spectra can be obtained for a paramagnetic system at fast MAS (> 25 kHz). Using the high sensitivity of ^{1}H and the high resolution due to the paramagnetic nature of Cu(II), a temperature dependence study of the model compound Cu(II)-(DL-Ala)$_2$.H_2O could be performed that shows that the shift correlates with the spin delocalization over the ligands. The fast MAS has enabled the implementation of ^{1}H–^{1}H homonuclear spin diffusion, REDOR and shifted-REDOR pulse sequences. Our benchmark is the existing crystal structure. The error in the measured values were similar to that observed for diamagnetic systems and are largely systematic errors from e.g. thermal motions that effectively reduce the dipolar coupling from its rigid limit value. We present a technical step forward by showing that both REDOR and shifted-REDOR are quantitatively reliable in determining the dipolar coupling strength and internuclear distances near the paramagnetic metal center, which paves the way for future application in metalloproteins to probe fast dynamics. In addition, the results contribute to the converging and convincing evidence that paramagnetic solid-state NMR is increasingly accessible and can be interpreted in the same way as the NMR spectra of diamagnetic solids.

6.4 Supporting Information

Sample preparation and solid-state NMR experiments

Cu(II)-(DL-Ala)$_2$.H$_2$O complex was synthesized as reported earlier.(10) All chemicals including the uniformly labelled ^{13}C-DL-alanine were obtained from Sigma Aldrich (USA).

Solid-state NMR experiments were performed with AV-I (17.6 T) 750 MHz and AV-HDIII (22.31 T) 950 MHz spectrometers equipped with a 2.5 mm and 1.3 mm MAS probe, respectively, at spinning frequencies ranging from 30 to 62.5 kHz. 1D proton and carbon spectra were recorded with a rotor synchronized Hahn-echo sequence (Figure S6.4a). The high-power $\pi/2$ pulses were 2 μs and 2.5 μs for ^{1}H and ^{13}C, respectively. A dead time of 4.5 μs was subtracted from the refocusing period in the Hahn-echo pulse sequence. A comparison of spectra obtained with single 90^o pulse (Figure S6.1) with rotor synchronized Hahn-echo spectra (Figure 6.2) confirms that there is little phase distortion in echo spectra obtained with a large spectral window (SW).(4) The advantage of using rotor-synchronized Hahn-echo over single 90^o pulse is elimination of probe artifacts as observed from Figure S6.1a and Figure 6.2a. This prompted us to use rotor-synchronized Hahn-echo pulse sequence to obtain 1D spectra for both carbon and proton for further study.

The 1D and 2D dipolar-INEPT sequence was adopted from Wickramasinghe *et al*., (2008) with a $\pi/2$ pulse length similar to the rotor synchronized Hahn-echo experiment.(13) Temperature dependent experiments were performed at temperatures between 247 K and 318 K. For the 2D ^{1}H–^{1}H spin diffusion (Figure S6.4b) experiment the mixing time was varied from 1 ms to 5 ms with a total acquisition time of 530 μs and a delay of 30 ms between scans. 200 slices of data were acquired in the t1 dimension in a total experiment time of < 5 mins. REDOR and shifted-REDOR data were collected by direct excitation of ^{13}C (Figure S6.4c and S6.4d).(5, 6)·(27–29) The $\pi/2$ pulse lengths were 2 μs and 2.2 μs for ^{1}H and ^{13}C respectively. Temperature calibration was done using samarium tin oxide and lead nitrate.(30–32) Data analysis was performed with TOPSPIN 4.0.5 (Bruker) and Igor pro 6.37.

REDOR and shifted-REDOR data analysis

The REDOR and shifted-REDOR curves were fitted with SIMPSON 4.2.1.(33, 34) The geometry of Cu(II)-(DL-Ala)$_2$.H$_2$O was adopted from Calvo *et al*., and Zhang *et al*., to generate the spin system parameters, dipolar coupling and Euler angles using SIMMOL-VMD.(8, 23, 35, 36) The signal from the methyl C-H was used as a reporter to determine the dipolar coupling strength due to its intrinsic isotropic motion and

high S/N ratio (Figure 6.2a and b). The fitting algorithm as implemented in SIMPSON package was used to estimate the dipolar coupling.(33–35)

The rigid limit dipolar coupling strength of the methyl C-H is ~ 32.1 kHz which corresponds to an internuclear distance of 0.98 Å.(23) It is known that methyl rotation partially averages the dipolar coupling between the C-H bond of the methyl group and therefore the rigid limit dipolar coupling is scaled according to(26, 37)

$$D_{avg} = S * D, \tag{S6.1}$$

with D being the dipolar coupling strength in the rigid limit. The scaling factor is

$$S = (3cos^2\theta - 1)/2, \tag{S6.2}$$

where θ is the angle between the methyl C-H and the rotational axis, which in this case is the bond between $C_\alpha - C_\beta$. For a tetrahedral geometry of the methyl group θ = 109.5°. This gives a theoretical scaling factor of S = 0.333 (Figure S6.5) and D_{avg}=10.69 kHz for the C-H bond in Cu(II)-(DL-Ala)$_2$.H$_2$O in the rotating methyl group. For the analysis of the data, the scaled D_{avg} = 10.69 kHz was changed to fit the experimental data. The average dipolar coupling strength was optimized to fit the REDOR curve using the fitting algorithm of SIMPSON. The homonuclear dipolar coupling between the three protons of the methyl group was also scaled by the theoretical value of 0.333 to give a D_{avg} = 9.76 kHz.(23) The codes for fitting and to obtain the spin-system are uploaded in https://github.com/rubindg/REDOR_fitting_simpson.

Theory of temperature dependence of Fermi contact shifted resonances

The chemical shift of the paramagnetic system is temperature dependent and the observed chemical shift is given by (16)

$$\delta_{obs} = \delta_{dia} + \delta_{FCS} + \delta_{PCS}, \tag{S6.3}$$

where δ_{dia} is the diamagnetic chemical shift and δ_{CS}, δ_{PCS} are the contributions from the Fermi contact shift (FCS) and pseudo-contact shift (PCS) respectively.(16, 38) For the nuclei of coordinating ligands FCS >> PCS and eq. 1 can be written as

$$\delta_{obs} \approx \delta_{dia} + \delta_{FCS}. \tag{S6.4}$$

The contribution from the FCS is given by(38)

$$\delta_{FCS} = \frac{A\langle S_z\rangle}{\hbar\gamma_I B_0}, \tag{S6.5}$$

with $A = \frac{2}{3}\hbar\gamma_I\mu_B g_e\mu_0\rho$ the isotropic hyperfine coupling that is proportional to the spin density ρ on a nucleus. The $\langle S_z\rangle$ is the expectation value of the z magnetization, $\hbar$ is

the reduced Planck constant, γ_I is the gyromagnetic ratio of the nucleus in question, and B_0 is the external magnetic field.
Since the $\langle S_z \rangle$ is related to the magnetic susceptibility according to(38, 39)

$$\langle S_z \rangle = \frac{B_0 \chi}{\mu_B g_e \mu_0}, \quad \text{(S6,6)}$$

where μ_B is the Bohr magneton, $g_e \approx 2.003$ is the free electron g-value, and μ_0 is the permeability of the vacuum, the FCS can also be expressed in terms of the magnetic susceptibility χ by

$$\delta_{FCS} = \frac{A\chi}{\hbar \gamma_I \mu_B g_e \mu_0}. \quad \text{(S6.7)}$$

The system is a linear chain in the high temperature limit, since $2J = -2.2$ cm^{-1}, which translates into ~ 3 K. Therefore, we are in the high temperature limit, $|2J| \ll T$, and the experiments for Cu(II)-(DL-Ala)$_2$.H$_2$O were performed at this limit. The magnetic susceptibility is given by(40)

$$\chi = \frac{S(S+1)\mu_B^2 g_e^2 \mu_0}{3k_B T}, \quad \text{(S6.8)}$$

where $S = 1/2$ is the spin of the Cu(II) ion, k_B is the Boltzmann constant and T is the temperature in Kelvin. Substituting eq. 6 in eq. 5, and in eq. 2 we obtain

$$\delta_{obs} \approx \delta_{dia} + A\frac{S(S+1)\mu_B g_e}{3\hbar \gamma_I k_B T} \quad \text{(S6.9)}$$

for the temperature dependent chemical shift, which was used to determine hyperfine couplings and spin densities by fitting to the data in Figure 6.3.

Supporting figures and tables

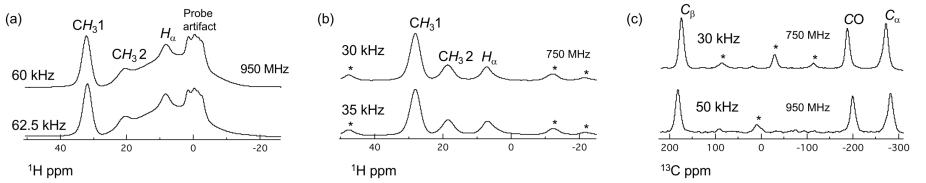


Figure S6.1. *Single 90° pulse experiment for ^{1}H at (a) 950 MHz with MAS of 60 kHz and 62.5 kHz, (b) 750 MHz at MAS of 30 kHz and 35 kHz and for ^{13}C at (c) 750 MHz with MAS of 30 kHz and 950 MHz with MAS of 50 kHz. Resonances marked with * are the spinning side bands. ^{1}H and ^{13}C assignments are indicated with italics.*

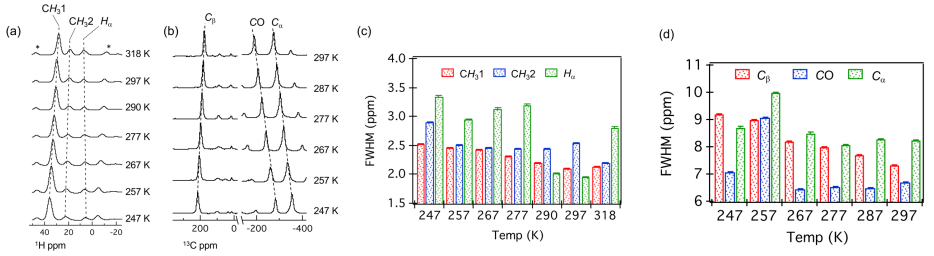


Figure S6.2. *Temperature dependence of (a) Proton and (b) Carbon signals at 30 kHz MAS in a magnetic field of 14 T. The full width at half of the maximum FWHM of (c) Protons (red = C**H**$_3$1, blue = C**H**$_3$2 and green = H$_\alpha$) and (d) Carbons (red = C$_\beta$, blue = CO and green = C$_\alpha$) at different temperature. The peaks marked with stars are the spinning side bands while the smaller peaks in carbon spectra are from small impurities and spinning side bands. Assignments of ^{1}H and ^{13}C signals are indicated in italics.*

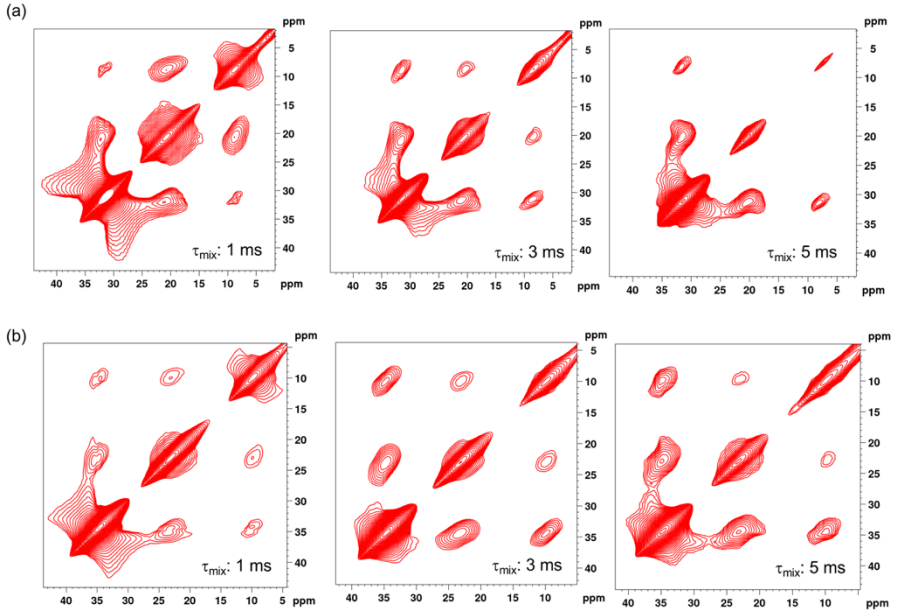


Figure S6.3. *^{1}H–^{1}H spin diffusion spectra at (a) 300 K and (b) 228 K at 60 kHz MAS and 950 MHz ^{1}H frequency with mixing times of 1 ms, 3 ms and 5 ms.*

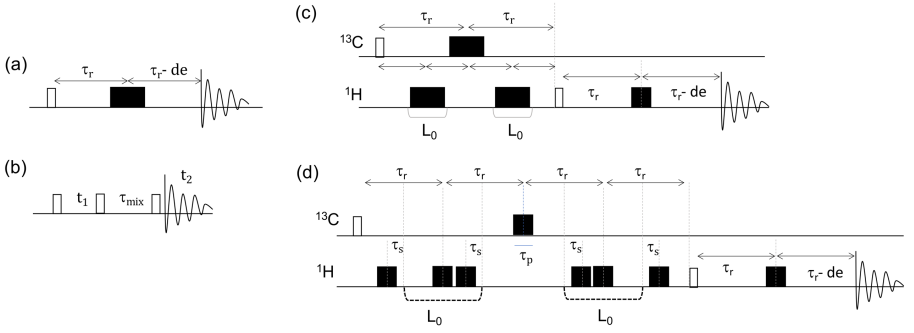


Figure S6.4. *Pulse sequences used in this study. (a) Rotor synchronized Hahn-echo, (b) ^{1}H–^{1}H spin diffusion, (c) Proton detected standard REDOR and (d) Proton detected shifted-REDOR. τ_r denotes the rotor period, t_1 and t_2 are the two-time domains for 2D spectra, τ_s is (0.68 to 0.44)* $\tau_R/2$, τ_p is the π pulse length, de is the dead time of the instrument, τ_{mix} is the mixing time and L_0 is the loop counter for repeating the π pulses.*

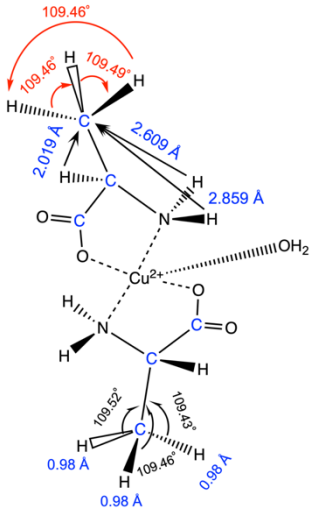


Figure S6.5. *Geometry of Cu(II)-(DL-Ala)2.H₂O adopted from Zhang et al.,(23)*

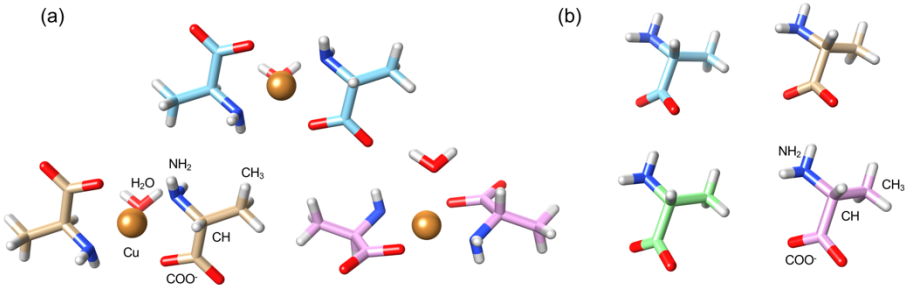


Figure S6.6. *Crystal packing in a unit cell of (a) Cu(II)-(DL-Ala)₂.H₂O (cif:1153761)(8) and (b) DL-alanine (cif:164668)(41).*

***Table S6.1**. Assignment of ^{1}H spectra from the literature on Cu(II)-(DL-Ala)$_2$.H$_2$O.(10, 19) The magnetic field used was from 7.5 T to 11.75 T with spinning frequencies between 15 and 30 kHz.*

Protons of group	δ_{iso} (ppm)
CH_3	32 & 20.4
CH	8.4
NH_2	-132.7 & -159.5
H_2O	1

***Table S6.2**. Properties of Cu(II)-(DL-Ala)$_2$.H$_2$O experimentally determined.*

Properties		Reference
Intrachain AFM exchange coupling constant $2J_0$ at T > 1.8 K	-2.27 ± 0.08 cm^{-1}	(11)
g-factor	2.091 ± 0.005	(11)
Curie temperature from NMR	6.5 K	(20)
Curie Temperature from χ_M (T) vs log T	2.1 K	(8)
^{13}C $T_1\rho$ @ 344 K	ms	(17)
*C*O	8.7 ± 0.1	
*C*H	13.9 ± 0.3	
*C*H$_3$	50.4 ± 1.9	
Δ_{aniso} @ 297 K	ppm	(17)
*C*O	-331 ± 4	
*C*H	-149 ± 10	
*C*H$_3$	53 ± 2	

* The ^{13}C assignments are indicated in italics.

6.5 References

1. Pintacuda, G., N. Giraud, R. Pierattelli, A. Böckmann, I. Bertini, and L. Emsley. 2007. Solid-State NMR Spectroscopy of a Paramagnetic Protein: Assignment and Study of Human Dimeric Oxidized CuII–ZnII Superoxide Dismutase (SOD). *Angewandte Chemie International Edition*. 46:1079–1082.
2. Bertini, I., L. Emsley, M. Lelli, C. Luchinat, J. Mao, and G. Pintacuda. 2010. Ultrafast MAS Solid-State NMR Permits Extensive 13C and 1H Detection in Paramagnetic Metalloproteins. *J. Am. Chem. Soc.* 132:5558–5559.
3. Gwendal Kervern, †, † Guido Pintacuda, ‡ Yong Zhang, ‡ Eric Oldfield, § Charbel Roukoss, § Emile Kuntz, ‖ Eberhardt Herdtweck, § Jean-Marie Basset, † Sylvian Cadars, † Anne Lesage, § and Christophe Copéret, and † Lyndon Emsley*. 2006. Solid-State NMR of a Paramagnetic DIAD-FeII Catalyst: Sensitivity, Resolution Enhancement, and Structure-Based Assignments.
4. Pell, A.J., and G. Pintacuda. 2015. Broadband solid-state MAS NMR of paramagnetic systems. *Progress in Nuclear Magnetic Resonance Spectroscopy*. 84–85:33–72.
5. Schanda, P., B.H. Meier, and M. Ernst. 2011. Accurate measurement of one-bond H–X heteronuclear dipolar couplings in MAS solid-state NMR. *Journal of Magnetic Resonance*. 210:246–259.
6. Schanda, P., M. Huber, J. Boisbouvier, B.H. Meier, and M. Ernst. 2011. Solid-State NMR Measurements of Asymmetric Dipolar Couplings Provide Insight into Protein Side-Chain Motion. *Angew. Chem. Int. Ed.* 50:11005–11009.
7. Jain, M.G., K.R. Mote, J. Hellwagner, G. Rajalakshmi, M. Ernst, P.K. Madhu, and V. Agarwal. 2019. Measuring strong one-bond dipolar couplings using REDOR in magic-angle spinning solid-state NMR. *J. Chem. Phys.* 150:134201.
8. Calvo, R., P.R. Levstein, E.E. Castellano, S.M. Fabiane, O.E. Piro, and S.B. Oseroff. 1991. Crystal structure and magnetic interactions in bis (D, L-alaninato) copper (II) hydrate. *Inorganic chemistry*. 30:216–220.
9. Mirceva, A., J.O. Thomas, and T. Gustafsson. 1989. Structure of trans-bis(dl-α-alaninato)copper(II) monohydrate. *Acta Cryst C, Acta Cryst Sect C, Acta Crystallogr C, Acta Crystallogr Sect C, Acta Crystallogr C Cryst Struct Commun, Acta Crystallogr Sect C Cryst Struct Commun*. 45:1141–1144.
10. Liu, K., D. Ryan, K. Nakanishi, and A. McDermott. 1995. Solid state NMR studies of paramagnetic coordination complexes: A comparison of protons and deuterons in detection and decoupling. *J. Am. Chem. Soc.* 117:6897–6906.
11. Calvo, R., R.P. Sartoris, H.L. Calvo, E.F. Chagas, and R.E. Rapp. 2016. Antiferromagnetic spin chain behavior and a transition to 3D magnetic order in Cu(D,L-alanine)2: Roles of H-bonds. *Solid State Sciences*. 55:144–151.
12. Ishii, Y., N.P. Wickramasinghe, and S. Chimon. 2003. A New Approach in 1D and 2D ^{13}C High-Resolution Solid-State NMR Spectroscopy of Paramagnetic Organometallic Complexes by Very Fast Magic-Angle Spinning. *J. Am. Chem. Soc.* 125:3438–3439.
13. Wickramasinghe, N.P., and Y. Ishii. 2006. Sensitivity enhancement, assignment, and distance measurement in 13C solid-state NMR spectroscopy for paramagnetic systems under fast magic angle spinning. *Journal of Magnetic Resonance*. 181:233–243.
14. Ishii, Y., and N.P. Wickramasinghe. 2008. 1H and 13C High-Resolution Solid-State NMR of Paramagnetic Compounds Under Very Fast Magic Angle Spinning. In: Modern Magnetic Resonance. Springer, Dordrecht. pp. 467–474.
15. Kolbert, A.C., R. Verel, H.J.M. de Groot, and M. Almeida. 1997. Determination of the spin density distribution in the organic conductor DMTM(TCNQ)2 with 13C magic angle spinning NMR. *Molecular Physics*. 91:725–730.
16. Bertini, I., C. Luchinat, G. Parigi, and E. Ravera. 2017. NMR of paramagnetic molecules: applications to metallobiomolecules and models. Second edition. Amsterdam: Elsevier.
17. Wickramasinghe, N.P., M.A. Shaibat, C.R. Jones, L.B. Casabianca, A.C. de Dios, J.S. Harwood, and Y. Ishii. 2008. Progress in C13 and H1 solid-state nuclear magnetic resonance for paramagnetic systems under very fast magic angle spinning. *The Journal of Chemical Physics*. 128:052210.

18. Wickramasinghe, N.P., M. Shaibat, and Y. Ishii. 2005. Enhanced Sensitivity and Resolution in 1H Solid-State NMR Spectroscopy of Paramagnetic Complexes under Very Fast Magic Angle Spinning. *J. Am. Chem. Soc.* 127:5796–5797.
19. Willans, M.J., D.N. Sears, and R.E. Wasylishen. 2008. The effectiveness of 1H decoupling in the 13C MAS NMR of paramagnetic solids: An experimental case study incorporating copper(II) amino acid complexes. *Journal of Magnetic Resonance*. 191:31–46.
20. Sandreczki, T., D. Ondercin, and R.W. Kreilick. 1979. Low-temperature NMR studies of a single crystal of trans-Cu(DL-ala)2.H2O. *J. Am. Chem. Soc.* 101:2880–2884.
21. Kumara Swamy, S.K., A. Karczmarska, M. Makowska-Janusik, A. Kassiba, and J. Dittmer. 2013. Solid-State NMR Correlation Experiments and Distance Measurements in Paramagnetic Metalorganics Exemplified by Cu-Cyclam. *ChemPhysChem*. 14:1864–1870.
22. Szalontai, G., R. Csonka, G. Speier, J. Kaizer, and J. Sabolović. 2015. Solid-State NMR Study of Paramagnetic Bis(alaninato-κ ^{2} *N* , *O*)copper(II) and Bis(1-amino(cyclo)alkane-1-carboxylato-κ ^{2} *N* , *O*)copper(II) Complexes: Reflection of Stereoisomerism and Molecular Mobility in ^{13} C and ^{2} H Fast Magic Angle Spinning Spectra. *Inorganic Chemistry*. 54:4663–4677.
23. Zhang, Y., H. Sun, and E. Oldfield. 2005. Solid-State NMR Fermi Contact and Dipolar Shifts in Organometallic Complexes and Metalloporphyrins. *J. Am. Chem. Soc.* 127:3652–3653.
24. Babinský, M., K. Bouzková, M. Pipíška, L. Novosadová, and R. Marek. 2013. Interpretation of Crystal Effects on NMR Chemical Shift Tensors: Electron and Shielding Deformation Densities. *J. Phys. Chem. A*. 117:497–503.
25. Schanda, P., and M. Ernst. 2016. Studying dynamics by magic-angle spinning solid-state NMR spectroscopy: Principles and applications to biomolecules. *Progress in Nuclear Magnetic Resonance Spectroscopy*. 96:1–46.
26. Wu, C.H., B.B. Das, and S.J. Opella. 2010. 1H–13C hetero-nuclear dipole–dipole couplings of methyl groups in stationary and magic angle spinning solid-state NMR experiments of peptides and proteins. *Journal of Magnetic Resonance*. 202:127–134.
27. Jaroniec, C.P., B.A. Tounge, C.M. Rienstra, J. Herzfeld, and R.G. Griffin. 2000. Recoupling of Heteronuclear Dipolar Interactions with Rotational-Echo Double-Resonance at High Magic-Angle Spinning Frequencies. *Journal of Magnetic Resonance*. 146:132–139.
28. Schaefer, J. 2011. "Development of REDOR rotational-echo double-resonance NMR" by Terry Gullion and Jacob Schaefer [J. Magn. Reson. 81 (1989) 196–200]. *Journal of Magnetic Resonance*. 213:421–422.
29. Gertman, R., I. Ben Shir, S. Kababya, and A. Schmidt. 2008. In Situ Observation of the Internal Structure and Composition of Biomineralized Emiliania huxleyi Calcite by Solid-State NMR Spectroscopy. *J. Am. Chem. Soc.* 130:13425–13432.
30. Aliev, A.E., and K.D.M. Harris. 1994. Simple technique for temperature calibration of a MAS probe for solid-state NMR spectroscopy. *Magn. Reson. Chem.* 32:366–369.
31. Guan, X., and R.E. Stark. 2010. A general protocol for temperature calibration of MAS NMR probes at arbitrary spinning speeds. *Solid State Nuclear Magnetic Resonance*. 38:74–76.
32. Langer, B., I. Schnell, H.W. Spiess, and A.-R. Grimmer. 1999. Temperature Calibration under Ultrafast MAS Conditions. *Journal of Magnetic Resonance*. 138:182–186.
33. Bak, M., J.T. Rasmussen, and N.C. Nielsen. 2000. SIMPSON: A General Simulation Program for Solid-State NMR Spectroscopy. *Journal of Magnetic Resonance*. 147:296–330.
34. Tošner, Z., R. Andersen, B. Stevensson, M. Edén, N.Chr. Nielsen, and T. Vosegaard. 2014. Computer-intensive simulation of solid-state NMR experiments using SIMPSON. *Journal of Magnetic Resonance*. 246:79–93.
35. Vosegaard, T., A. Malmendal, and N.C. Nielsen. 2002. The Flexibility of SIMPSON and SIMMOL for Numerical Simulations in Solid-and Liquid-State NMR Spectroscopy. *Monatshefte für Chemie*. 133:1555–1574.
36. Bak, M., R. Schultz, T. Vosegaard, and N.Chr. Nielsen. 2002. Specification and Visualization of Anisotropic Interaction Tensors in Polypeptides and Numerical Simulations in Biological Solid-State NMR. *Journal of Magnetic Resonance*. 154:28–45.
37. Asami, S., and B. Reif. 2019. Accessing Methyl Groups in Proteins via 1 H-detected MAS Solid-state NMR Spectroscopy Employing Random Protonation. *Scientific Reports*. 9:1–13.
38. Bertini, I., C. Luchinat, and G. Parigi. 2002. Magnetic susceptibility in paramagnetic NMR. *Progress in Nuclear Magnetic Resonance Spectroscopy*. 40:249–273.

39. La Mar, G.N., G.R. Eaton, R.H. Holm, and F.Ann. Walker. 1973. Proton magnetic resonance investigation of antiferromagnetic oxo-bridged ferric dimers and related high-spin monomeric ferric complexes. *J. Am. Chem. Soc.* 95:63–75.
40. Sinn, E. 1970. Magnetic exchange in polynuclear metal complexes. *Coordination Chemistry Reviews*. 5:313–347.
41. Subha Nandhini, M., R.V. Krishnakumar, and S. Natarajan. 2001. dl-Alanine. *Acta Cryst C*. 57:614–615.

Chapter 7

General Discussion and Prospects

Mimics for laccases

Enzymatic biofuel cells (EBC) promise a future of sustainability without adversely affecting the environment. The stability of the enzymes and challenge of functionalizing them on an electrode has, however, limited their application to small devices.(1–3) One way to overcome this disadvantage is to design and synthesize an artificial catalyst based on the active site of enzymes. In the past decade a slew of artificial catalysts has been reported for the enzyme laccase, which catalyzes oxygen reduction at the cathode half of the EBC. Although these catalysts circumvent the issues of instability and immobilization of the laccase, the efficiency of the oxygen reduction reaction was substantially lower than for laccase.(4) There are two prevailing ideas to improve the efficiency of artificial catalysts, (a) incorporating functional groups mimicking the second shell residues and their associated interactions within the active site of laccase and (b) mimicking the motions of the active site residues associated with the complex oxygen reduction reaction. In relation to the latter idea, this thesis aims to lay the groundwork for understanding active site motions in the enzyme small laccase (SLAC).

Motions in enzyme active sites

Enzymes increases the catalytic rate of reaction by stabilizing the transition state. This is achieved by attaining a conformation that has most favorable interactions with the substrate when in its transition state, requiring sub-Ångström precision of positioning of active site atoms. For a multistep process such as oxygen reduction, each step in the reaction is associated with a transition state. The enzyme must therefore change conformation in order to stabilize these successive transition states. Such conformational change during the catalytic cycle is found in many enzymes, for example, alcohol dehydrogenase, dihydrofolate reductase and cytochrome P450.(5–7) In laccase, once the enzyme is reduced from its resting oxidized (RO) state oxygen reduction occurs via the three intermediate states described in Chapter 1, the fully reduced (FR) state, the peroxide intermediate (PI) state and the native intermediate (NI) state. Conformational changes are imperative during this reaction as the interactions at the active site are likely to be different for the transition states of the conversion of dioxygen to peroxide and of peroxide to two separate oxygen atoms. Also, the transfer of protons through the enzyme and binding of oxygen and egress of water molecules may well involve conformational changes of backbone or sidechains. Large conformational changes may themselves have significant activation barriers, to the extent that required conformational changes may become the rate limiting step of the catalytic cycles.

The main goal of the work described in this thesis was to characterize such motions using NMR spectroscopy and to assign them to specific histidine ligands. Characterizing the motions that enable these conformational changes and

implementing them in the bio-inspired catalyst may improve its efficiency. The small size of the inorganic compounds such as discussed in Chapter 1 do not allow for such complicated motions, but a small protein or peptide mimic of the TNC might approach the native system better.

Paramagnetic NMR methodology to study motions

Although the reaction mechanism of laccase has been characterized in detail using multiple crystal structures and quantum calculations, the information about the motions present at the active site was limited. Two crystal structures showed that the histidine ligands of the active site can have two conformations (Chapters 1 and 2). NMR spectroscopy is suitable to identify such motions and determine the exchange rates. In this thesis a ~ 105 kDa trimeric, two-domain laccase, SLAC, was studied. Due to its large size, line broadening caused by the paramagnetic copper ions and large hyperfine shifts it is not possible to use standard multidimensional NMR experiments to study the active site. Therefore, paramagnetically tailored experiment were used in which the delay between the scans and the magnetization transfer between nuclei is reduced to get optimal signal, given the short spin-spin and spin-lattice relaxation times of the nuclei close to the paramagnetic metal center (Chapter 1). Due to the large hyperfine shifts, the signals from the nuclear spins near the metal center in a paramagnetic protein are dispersed over a large spectral region compared to those for diamagnetic proteins. To excite such a large spectral region, short high-power radiofrequency (RF) pulses are required. In addition, standard homonuclear and heteronuclear decoupling methods are found to be inefficient for such a large spectral region and in the worst case it have a deleterious effect on the spectrum.(8) Excitation of multiple smaller spectral regions with changing offset and high power RF pulses can help to resolve this issue.(9) Recent advances in magic angle spinning (MAS) solid state NMR (ssNMR) have also helped in challenging these problems. The sensitivity and resolution of paramagnetic spectrum were improved by using heteronuclear correlation experiments based on transferred-echo double resonance (TEDOR) and dipolar analog of insensitive nuclei enhancement by polarization transfer (D-INEPT) experiment.(10, 11) In these experiments, the polarization transfer time is based on the dipolar coupling strength between the nuclei, which is in μs to ms time scale, thereby efficiently enhancing paramagnetically broadened signals. In addition, very fast MAS (> 20 kHz) has removed the need for decoupling as under such conditions the contribution of the dipolar coupling on the linewidth is sufficiently narrowed.(12) Development of short high-power adiabatic pulses (SHAP) allowed to efficiently excite large spectral windows, ranging from 400 ppm to ~ 1000 ppm.(13)

The RO and NI states

The TNC comprises of a T3 site and a T2 site. Interestingly, the NMR spectra of SLAC were observed to represent a mix of the RO and NI states (Chapters 2, 3 and 4).(14) The SLAC wild type (SLAC-wt) was observed to be predominantly in the RO state, while the T1 site depleted mutant (SLAC-T1D) was mostly in the NI state. Perhaps the reason is that in SLAC-wt the T1 site copper confers some structural restraints on the geometry of the T3 site via the HCH motif so as to render the RO state more stable than the NI state.(14) In the SLAC-T1D this restraint is absent and the NI state becomes predominant. Interestingly, the double mutant SLAC-T1D/Q291E is exclusively in the RO state.(14) This double mutant is discussed in later. It is also observed that the resonances from the RO state are shifted less (11 to 22 ppm) compared to those of the NI state (22 to 55 ppm). The reason is that in the RO state the paramagnetic and diamagnetic states are in fast exchange and the population of the former depends on the energy gap ($2J$, equation 1.5). For a $2J$ of -600 cm^{-1}, the population is about 20% at ambient temperature, so the FCS is significantly smaller than of the NI state, which is a frustrated spin system that is paramagnetic in the ground state.

The strong coupling between all the three copper ions in the NI state (15) increases the electronic relaxation rate enabling the observation of all histidine ligands (Chapters 3 and 4). Similarly, in the RO state, strong coupling between the T3 copper ions enables the observation of resonance from its histidine ligands, while the resonances of the T2 site histidine ligands are broadened beyond detection.(16) It is noteworthy that the Nε2, Cδ2-Hδ2 and Cε1-Hε1 nuclei of the histidine ring are not observed. These atoms are < 3.5 Å and one, two or three bonds from the copper ion and thereby have large electron spin density. This excess electron spin density can lead to the signal broadening beyond detection and very large hyperfine shifts. For a type-1 copper proteins like amicyanin and plastocyanin the resonances of the Hδ2 and Hε1 nuclei from the histidine ligand could be determined.(9, 17) It might be because most of the spin density is localized on the sulfur of the cysteine ligand. This consequently reduces the spin density on the histidine rings thereby enabling the observation of the nuclei very close to the metal center. Saturation transfer experiment can be used to detect signals that are broadened beyond detection in the ^1H NMR spectrum.(9) A "blind" high-power irradiation of the ^1H spectral region ~ 1000 ppm downfield allowed the detection of the resonances from the Hβ2/3 of the cysteine ligand with linewidths of 519 and 329 kHz in plastocyanin.(9) Such experiments are not possible in laccase due to the absence of self-exchange between the diamagnetic and the paramagnetic forms.

The resonances of Nδ1 and Hδ1 nuclei from all the eight (T3+T2 sites) and six (T3 site only) histidine ligands are observed in SLAC-T1D and SLAC-wt respectively (Chapters 3 and 4). In the NI state five chemical exchange processes are identified and

are attributed to the histidine ligands ring motion at the TNC (Chapters 2 and 3). The exchange rates of these process suggest that they are independent processes. However, the energy barrier is similar within the one standard deviation (Chapter 2). The different rates suggest multiple reorganization events in the TNC and some of them might be a conformation that helps in progressing the oxygen reduction reaction to next step. These chemical exchange processes are not observed in the RO state. This may be due to the RO state being more rigid compared to the NI state thus slowing down the histidine ring motions to bring it outside the observed exchange rates of 80 to 200 s^{-1}.

For further characterization of the chemical exchange processes, sequence specific assignment is needed. Using the second shell mutation of Y108F in SLAC-T1D, two of these processes were assigned to the T2 site histidine ligands (Chapter 3). A second shell mutation of Q291E in the SLAC-T1D resulted in the NMR spectra exclusively for the RO state. This is in contrast to the SLAC-T1D/Y108F mutant that was a mix of the NI and the RO state, with the former being the dominant species, analogous to the SLAC-T1D. The switch to the RO state allowed resonance assignment of two T3 site histidine ligands from the RO state. In addition, it revealed the subtle balance between the NI and the RO state. Perhaps this can be explained as follows. Gln291 is located near the T3 site, lining the water channel. This water channel was hypothesized to be the source of protons during the oxygen reduction. The NI state can be converted to the RO state by addition of two protons (Figure 1.3), which are obtained from the environment. Gln291 might well be one of the residues responsible for providing the protons, provided it simultaneously receives one from the surroundings. From the crystal structure 3cg8 of SLAC from *S. coelicolor*, the side chain of Gln291 is strongly hydrogen bonded to Thr167 Oγ1, His164 CO and two water molecules (614 and 732) (Figure 7.1a).(18) Mutating it to Glu291 increases the proton donating ability and thus the NI state can be converted to the RO state for the SLAC-T1D/Q291E mutant with ease. In experiments not reported in the chapters before, we observed a time and pH dependent formation of an unknown state X from SLAC-T1D (Figure 7.1b, c and d). The protein was purified at pH 6.8 and after buffer exchange to pH 8.1 or 7.5 state X is populated in ~ 100 hrs. This state X can be reversed to the initial state, which is a mix of the RO and the NI state with latter being the dominant species, when the pH is lowered again to 6.8. The rate of formation of state X is slower at pH 7.5 than at pH 8.1. In state X the resonances of the NI state (22 to 55 ppm) are reduced in intensity, while those of the RO state (11 to 22 ppm) increase (Figure 7.1b and d). Two additional resonances, pa and pb, are observed in state X (Figure 7.1b and d). Perhaps this state is an intermediate between the NI and the RO states and is accessible at pH > 7.0 because a basic pH can locally increase the proton chemical potential. The pH dependence shown in Figure 7.1b, c and d might well be related to Gln291 donating a single proton and populating a state X that can be a partially

protonated NI state. The existence of such state was reported in Fet3p, an iron oxidizing laccase from *S. cerevisiae* (Figure 7.2).(19) Determining the pH dependence of the spectrum of SLAC-T1D/Q291E might give more insight into the role of the Gln291 residue in the oxygen reduction reaction and explain the reason of its slow rate of conversion. EPR spectroscopy in combination with quantum calculations might help to resolve the nature of state X and establish the role of Gln291.

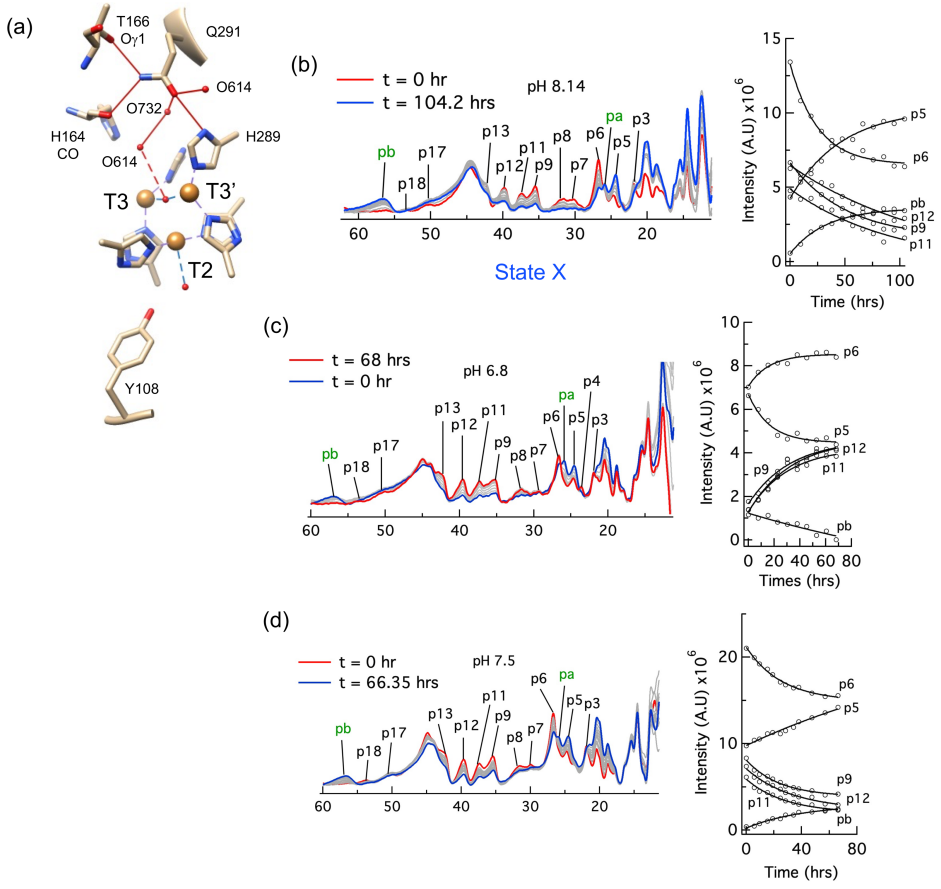


Figure 7.1. *(a) The hydrogen bonding network of the Gln291 side chain. Orange spheres are the copper ions of the TNC. Respective copper ions are indicated. Amino acid residues are shown as wheat sticks. Red spheres are bound water molecules. Residues involved in the hydrogen bond (red sticks) are indicated. A probable hydrogen bond between O614 and the T3 copper ions bridging O is shown as dashed line. The time course ^{1}H NMR spectra of SLAC-T1D at pH 8.14 (b), 6.8 (c) and 7.5 (d). Panel b and c are sequential experiments while panel d is an independent sample. The time course is color coded as red (initial in panel b and d and final in panel c) and blue (final in panel b and d and initial in panel c). The blue trace is of state X as indicated below panel b. Intermediate time spectra are shown as grey*

trace. Each panel is associated with the intensity change of the resonances with time. The solid line shows the single exponential fit of the data points in open circles.

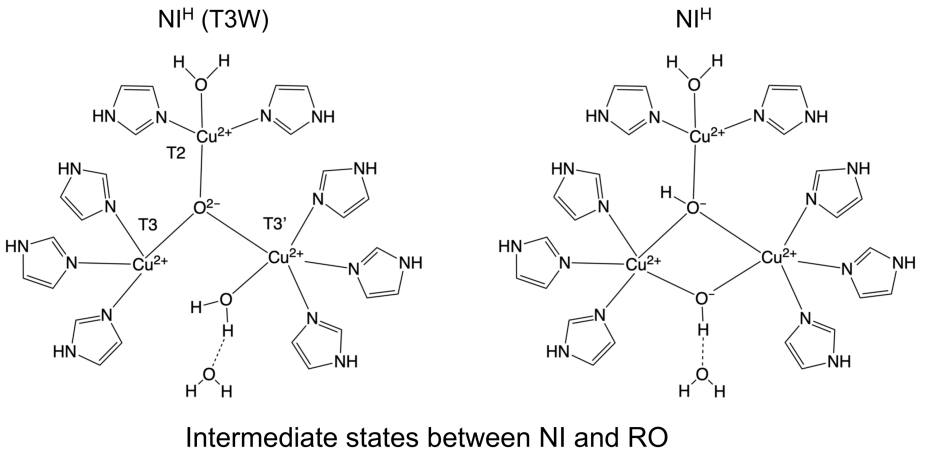


***Figure 7.2**. Proposed intermediate states during the conversion of the NI state to the RO state as described by Heppner et al. (2014).(19)*

Suggestions to obtain further assignments.

Overall, 2/8 histidine ligands in the NI state, one chemical exchange process and 2/6 histidine ligands from the RO state could be assigned sequence specifically. Maybe more second shell mutation can help in assigning resonances to other histidine ligands. Multiple amino acids can be subjected to mutagenesis as shown in Figure 1.2d, for example D113N, I169V, H164A and S294A. All these residues have interactions with the coordinating histidine ligands. Another method that can aid in assignment is using quantum calculations.(20) Such calculations have been extensively done for three-domain laccase, which lacks the Tyr near the T2 site.(15, 21) For SLAC it was reported that this residue plays an important role during catalysis and confers protection against the reactive oxygen species.(22, 23) The calculations on the basic model of the TNC in the RO state with the Tyr revealed that the orientation of the phenolic group determines the formation of the tyrosyl radical (Chapter 5). Radical formation is observed when the phenolic group is oriented toward the water/OH^- ligand of the T2 site. Perhaps the tyrosyl radical in the calculation is an excited state of the RO state that is accessible only when the TNC is partially reduced, as observed experimentally.(22, 23) Using previous calculations as a benchmark (24), optimized geometry of the RO state could be obtained (Chapter 5). A similar strategy can be used to obtain geometry of the other intermediate states. These optimized geometries can be used to estimate the chemical shift on the histidine ligands, thereby aiding in the assignment of the observed resonances.

In paramagnetic solution NMR the signals are affected by two relaxation processes, (i) the interaction between the electron and nuclear spins or the Solomon-Bloembergen dipolar and contact mechanism and (ii) the interaction of the nuclear spin with the net magnetic moment in thermal equilibrium due to the rapid electronic relaxation rate or the Curie mechanism.(25) The Curie relaxation depends on the size of the molecule with relaxation increasing with the size of the molecule. Solid-state NMR (ssNMR) is independent of the molecular size and to a first approximation the contribution from the Curie mechanism is diminished or absent.(25) This results in observation of resonances from the nuclei very close (~ 3.0 Å) to the paramagnetic metal center.(20) In addition, dipolar couplings can be measured with high accuracy using ssNMR and this can provide anisotropic motions associated with residues near the metal centers.(11, 26) Unfortunately, in our hands SLAC was not stable under MAS conditions and paramagnetic signals vanished within a few hours. In Chapter 6 the efficacy of REDOR and shifted-REDOR in determining dipolar coupling strength in a strongly paramagnetic environment is shown. Multidimensional ssNMR experiments based on the dipolar coupling were optimized for application to paramagnetic molecules. As a future outlook these experiments can be applied to study the active site of laccase in greater detail, provided SLAC can be stabilized for experiments under MAS conditions.

References

1. Vincent, K.A., J.A. Cracknell, J.R. Clark, M. Ludwig, O. Lenz, B. Friedrich, and F.A. Armstrong. 2006. Electricity from low-level H_2 in still air – an ultimate test for an oxygen tolerant hydrogenase. *Chem. Commun.* 5033.
2. Vincent, K.A., J.A. Cracknell, A. Parkin, and F.A. Armstrong. 2005. Hydrogen cycling by enzymes: electrocatalysis and implications for future energy technology. *Dalton Trans.* 3397.
3. Sony Develops. *Sony Global - Sony Global Headquarters.*
4. Thorseth, M.A., C.E. Tornow, E.C.M. Tse, and A.A. Gewirth. 2013. Cu complexes that catalyze the oxygen reduction reaction. *Coordination Chemistry Reviews.* 257:130–139.
5. Plapp, B.V. 2010. Conformational Changes and Catalysis by Alcohol Dehydrogenase. *Arch Biochem Biophys.* 493:3–12.
6. Poulos, T.L. 2003. Cytochrome P450 flexibility. *Proceedings of the National Academy of Sciences.* 100:13121–13122.
7. Hammes-Schiffer, S. 2002. Impact of Enzyme Motion on Activity. *Biochemistry.* 41:13335–13343.
8. Pell, A.J., G. Pintacuda, and C.P. Grey. 2019. Paramagnetic NMR in solution and the solid state. *Progress in Nuclear Magnetic Resonance Spectroscopy.* 111:1–271.
9. Bertini, I., S. Ciurli, A. Dikiy, R. Gasanov, C. Luchinat, G. Martini, and N. Safarov. 1999. High-Field NMR Studies of Oxidized Blue Copper Proteins: The Case of Spinach Plastocyanin. *Journal of the American Chemical Society.* 121:2037–2046.
10. Kervern, G., G. Pintacuda, Y. Zhang, E. Oldfield, C. Roukoss, E. Kuntz, E. Herdtweck, J.-M. Basset, S. Cadars, A. Lesage, C. Copéret, and L. Emsley. 2006. Solid-State NMR of a Paramagnetic DIAD-FeII Catalyst: Sensitivity, Resolution Enhancement, and Structure-Based Assignments. *J. Am. Chem. Soc.* 128:13545–13552.
11. Parthasarathy, S., Y. Nishiyama, and Y. Ishii. 2013. Sensitivity and Resolution Enhanced Solid-State NMR for Paramagnetic Systems and Biomolecules under Very Fast Magic Angle Spinning. *Acc. Chem. Res.* 46:2127–2135.

12. Ishii, Y., N.P. Wickramasinghe, and S. Chimon. 2003. A New Approach in 1D and 2D ^{13}C High-Resolution Solid-State NMR Spectroscopy of Paramagnetic Organometallic Complexes by Very Fast Magic-Angle Spinning. *J. Am. Chem. Soc.* 125:3438–3439.
13. Kervern, G., G. Pintacuda, and L. Emsley. 2007. Fast adiabatic pulses for solid-state NMR of paramagnetic systems. *Chemical Physics Letters*. 435:157–162.
14. Machczynski, M.C., and J.T. Babicz. 2016. Correlating the structures and activities of the resting oxidized and native intermediate states of a small laccase by paramagnetic NMR. *Journal of Inorganic Biochemistry*. 159:62–69.
15. Solomon, E.I., A.J. Augustine, and J. Yoon. 2008. O_2 Reduction to H_2O by the multicopper oxidases. *Dalton Trans.* 3921–3932.
16. Bertini, I., C. Luchinat, G. Parigi, and E. Ravera. 2017. NMR of paramagnetic molecules: applications to metallobiomolecules and models. Second edition. Amsterdam: Elsevier.
17. Kalverda, A.P., J. Salgado, C. Dennison, and G.W. Canters. 1996. Analysis of the paramagnetic copper(II) site of amicyanin by 1H NMR spectroscopy. *Biochemistry*. 35:3085–3092.
18. Skálová, T., J. Dohnálek, L.H. Østergaard, P.R. Østergaard, P. Kolenko, J. Dušková, A. Štěpánková, and J. Hašek. 2009. The Structure of the Small Laccase from *Streptomyces coelicolor* Reveals a Link between Laccases and Nitrite Reductases. *Journal of Molecular Biology*. 385:1165–1178.
19. Heppner, D.E., C.H. Kjaergaard, and E.I. Solomon. 2014. Mechanism of the Reduction of the Native Intermediate in the Multicopper Oxidases: Insights into Rapid Intramolecular Electron Transfer in Turnover. *J. Am. Chem. Soc.* 136:17788–17801.
20. Bertarello, A., L. Benda, K.J. Sanders, A.J. Pell, M.J. Knight, V. Pelmenschikov, L. Gonnelli, I.C. Felli, M. Kaupp, L. Emsley, R. Pierattelli, and G. Pintacuda. 2020. Picometer Resolution Structure of the Coordination Sphere in the Metal-Binding Site in a Metalloprotein by NMR. *J. Am. Chem. Soc.* 142:16757–16765.
21. Jones, S.M., and E.I. Solomon. 2015. Electron Transfer and Reaction Mechanism of Laccases. *Cell Mol Life Sci*. 72:869–883.
22. Tian, S., S.M. Jones, and E.I. Solomon. 2020. Role of a Tyrosine Radical in Human Ceruloplasmin Catalysis. *ACS Cent. Sci.*
23. Gupta, A., I. Nederlof, S. Sottini, A.W.J.W. Tepper, E.J.J. Groenen, E.A.J. Thomassen, and G.W. Canters. 2012. Involvement of Tyr108 in the Enzyme Mechanism of the Small Laccase from Streptomyces coelicolor. *Journal of the American Chemical Society*. 134:18213–18216.
24. Quintanar, L., J. Yoon, C.P. Aznar, A.E. Palmer, K.K. Andersson, R.D. Britt, and E.I. Solomon. 2005. Spectroscopic and Electronic Structure Studies of the Trinuclear Cu Cluster Active Site of the Multicopper Oxidase Laccase: Nature of Its Coordination Unsaturation. *J. Am. Chem. Soc.* 127:13832–13845.
25. Kervern, G., S. Steuernagel, F. Engelke, G. Pintacuda, and L. Emsley. 2007. Absence of Curie Relaxation in Paramagnetic Solids Yields Long ^{1}H Coherence Lifetimes. *J. Am. Chem. Soc.* 129:14118–14119.
26. Schanda, P., and M. Ernst. 2016. Studying dynamics by magic-angle spinning solid-state NMR spectroscopy: Principles and applications to biomolecules. *Progress in Nuclear Magnetic Resonance Spectroscopy*. 96:1–46.

Summary

Enzymatic biofuel cells (EBCs) promise a sustainable future. They use enzymes to oxidize substrates at the anode and reduce oxygen to water at the cathode. Laccases are preferred enzymes for the oxygen reduction reaction but their stability is reduced when functionalized over an electrode. Artificial, bio-inspired catalysts were designed to overcome this challenge but come at a cost of losing catalytic efficiency. Motions within the active site of laccase might be one of the reasons that determine this efficiency. Specific motions can help attain a conformation that can reduce the energy barrier of a catalytic step by having favourable interactions with the transition state. For the complex oxygen reduction reaction, consisting of multiple steps, such motions seem unavoidable. This thesis provides the groundwork to study such motions at the active site of laccase using NMR spectroscopy.

Chapter 1 summarizes the properties of the tri-nuclear copper center (TNC) of several laccases, where oxygen reduction takes place, and compares the TNC complexity with the reported artificial catalysts. The two-domain trimeric small laccase from *Streptomyces coelicolor* (SLAC) is used in this study. Due to the paramagnetic nature of the copper ions in the TNC, application of standard NMR experiments is not possible to characterize the dynamics or assign the resonances. Paramagnetically tailored NMR experiments and second-shell mutagenesis aided in overcoming this challenge. The native intermediate (NI) state and the resting oxidized (RO) state of the TNC are studied in detail (Chapters 2 to 4). The NMR spectra of SLAC are shown to represent a mixture of these two states (Chapters 3 and 4). The NI state was studied using a type 1 site depleted mutant of small laccase (SLAC-T1D) because the relative intensities show it to be the major state in this mutant. Five chemical exchange processes were discovered and could be attributed to ligand histidine ring motions (Chapters 2 and 3). The second-shell mutation of Y108F aided in assigning two of these processes to two histidine ligands in the NI state (Chapter 3). The RO state was studied using SLAC wild type (wt) because this is the major state (Chapter 4). Interestingly, another second-shell mutation, Q291E of SLAC-T1D, is found to cause the enzyme to be exclusively in the RO state. This result suggests a subtle balance between the RO and the NI states (Chapter 4). Using SLAC-wt and SLAC-T1D/Q291E, resonances were assigned to two histidine ligands in the RO state (Chapter 4). In the NI and RO states, all eight (T3 + T2 sites) and six (T3 site only) histidine ligands, respectively, are observed.

Quantum calculation can be advantageous in assigning the resonances. This requires a proper description of the geometry of the TNC. Using previous studies as a benchmark, the geometry of the RO state was modelled and the electronic structure

was calculated. This work shows that the orientation of Y108 hydroxyl group is important for the spin density distribution at the TNC (Chapter 5).

Solid state NMR can provide information about the dipolar coupling between nuclei near the metal center. The dipolar coupling strength can be used to probe the presence of anisotropic motions at the active site of laccase. Chapter 6 shows the efficacy of rotational echo double resonance (REDOR) based pulse sequence in determining the dipolar coupling in a paramagnetic environment in a model compound Cu-DL-$(Ala)_2.H_2O$. It is shown that accurate distance information can be obtained from REDOR experiments (Chapter 6).

Samenvatting

Enzymatische biobrandstofcellen (EBS's) beloven een duurzame toekomst. Ze gebruiken enzymen om substraten aan de anode te oxideren en om zuurstof aan de kathode te reduceren. Laccases zijn ideale enzymen voor de reductie van zuurstof, maar ze verliezen stabiliteit wanneer ze gebruikt worden voor oppervlakte-functionalisatie van een elektrode. Bio-geïnspireerde katalysatoren zijn ontworpen om deze uitdaging het hoofd te bieden, maar dat gaat ten koste van de katalytische efficiëntie. Bewegingen in het actieve centrum van laccase kunnen van invloed zijn op deze efficiëntie. Specifieke bewegingen kunnen het enzym helpen om een conformatie aan te nemen die de energiebarrière van een katalytische stap verlaagt door gunstige interacties te hebben met de overgangstoestand. Deze bewegingen lijken onvermijdelijk voor de complexe reductiereactie van zuurstof, die uit meerdere stappen bestaat. Dit proefschrift vormt de basis voor het bestuderen van dergelijke bewegingen in het actieve centrum van laccase met behulp van NMR-spectroscopie. Hoofdstuk 1 geeft een samenvatting van de eigenschappen van het tri-nucleaire kopercentrum (TNC), waar zuurstofreductie plaatsvindt, van verschillende laccases, en vergelijkt het TNC met de gerapporteerde kunstmatige katalysatoren.

In deze studie wordt gebruikt gemaakt van de kleine laccase van *Streptomyces coelicolor* (SLAC), een trimeer van een eiwit met twee domeinen. Vanwege de paramagnetische aard van de koperionen in het TNC is niet mogelijk om de dynamiek te karakteriseren en de resonanties toe te kennen met standaard NMR-experimenten. NMR-experimenten aangepast voor paramagnetische monsters en mutaties in de tweede coördinatieschil van het enzym zijn gebruikt om deze uitdagingen te overwinnen. De natieve intermediaire (NI) toestand en de geoxideerde rusttoestand (RO) van het TNC zijn uitvoerig bestudeerd (Hoofdstukken 2 t/m 4). Het NMR-spectrum van SLAC laat een combinatie zien van deze twee toestanden (Hoofdstukken 3 en 4). De NI-toestand is bestudeerd door gebruik te maken van een variant die het koperion in het type 1-centrum mist (SLAC-T1D), omdat de relatieve intensiteiten in het NMR-spectrum laten zien dat die toestand voor deze variant de hoofdtoestand is. Vijf uitwisselingsprocessen werden ontdekt en toegeschreven aan rotatie van de ringen van histidineliganden (Hoofdstukken 2 en 3). De Y108F mutatie in de tweede coördinatieschil hielp bij het toekennen van twee van deze processen aan twee histidineliganden in de NI-toestand (Hoofdstuk 3). De RO-toestand is bestudeerd met het wild-type (wt) SLAC, omdat deze toestand daarin de hoofdtoestand is (Hoofdstuk 4). Een tweede mutatie, Q291E in SLAC-T1D, blijkt ervoor te zorgen dat SLAC slechts in de RO-toestand voorkomt, wat aangeeft dat er een subtiel evenwicht bestaat tussen de RO- en NI-toestanden (Hoofdstuk 4). Door gebruik te maken van SLAC-wt en SLAC-T1D/Q291E werden resonanties toegekend aan twee histidine liganden in de RO-toestand (Hoofdstuk 4). In zowel de NI- als de RO-toestand zijn alle

histidineliganden waargenomen, dit zijn respectievelijk acht (T3 + T2-centra) en zes (alleen T3-centrum) liganden.

Kwantumberekeningen kunnen helpen bij het toekennen van de resonanties in paramagnetische systemen, maar dit vereist een goede beschrijving van de geometrie van het TNC. Door voort te borduren op eerdere studies, kon de geometrie van de RO-toestand worden gemodelleerd en de elektronische structuur berekend. Dit werk laat zien dat de oriëntatie van de hydroxylgroep van Y108 belangrijk is voor de spin-dichtheidsverdeling in het TNC (Hoofdstuk 5).

Vaste-stof-NMR kan informatie geven over de dipolaire koppeling tussen kernen nabij het metaalcentrum. De dipolaire koppelingssterkte kan worden gebruikt om anisotrope bewegingen in het actieve centrum van laccase te onderzoeken. Hoofdstuk 6 toont aan dat een pulssequentie die gebaseerd is op rotatie-echo dubbele resonantie (REDOR) gebruikt kan worden bij het bepalen van de dipolaire koppeling in een paramagnetische omgeving in de modelverbinding Cu-DL-$(Ala)_2.H_2O$. Nauwkeurige afstandsinformatie kan zo worden verkregen uit REDOR-experimenten (Hoofdstuk 6).

Curriculum vitae

Rubin Dasgupta was born in Kolkata, West Bengal, India on 14th February 1992 and raised in Sindhudurg, Maharashtra, India. After completing his schooling, he moved to Dehradun, India (at the foot of the Himalayas) for his Bachelor's degree in 2009. During this time, he got tutored in wide range of disciplines including botany, zoology, chemistry and biotechnology. After taking a gap year to travel across India he moved to his birth place and joined the Master's degree course at Bose Institute in 2013. Here he developed skills and interest for NMR spectroscopy. He did his Master's internship with Prof. Dr. Gautam Basu and discovered a novel helix N-cap motif that might confer stability to the helix and allows it to participate in long range interactions in proteins. This discovery led to his first peer review article and a best poster award at the 7th peptide engineering meeting, Pune, India. Rubin was also involved in refurbishing a time-resolved fluorimeter and establishing a protocol to study peptide/protein and nanoparticle interaction. After obtaining his Master's degree in 2015, he obtained a fellowship from the council of scientific and industrial research (CSIR), India, to work as a junior research fellow and develop NMR methodology in combination with time resolved fluorescence spectroscopy. After a year, in 2016 he joined Leiden University for his PhD with Prof. Dr. Marcellus Ubbink and Prof. Dr. Huub J.M. de Groot. Here, he developed paramagnetic NMR methodology to study the active site of laccase. He was successful in obtaining the first two-dimensional NMR spectrum of small laccase and identify motions at its active site. He also optimized solid state NMR methods to study paramagnetic molecules. He presented his work at the 19th international Conference on Biological Inorganic Chemistry, Interlaken, Switzerland for which he was awarded the Kroese-Duijters travel grant from Leids Universiteits Fonds, Leiden University. He also presented his work at CHAINS 2020, The Netherlands, Biophysical Society Virtual networking meeting: Magnetic resonance meet the future of Biophysics 2020 and NMR Discussion group meeting, 2020, The Netherlands. After completing his thesis, he will join Dr. Katja Petzold's group at Karolinska Institute, Sweden for his post-doctoral research.

List of Publications

Dasgupta, R., H.K. Ganguly, E.K. Modugula, and G. Basu. 2017. Type VIa β-turn-fused helix N-termini: A novel helix N-cap motif containing cis-proline. *Peptide Science*. 108:e22919.

Bera, S., J. Dhar, **R. Dasgupta**, G. Basu, S. Chakraborti, and P. Chakrabarti. 2018. Molecular features of interaction involving hen egg white lysozyme immobilized on graphene oxide and the effect on activity. *International Journal of Biological Macromolecules*. 120:2390–2398.

Dasgupta, R., K.B.S.S. Gupta, F. Nami, H.J.M. de Groot, G.W. Canters, E.J.J. Groenen, and M. Ubbink. 2020. Chemical Exchange at the Trinuclear Copper Center of Small Laccase from *Streptomyces coelicolor*. *Biophysical Journal*. 119:9–14.

Dasgupta, R., K.B.S.S. Gupta, H.J.M. de Groot, and M. Ubbink. 2021. Towards resolving the complex paramagnetic nuclear magnetic resonance (NMR) spectrum of small laccase: assignments of resonances to residue-specific nuclei. *Magnetic Resonance*. 2:15–23.

Dasgupta, R., K.B.S.S. Gupta, H.J.M. de Groot, and M. Ubbink. 2021. The Resting Oxidized State of Small Laccase Analyzed with Paramagnetic NMR Spectroscopy. *ChemPhysChem*. 22:733–740.

Dasgupta, R., K.B.S.S. Gupta, D. Elam, M. Ubbink, and H.J.M. de Groot. 2021. Dipolar dephasing for structure determination in a paramagnetic environment. *Solid State Nuclear Magnetic Resonance*. 113:101728.

Chatterjee, S.D., J. Zhou, **R. Dasgupta**, A. Cramer-Blok, M. Timmer, M. van der Stelt, and M. Ubbink. 2021. Protein Dynamics Influence the Enzymatic Activity of Phospholipase A/Acyltransferases 3 and 4. *Biochemistry*. 60:1178–1190.